University of Alberta

HEAVY PARTICLE DISPERSION OVER LEVEL TERRAIN AND IN WINDBREAK FLOW

by

Thomas Bouvet

A thesis submitted to the Faculty of Graduate Studies and Research in partial fulfillment of the requirements for the degree of Doctor of Philosophy

Department of Earth and Atmospheric Sciences

Edmonton, Alberta

Spring 2006

Library and Archives Canada

Published Heritage Branch

395 Wellington Street
Ottawa ON K1A 0N4
Canada

Bibliothèque et Archives Canada

Direction du Patrimoine de l'édition

395, rue Wellington
Ottawa ON K1A 0N4
Canada

Your file Votre référence
ISBN: 0-494-13940-4
Our file Notre référence
ISBN: 0-494-13940-4

NOTICE:
The author has granted a non-exclusive license allowing Library and Archives Canada to reproduce, publish, archive, preserve, conserve, communicate to the public by telecommunication or on the Internet, loan, distribute and sell theses worldwide, for commercial or non-commercial purposes, in microform, paper, electronic and/or any other formats.

The author retains copyright ownership and moral rights in this thesis. Neither the thesis nor substantial extracts from it may be printed or otherwise reproduced without the author's permission.

AVIS:
L'auteur a accordé une licence non exclusive permettant à la Bibliothèque et Archives Canada de reproduire, publier, archiver, sauvegarder, conserver, transmettre au public par télécommunication ou par l'Internet, prêter, distribuer et vendre des thèses partout dans le monde, à des fins commerciales ou autres, sur support microforme, papier, électronique et/ou autres formats.

L'auteur conserve la propriété du droit d'auteur et des droits moraux qui protège cette thèse. Ni la thèse ni des extraits substantiels de celle-ci ne doivent être imprimés ou autrement reproduits sans son autorisation.

In compliance with the Canadian Privacy Act some supporting forms may have been removed from this thesis.

While these forms may be included in the document page count, their removal does not represent any loss of content from the thesis.

Conformément à la loi canadienne sur la protection de la vie privée, quelques formulaires secondaires ont été enlevés de cette thèse.

Bien que ces formulaires aient inclus dans la pagination, il n'y aura aucun contenu manquant.

Canada

Abstract

This PhD thesis first re-examines and further develops an analytical solution for the deposition swath of heavy particles released in the atmosphere from an elevated source over uniform terrain, correcting the particle diffusivity for the crossing trajectory effect. Despite its neglect of the turbulent flux, the revised (approximate) analytical solution proves to be accurate within 20% provided the variable $\overline{u}(H_s)/w_g \leq 7$ (ratio of the mean horizontal wind speed at source height to the particle gravitational settling velocity). In this domain of validity, simple formulae relating the statistics of the deposition swath to $\overline{u}(H_s)/w_g$ are derived. The rest of this work investigates the impact of a windbreak on heavy particle dispersion and its numerical modelling. Setting up a windbreak is a common practice in agriculture, often aimed at controlling particle transfer as a result of filtration and distortion of the carrying windflow. New observations of heavy particle deposition within a flow disturbed by a porous thin fence, as well as measurements of concentration along vertical profiles on both sides of a thick 'shelterbelt' of corn are presented. These data are used to diagnose the capabilities of a Lagrangian Stochastic (LS) particle trajectory model, coupled to a wind model providing fields of wind statistics, to capture the impact of a windbreak on dispersion. The concentration and the deposition rates, as simulated by the model, match the observation within 30% accuracy. These results suggest that (1) the LS model handles properly the heterogeneities of the flow; (2) the heuristic adjustments made to account for the inertia of heavy particles are useful approximations; (3) the description of particle interactions with leaves provides a reasonably satisfactory account of filtration by a natural hedge. The numerical simulations show that while

the windflow disturbance lowers the deposition peak, it also spreads deposition further away from the source. In the case of a thick windbreak, an important fraction of the particles entering the shelterbelt across its upstream face are lifted out of its volume by the mean updraft induced by the deceleration of the flow, these particles thereby escaping deposition.

Acknowledgements

I would like to thank my supervisor John Wilson for his availability to share his skills as a talented scientist and as a fine writer.

I would like to thank Brigitte Durand for her invaluable support and exceptional commitment in the experiments.

I am grateful also for financial support received from the Department of Earth and Atmospheric Sciences in the form of a Graduate Teaching Assistantship, and from the Natural Sciences and Engineering Research Council of Canada (NSERC) through a grant to John. D. Wilson.

I dedicate this thesis to all the student fellows with whom I built friendships over the course of this PhD. The entertaining times we shared were the mind-refreshment that fed my enthusiasm to pursue my work.

Contents

1 Introduction **1**

1.1 Humans manipulate microclimate. 2

1.2 Aerial transport of heavy particles raises problematical issues . 6

1.3 Windbreaks, a useful strategy to confine particle deposition? . 7

1.4 Options for modelling heavy particle dispersion about/inside a windbreak. 9

1.4.1 Modelling particle dispersion in a given wind flow . . . 9

1.4.2 Modelling the wind flow 14

1.4.3 Modelling particle filtration 18

1.5 Presentation of the thesis, and novelty of this work. 23

1.5.1 An analytical solution for particle deposition on uniform terrain accounting for the 'Crossing Trajectory Effect'. 23

1.5.2 Provision of new experimental data. 25

1.5.3 New evidence on the skills of a coupled RANS-LS model for heavy particle dispersion in a windbreak flow. . . . 33

1.5.4 A new insight into the dispersion patterns of heavy particles in windbreak flow. 34

1.6 References. 35

2 An approximate analytical solution for the deposition of heavy

particles released from an elevated line source **47**

2.1 Introduction 48

2.2 The analytical solution 49

2.2.1 The Rounds-Godson solution 49

2.2.2 Accounting for the Crossing Trajectory Effect (CTE) . 52

2.3 Discussion and test of the analytical solution 56

2.3.1 On the assumption of 'far field' dispersion 56

2.3.2 Neglect of turbulent deposition 58

2.3.3 Test against experimental results and Lagrangian Stochastic (LS) simulations 62

2.4 An even simpler description implicit in the analytical solution 69

2.5 Conclusion 72

2.6 References 73

3 Observations and modelling of heavy particle deposition in a windbreak flow **77**

3.1 Introduction 78

3.2 The experiment 79

3.2.1 Material 81

3.2.2 Micro-meteorological measurements 85

3.2.3 Deposition measurements 85

3.3 The particle transport model 86

3.3.1 Generalized Langevin equation 87

3.3.2 Adjustments to the Langevin equation for heavy particle dispersion 89

3.3.3 Reproducing the experimental conditions 91

3.4 Results 105
3.4.1 Micrometeorological data 105
3.4.2 Deposition 105
3.4.3 Discussion and Conclusions 109
3.5 References 119

4 Filtering of windborne particles by a natural windbreak. 125
4.1 Introduction 126
4.2 Particle entrapment by a shelterbelt: measured particle fluxes 129
4.2.1 Host flow 135
4.2.2 Particle concentrations and fluxes 135
4.3 Theoretical model of particle filtration 139
4.3.1 Resolved scales of motion 139
4.3.2 Modelling of a virtual source 141
4.3.3 Parameterization of deposition and rebound on leaves. 143
4.4 Results 145
4.4.1 Micrometeorology of the host flow 145
4.4.2 The wind flow about the shelter belt 146
4.4.3 Particle concentration and fluxes 150
4.4.4 Comparison with the treatment of entrapment by Raupach et al. (2001) 160
4.4.5 Particle dispersion patterns. 163
4.5 Conclusions 173
4.6 References 174

5 Conclusions 179
5.1 Summary of findings 180

5.1.1 Provision of an approximate solution for the deposition of heavy particles on uniform terrain 180
5.1.2 Provision of new experimental data. 181
5.1.3 Diagnosis of the capabilities of a coupled RANS-LS model. 181
5.1.4 Insight into the patterns of dispersion in a windbreak flow. 183
5.2 Recommendations for future research. 184
5.2.1 Provision of recommendations for windbreak design . . 184
5.2.2 An analytical treatment of particle filtering. 185
5.3 Long distance particle transport and landscape structure: a broader perspective. 185
5.4 References 188

Appendices **191**

A-1 Finite-difference solutions of the advection-diffusion equation. 192
A-2 The Lagrangian Stochastic (LS) model. 194
A-3 Steadiness of the passive point source in runs P 195
A-4 Lateral homogeneity of the line source (runs L) 197
A-5 Possible disturbance of deposition collector walls on particle deposition 199
A-6 Automated particle count 201
A-7 Code sources 203

List of Tables

3.1 Values of the normalized variances (in the limit $z/L_{\mathrm{mo}} \rightarrow 0$) of the wind velocity in the along-wind, the cross-wind and the vertical direction 117

3.2 Experimental conditions during runs 118

4.1 Conditions of the experimental runs. 147

4.2 Micrometeorological conditions: comparison of results from two alternative methods 148

List of Figures

1.1 Screen harvesting water droplets in coastal fog 3

1.2 Schematic of temperature profiles in a stable atmosphere when the air is mixed artifically by a fan and when it is not 5

1.3 Corn leaves: not cylinders, not regular, and living in a turbulent flow 20

1.4 Artificial fence erected in a straight fashion on a flat terrain . 27

1.5 Resistance coefficient of the screen fabric measured in wind-tunnel, as a function of the Reynolds' number based on the fabric mesh size 27

1.6 Spherical glass beads spread over a glass strip coated with glycerin 28

1.7 Line source composed of nine point sources lined up parallel to the windbreak 29

1.8 Petri dish filled with liquid: a collector of beads depositing on ground 29

1.9 Corn shelterbelt frontal view 30

1.10 Corn shelterbelt viewed between two rows of plants 31

1.11 Vertical profile of wind cup anemometers immediatly upwind of the corn shelterbelt 32

2.1 Normalized deposition rate of heavy particles. Experimental data versus the analytical solution of Godson or the revised analytical solution. 53

2.2 Estimation of the number N of independent velocity choices made by a particle along its trajectory, as a function of particle gravitational settling velocity 57

2.3 Fractional contribution of turbulent deposition to total deposition 60

2.4 Deposition swath of heavy particles. Comparison of the analytical solution with the numerical solution of the advection-diffusion equation when turbulent deposition is ignored or when it is included 61

2.5 Fractional error in the approximate analytical solution, relative to a numerical solution of the advection-diffusion equation when turbulent deposition is accounted for 63

2.6 Position of the deposition peak: comparison between the analytical solution and experimental results 65

2.7 Normalized peak deposition rate: comparison between the analytical solution and experimental results 66

2.8 Comparison between the analytical solution and the corresponding LS solution for (a) the location of the deposition peak; (b) the magnitude of the normalized deposition peak; (c) the standard deviation of the deposition location; (d) the '90% recovery distance' 67

2.9 Analytical solution of the location of the deposition peak . . . 70

3.1 Top view schematic of the experimental setup 80

3.2 Picture of the spherical glass beads 81
3.3 Schematic of the point source 82
3.4 Frontal and side views of an element that composes the line source 83
3.5 Windbreak induced disturbance of the horizontal average velocity field and of the turbulent kinetic energy field 93
3.6 Side view of particle trajectories simulated by the coupled RANS-LS model 94
3.7 Top view of computed trajectories of particles released by the line source 95
3.8 Deposition swath of particles. Comparison between experimental data and numerical simulations when $C^*_{ww} = 1.5$, $C^*_{ww} = 2.0$, or $C^*_{ww} = 2.5$ 98
3.9 Measured cross-wind deposition swath of particles for run P1 . 100
3.10 Cross-wind deposition swath of runs P1, P4, and P5. Comparison between the experimental data and the LS simulations with treatment 1 or with treatment 2 of the lateral dispersion . . . 102
3.11 Deposition swath computed by the LS model when $\chi = 0.1$, $\chi = 0.5$ and $\chi = 1.0$ 104
3.12 Deposition swath of particles after dispersion over uniform terrain: numerical results versus experimental data 107
3.13 Deposition swath of particles dispersing about a fence: numerical results versus experimental data 110
3.14 Computed deposition swath of particles dispersing in a fence-disturbed flow, when particles flow freely through the fence without being entrapped or when particles are allowed to deposit onto the fence 112

3.15 Computed deposition swath of particles dispersing in the reference flow or in a flow disturbed by the fence which does not entrap particles 113

3.16 Normalized concentration fields of particles dispersed in various wind flows 115

4.1 Vertical profile of the leaf azimuthal angle distribution of the shelterbelt 130

4.2 Vertical profile of the leaf zenithal angle distribution of the shelterbelt 131

4.3 Vertical profile of the vegetation area density $A(z)$ and its projections 132

4.4 Side view of the experimental setup 133

4.5 Frontal view of the experimental setup 134

4.6 Schematic of a the particle trap instrument 137

4.7 Side view of numerically simulated particle trajectories across the shelterbelt 142

4.8 Disturbance in the mean horizontal velocity and in the turbulent kinetic energy 149

4.9 Mean horizontal velocity perpendicular to the hedge, computed by the RANS model and measured experimentally 151

4.10 Vertical profiles of concentration (normalized by the source intensity Q_g) measured immediately upwind and downwind from the shelterbelt, and corresponding numerical simulations . . . 152

4.11 Actual particle size distribution at $z/H = 0.6$, $x/W = -0.6$ (virtual source plane) versus distribution derived from linear interpolation between the distribution at the top and the bottom of the shelterbelt 157

4.12 Normalized particle fluxes across the upwind face of the hedge, across the downwind face or onto ground 159

4.13 Computed fields of particle concentration and vertical fluxes about the corn belt 164

4.14 Proportion of particles of diameter 10 ± 1 μm, 30 ± 1 μm and 50 ± 1 μm along a horizontal transect at $z/H = 0.6$ across the shelterbelt 166

4.15 Deviation in the median particle size, in micrometers, calculated by numerical simulation 167

4.16 Particle mass budget in the shelterbelt (numerical simulation) 169

4.17 Computed horizontal fluxes of particles carried by the mean velocity field, the turbulent velocity field or by the overall wind field, across the upwind and downwind faces of the shelterbelt 171

4.18 Computed vertical flux across the top boundary of the shelterbelt, carried by the mean flow, the turbulent flow or the gravitational settling 172

A-1 Evolution of the particle source release rate over the duration of an experimental run 196

A-2 Normalized deposition rate along the windbreak 198

A-3 Ratio of particle deposition into high wall collectors (80 mm high) to deposition into low wall collectors (18 mm high) . . . 200

A-4 Comparison between automated count and optical count . . . 202

List of notations

$(\overline{\ })$ ..... Time averaged quantity.

$(')$ ..... Deviation from a time averaged quantity.

β ..... Empirical parameter relating Eulerian and Lagrangian scales.

Γ ..... Gamma function.

ϵ ..... Dissipation rate of the turbulent kinetic energy.

ζ ..... Time of separation.

η ..... Optical porosity.

θ ..... Wind direction.

κ ..... Particle transmittance across a windbreak.

μ ..... Dynamic viscosity of air.

ν ..... Thermal stability parameter.

ξ ..... Correction factor for turbulent diffusivity.

ρ ..... Air density.

ρ_p ..... Particle density.

σ_x ..... Standard deviation in the quantity x.

τ_p ..... Particle Stokesian time scale.

φ_m ..... Monin-Obukhov universal function for momentum.

Ω ..... Speed of rotation.

A ..... Vegetation area density.

c ..... Particle concentration.

C_{uu} ..... Variance of u normalized by u_*^2

C_0 ..... Kolmogorov universal constant

C_d ..... In-situ drag coefficient of vegetation.

d_p ..... Particle diameter.

D ..... Particle deposition flux.

e ..... Coefficient of velocity restitution upon rebound.

E_F ..... Efficiency of filtration.

E_I ..... Efficiency of impaction.

E_{df} ..... Efficiency of deposition on a single fiber.

E_{dv} ..... Efficiency of deposition on vegetation.

Err ..... Fractional error.

g ..... Gravitational acceleration.

H ..... Windbreak height.

H_s ..... Particle source height.

K ..... Particle eddy diffusivity.

k_r ..... Barrier resistance coefficient.

k_v ..... Von Karman constant.

l ..... Particle path length.

L_{mo} ..... Monin-Obukhov length.

L_m ..... Length scale of the screen mesh.

L_v ..... Length scale of a vegetation element.

L_E ..... Eulerian length scale.

L_L ..... Lagrangian length scale.

m ..... meandering factor.

N_p ..... Number of particles.

P_I ..... Probability of particle interception.

Q ..... Particle source intensity.

Q_h ..... Heat flux.

R ..... Velocity auto-correlation function.

Re ..... Reynolds' number.

s ..... Horizontal wind velocity.

S_c ..... Schmidt number.

S_t ..... Stokes' number.

t ..... Time.

T_L ..... Integral Lagrangian time scale.

u ..... Wind velocity in the along-wind direction.

u_* ..... Friction velocity.

U_S ..... Mean wind velocity in the alongwind- direction at source height.

v ..... Wind velocity in the cross-wind direction.

V_b ..... Bleeding velocity through a screen.

V_c ..... Critical velocity of rebound.

V_i ..... Particle impact velocity.

V_r ..... Particle rebound velocity.

V_{dep} ..... Deposition velocity.

V_{turb} ..... Turbulent deposition velocity.

w ..... Wind velocity in the vertical direction.

W ..... Windbreak width.

w_g ..... Particle gravitational settling velocity.

x ..... Distance in the along-wind direction.

y ..... Distance in the cross-wind direction.

z ..... Height.

z_0 ..... Roughness length.

Chapter 1

Introduction

Contents

1.1 Humans manipulate microclimate. 2

1.2 Aerial transport of heavy particles raises problematical issues 6

1.3 Windbreaks, a useful strategy to confine particle deposition? 7

1.4 Options for modelling heavy particle dispersion about/inside a windbreak. 9

1.4.1 Modelling particle dispersion in a given wind flow . . 9

1.4.2 Modelling the wind flow 14

1.4.3 Modelling particle filtration 18

1.5 Presentation of the thesis, and novelty of this work. 23

1.5.1 An analytical solution for particle deposition on uniform terrain accounting for the 'Crossing Trajectory Effect'. 23

1.5.2 Provision of new experimental data. 25

1.5.3 New evidence on the skills of a coupled RANS-LS model for heavy particle dispersion in a windbreak flow. 33

1.5.4 A new insight into the dispersion patterns of heavy particles in windbreak flow. 34

1.6 References. 35

Micro-meteorology is the study of meteorology at a local scale, typically in the atmospheric surface layer. Because this air region surrounds people and deeply affects their lives and activities, micro-meteorology is not limited only to theoretical studies that aim to understand the physical processes ruling micro-climates, but also encompasses human endeavours to change micro-climate by modifying the layout of landscapes. This thesis addresses the issue of heavy particle advective transfers, often seen as pollution drifts. It investigates the alteration of particle fluxes induced by the presence of a windbreak, with the objective of assessing the usefulness of setting up shelterbelts as a mitigation strategy.

This introductory section first illustrates the propensity of human beings to adjust their meteorological environment in order to meet their preferences and alleviate constraints. Issues pertaining to aerial transport of particles are then specifically pointed out, and the pertinence of windbreaks as a mitigation tool is put into question. The methodology to address this subject is discussed and the approach chosen is justified, in particular concerning numerical modelling which is key in the investigation. The content of the thesis is then outlined, insisting on the novelty of the work presented. Because provision of new experimental data is a major contribution of this work, the experiments are described and illustrated in detail.

1.1 Humans manipulate microclimate.

In one of the driest regions in the world, the Atacama desert North of Chile, plants manage to grow by capturing coastal fog on their leaves. This illustrates how beautifully living organisms adjust to get the most out of the microclimate

to sustain themselves. Human beings also take advantage of the resources offered by the meteorological environment. Inspired by nature, people set vertical mesh screens up in the air in a direction perpendicular to the prevailing wind (see Figure 1.1) in order to catch and harvest the water carried by fog. Fog droplets coalesce on the porous cloth and drip by gravity into a supply

Figure 1.1: Screen harvesting water droplets in coastal fog

network, thus providing water for small rural communities in arid regions. Wind is another resource exploited by men. In the past, wind mills harnessed the winds to grind grain. Today wind generators extract the inexhaustible source of energy to produce electricity.

Although our air environment constitutes a tremendous resource, it can be perceived as a constraint. Human beings then contrive to master and tame it, by shaping a microclimate that suits their preferences. Building houses is the most obvious example of this alteration of the living space. Climate is often altered outdoors too. In urban environments where summer temperatures reach uncomfortable levels, vegetation is planted to shade buildings and

consume heat by evapotranspiration. In hot and humid regions, streets may be oriented in the prevailing wind direction, thus causing air channeling. Enhanced air circulation avoids the build up of heat, humidity and pollution.

Remarkable ingenuity has also been demonstrated to modify the microclimate of plants. Champagne, the French region where the sparkling wine is produced, is a chilly region where ground temperatures often drop below freezing at dawn when the temperature inversion is strongest. Vineyards have proved susceptible to those radiative frosts, in particular during spring time when the fragile buds are growing. Thus spring frosts can severely jeopardize vintage (Madelin and Beltrando, 2005). Spraying chemicals (including maleic hydrazide, dimethyl sulfoxide or decenylsuccinic acid) on plant surfaces as a frost protection has proved quite efficient (Marlange, 1967; Burns, 1974). Clay or even water spraying are two useful alternatives to mitigate frosts. In effect, water droplets sprayed onto plants release latent heat as they freeze on contact with plants; the mixed ice/liquid water coating thus maintains a temperature near 0 °C and as a result prevents surface temperatures from dropping far below the freezing point. An alternative strategy consists in placing huge fans 10 m or so above ground. These are operated early in the morning when the temperature inversion is strongest and the ground temperature reaches its minimum. The fans force vertical mixing of the air, thus convecting warmer air from above down to the ground. Figure 1.2 shows the impact of a fan stirring the surface air layer on the temperature profile. The air mixing results in an increase of the ground temperature. When air is severely stratified, temperatures may be augmented by 5 to 10 degrees by this technique, thus avoiding a damaging frost. The technique is so efficient that vine-growers not equipped

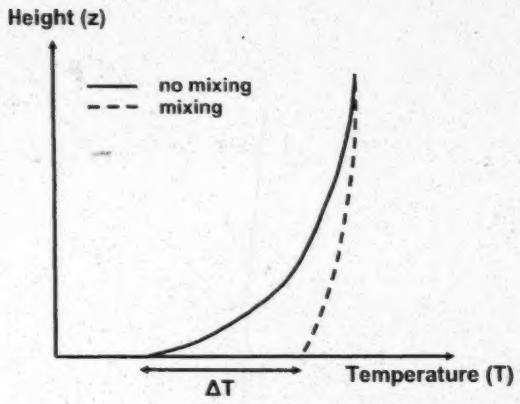

Figure 1.2: Schematic of temperature profiles in a stable atmosphere when the air is mixed artificially by a fan (dashed line) and when it is not (solid line)

with the fan system appeal to helicopters to operate the mixing (L'Humanité, 1997). These techniques are also used to protect cherry orchards from frost or promote drying of dew in British Columbia.

Another practice aimed at modifying microclimate for agricultural purposes is the sheltering of crops with barriers of vegetation. In addition to providing a habitat for wildlife (Johnson and Beck, 1988), this can improve crop yield (Kort, 1988; Boldesa et al. 2002) due to compound benefits including better water conservation (Dickey, 1988), better water use efficiency of plants (Davis and Norman, 1988), reduction of direct wind damage to plants (Papesch, 1992), and warmer microclimate (Cleugh and Hughes, 2002; Hodges et al., 2004). Because a windbreak decreases the wind intensity in its vicinity, it may also play a role in the mitigation of particle drift, which is problematical in numerous situations. This brings us from the general context of 'environmental manipulation' to the more specific content of my Ph.D. thesis,

i.e. understanding and possibly controlling the distribution of atmospheric particulates.

1.2 Aerial transport of heavy particles raises problematical issues

In regions of the world where snow is abundant, snow drifts (Shaw, 1988) on the road perturb traffic and affect people's everyday life. Environmental concerns are also raised by particle drift. Wind erosion for instance causes loss of soil fertility in susceptible arid regions (Li et al., 2004). In intensive yield-oriented agriculture, spraying crops with pesticides and fertilizers is a generalized practice. In windy situations, those chemicals drift away from their intended target (Woods et al., 2001). As chemical inputs represent a heavy load on a farmer's budget (Harris et al., 1998), spray drift causes significant economic losses. Furthermore, it pollutes the air (Gil and Sinfort, 2005), and the plants and soil which are unintentionally affected by the drifting chemicals may be contaminated. As sustainability in agriculture gains momentum as an environmental and societal issue (Horrigan et al., 2002), it has become a major concern to balance environmental 'purity' and productivity. In this context, attention to pollution by drifting chemicals has grown in recent years (Matthews and Thomas, 2000). Cultivation of Genetically Modified (GM) crops is increasingly common as it may allow to increase crop yield while reducing the application of chemical inputs (May, 2003; Bennett et al., 2004), thus improving accounts in both the profit and the pollution columns. This raises the issue of gene flow and genetical pollution of the environment (Klein et al., 2003), as GM genes, carried by wind-blown pollen, may contaminate

plants which are genetically related (Rieger et al., 2002). Consequently, control of gene flow is critical, and confinement of GM genes in their original crop is desirable.

All of the issues mentioned above pertain to heavy particle dispersion, and they illustrate the need to be able to gain insight in the dispersion mechanisms, to identify dispersive patterns. Taking a more practical perspective, it is necessary (for example in agronomy and agricultural engineering) to develop reliable tools allowing to quantify particle dispersion and to evaluate the associated pollution risks, in relation to meteorological conditions. The concerns raised by particle drift also point to the importance of finding efficient drift mitigation strategies and to quantify their impact.

1.3 Windbreaks, a useful strategy to confine particle deposition?

There is evidence that windbreaks are useful in the mitigation of particle drift[1] (Porskamp et al. 1994). A close look at the micrometeorology of windbreak flows is however necessary to gain insight on the impact of fences on particle dispersion. The flow disturbance created by a windbreak has been extensively documented, and the reader may refer for instance to Van Eimern et al. (1964), Plate (1971), McNaughton (1988, 1989) or more recently Cleugh (1998) and Wang et al. (2001). In short, drag of the windbreak on the flow causes reduced mean wind velocity near the ground in a region spanning roughly

[1] I will use the term 'drift' in relation to particulates (sprays, pollens,...) to connote their movement away from their intended locale of deposition, rather than in the more general sense of 'movement'.

$-5 \leq x/H \leq 30$, where x is the distance downwind of the fence and H is its height. A static pressure build-up immediately upwind from the windbreak (Wilson, 1997) deflects the approaching current, a fraction of which streams upwards over the windbreak. As a consequence of this 'channeling effect', a portion of the approaching wind is accelerated into a jet above the fence, while the current through the barrier (bleed flow) is decelerated by the adverse pressure gradient which spans roughly $-5 \leq x/H \leq 5$ (Wilson, 1997). The strong wind shear downwind from the fence thus created between the jet region above and the 'quiet zone' below produces turbulence in a so-called 'wake zone'; effectively this is a mixing-layer which transfers momentum downwards and progressively reaccelerates the sluggish zone beneath.

Reduction in the horizontal wind speed causes a gravitationally- settling particle plume to deposit closer to its source. However, the flow deflection upwards and the increased speed above a fence can result in some particles being carried further away than they otherwise would have been[2]. The complexities of a windbreak flow have then conflicting influences on the transport of airborne particles, and "in certain conditions barriers may enhance dispersal rather than retard it" (Nathan et al., 2005). Therefore the overall impact should be quantified; in this respect, as Ucar (2001) notes, little progress has so far been made. Given the complexities of a windbreak flow, numerical modelling is the necessary investigation tool. To test their skills, model outputs should however be compared with the 'real world' observations which they are designed to reproduce. Experimental work and data collection is thus an

[2]Of course one cannot speak meaningfully of where any one particle 'would have' deposited, with or without a windbreak, owing to the stochastic nature of particle paths in this turbulent (i.e. non-deterministic) system.

essential partner of numerical modelling.

1.4 Options for modelling heavy particle dispersion about/inside a windbreak.

1.4.1 Modelling particle dispersion in a given wind flow

The dispersion of particles can be modelled following either an Eulerian or a Lagrangian approach. The Eulerian approach consists in solving the particle mass budget equation in each bin of a mesh applied on the physical space, subject to an upwind boundary condition capturing the intensity and spatial distribution of the source. Because the particle plume is carried and dispersed by air flow in which it is embedded (advective transport), knowing the velocity field (or statistics of it) is a precursor to solving the concentration field. For atmospheric flows, generally only the mean velocity is resolved (see next paragraph for details) and as a result, only the mean concentration statistics can be computed. In effect, the concentration and velocity fields are decomposed into a resolved (mean) component and an unresolved (turbulent) component; the Reynolds-averaged mass conservation equation, assuming steady state and the non-existence of lateral gradients ($\partial/\partial y = 0$), is

$$\frac{\partial}{\partial x}\left(\overline{u}\,\overline{c} + \overline{u'c'}\right) + \frac{\partial}{\partial z}\left(\overline{w}\,\overline{c} + \overline{w'c'} - w_g\overline{c}\right) = 0 \qquad (1.1)$$

where $\overline{u}$ and $\overline{w}$ are the mean velocity components in the along wind (x) and vertical (z) directions, $\overline{c}$ is the mean concentration and w_g is the gravitational settling velocity of the heavy particles in a still fluid. In the process of time-averaging the mass budget equation, terms of cross-correlation between the

Eulerian velocity and the concentration ($\overline{u'c'}$ and $\overline{w'c'}$) appear; they represent the fluxes carried by the turbulent (unresolved) flow. Those terms, which are joint statistics of the flow and particle density fields, are unknown. The simplest approximation for them, the K-theory, assumes that turbulence disperses particles following a diffusive pattern, viz. the turbulent flux of particles is uniquely related to the mean gradient in particle concentration and to the turbulent diffusivity of the flow. This is termed 'first-order' closure of the mass budget equation. Alternatively, a more rigorous estimation of the turbulent flux terms may be determined by solving their budget equation (higher order closure). Yet again however, unknown terms of higher order (eg. $\overline{c'w'^2}$) representing transport by the unresolved flow are introduced. Ultimately in modelling those higher order joint $(c' - u_i')$ moments all existing theories invoke the gradient-diffusion assumption (K-theory) at some level, whatever the order of closure.

Yet, K-theory is fundamentally flawed. In effect in a diffusive regime a particle's position evolves as a Markovian process, i.e. particles follow a random walk in position and the particle's velocity is uncorrelated from one time step to the next. In contrast, because turbulent motions are coherent over finite length and time scales, fluid particle velocities are persistent during a time interval of order T_L, the Lagrangian time scale. Therefore although a diffusive treatment of turbulent transport may be appropriate in the 'far field' where the traveling time (t) of particles is sufficiently long ('far field' limit, when $t >> T_L$), it is inadequate otherwise. If one is to reconcile Taylors' (1921) Lagrangian solution for particle dispersion in homogeneous turbulence with the K-theory, then unless the 'far field' limit is reached, the turbulent diffusivity

has to be written as a function of the travel time t. Thus, two particles sampled at the same location and at the same time would be subject to different diffusivities depending on their respective traveling times. This is absurd in principle, as the turbulent diffusivity is supposedly a local property of the flow. The incongruity of this situation reveals the limitation of a diffusive treatment.

Another way to state the limited validity of K-theory is to focus on whether the turbulence carrying the unresolved flux is 'fine grained' relative to the dispersing plume (Corrsin, 1974). For K-theory to be a satisfactory approximation, the mean gradient in concentration should be approximately constant over displacements in position of the order of magnitude of the turbulent length scale. Observations of counter-gradient fluxes (Denmead and Bradley, 1985, 1987), wherein by definition turbulent diffusivity is negative, dramatically illustrate the limitations of the K-theory. It follows that the Eulerian treatment of particle dispersion is far from being universally applicable. In this context, it seems hopeless to expect an Eulerian model to handle skillfully the dispersion of particles about a windbreak, where sharp inhomogeneities in the mean flow field are conducive to strong particle concentration gradients. As a consequence, for the purposes of the present study, this option was discarded.

Alternatively a Lagrangian description of individual particle trajectories (based on the statistics of the carrying wind flow) may be adopted. It offers the major advantage of not calling for assumptions relative to the cross-correlation $\overline{u_i' c'}$ (Wilson, 2000), or more generally on any joint $(c' - u_i')$ statistics. Random walk models, also called Lagrangian Stochastic (LS) models, generate

an ensemble of particle trajectories for the given flow conditions, along which each particle is assumed to conserve its mass. This entails neglect of diffusive mass exchange with the surrounding air for gaseous particles, or neglect of evaporation for liquid particles[3]. Dispersion statistics, in particular the mean concentration field, are then derived from the displacement statistics of a large ensemble of particle trajectories.

Wilson and Sawford (1996) reviewed LS models for the dispersion of passive tracer particles. The simplest in a hierarchy of increasing complexity is the Random Displacement Model (or Zeroth-order LS model), which generates a random walk in position, ignoring the autocorrelation of a particle's velocity from one time step to the next. In that it is is equivalent to a diffusive treatment, it is therefore inadequate (as explained above) except in the far field of a source. In the first order LS model, velocity autocorrelation (along a particle's trajectory) is accounted for, and it evolves with time according to a generalized Langevin equation which specifies the velocity increment as the sum of a deterministic term and a stochastic term:

$$du_i = a_i(\mathbf{x}, t)dt + b_{ij}dW_i \tag{1.2}$$

where dW_i is a three dimensional Wiener process (white noise). The first term on the right hand side is a damping term which 'pushes' a particle's velocity to conform to the local Eulerian velocity probability density function of the fluid. The second is the stochastic term, and reflects the random fluctuations due to pressure and viscous forces exerted on a particle. The variables a_i and b_{ij} will be precisely defined in section 3.3.1.

[3]It is easy to accommodate such processes, e.g. radioactive decay, decreasing viability of spores, etc...

The Lagrangian stochastic theory is enticingly simple, and Lagrangian Stochastic models have seen a rapid growth in application since the early 1980's to model particle dispersion in atmospheric flows. However, extension of the theory to complex atmospheric turbulent flows has been difficult. Wilson et al. (1981a,b), when simulating the dispersion of particles with a LS model in the highly heterogeneous flow of a plant canopy, noted an abnormal accumulation of particles near the ground due to the vertical gradient in the variance of the vertical velocity. Wilson et al (1981c), followed by Legg and Raupach (1982) introduced heuristic corrections in the deterministic term of the Langevin equation to account for the heterogeneity in the vertical velocity variance. Similarly, extensions of the basic Langevin equation were introduced, still on an ad-hoc basis, to account for complexities of atmospheric flows such as non-stationarity and the non-Gaussianity of turbulence (Sawford, 1985). A few years later, Thomson (1987) brought a scientifically sound foundation to the design of the Langevin equation. He argued that LS models should be consistent with the similarity theory of Kolmogorov; more importantly he also proposed that LS models should be designed to ensure that particles which are initially well mixed in position-velocity space, should remain so with increasing time. This is known as the 'well mixed condition' (WMC) criterion, and it relates the necessary form of the Langevin equation to the Eulerian velocity probability density function of the background flow. The WMC criterion has proved extremely useful, for it provides a rigorous way to constrain the form of the deterministic term a_i. Yet the WMC does not suffice to determine uniquely the Langevin equation when multi-dimensional turbulence is considered, and to date no other criterion to further constrain the equation has been

found. Wilson and Flesch (1997) proposed the 'zero spin' criterion and Sawford (1999) refined this idea; however there are many possible zero-spin models and Thomson's solution has proven as good as others. By virtue of its simplicity it is considered as a standard (Wilson and Sawford, 1996), and Leuzzi and Monti (1998) gave evidence that it (i.e. Thomson's model) handled dispersion properly in highly heterogeneous flows. Sawford and Guest (1991) proposed simple but useful adjustments to extend the applicability of LS models to the dispersion of heavy particles, and Wilson (2000) showed that a 1st order LS model, that accounts for particle inertia without invoking its equation of motion, was capable of satisfactorily handling heavy particle dispersion over level terrain. Because this is the most reliable and promising approach to handle dispersion of heavy particles in a complex flow, the modelling is achieved in this present study with a 1st order LS model based on Thomson's formulation of the Langevin equation, which is adjusted to accommodate heavy particle dispersive peculiarities.

1.4.2 Modelling the wind flow

An LS model is said to be 'driven' by the wind velocity field, where the latter necessarily is described in terms of statistics (means, variances, cross-correlation, and dissipation rate of the turbulent kinetic energy). Because the parameterizations of the near-ground wind flow given by the Monin-Obukhov similarity theory do not hold in a windbreak flow, recourse to numerical modelling of the wind flow is necessary. In Direct Numerical Simulations (DNS), the flow is solved down to the finest turbulent scale (namely the dissipation scale) and therefore DNS fields are considered an exact reproduction of reality,

in so far as the Navier-Stokes equations (i.e. the mass and momentum budget equations) are flawless. Although DNS constitute the most reliable approach, they are not practical for atmospheric flows as they require prohibitive computer power.

Thirty five years ago, Deardorff (1970) proposed a numerical technique known as Large Eddy Simulation (LES), allowing to save computational expense (and therefore be more widely applicable), but at the same time retaining the essential physics governing the flow field. On the assumption that most of the momentum flux is carried by the large 'energy-containing' scales of motion, he suggested to resolve the flow down to those scales by using a sufficiently fine mesh resolution, but to parameterize the sub-grid scale motion. Many LES studies have been fairly successful at simulating atmospheric flows (e.g. Mason and Thomson, 1987; Kosovic and Curry, 2000), and the technique has proven a valuable tool to gain insight into flow patterns in the boundary layer. For instance, Mason (1989) identified with LES the flow structure of a convective boundary layer, i.e. downdrafts covering most of the surface area, where the flow converges into small narrow regions of updrafts. Yet, when the sub-grid scale motion carries a significant fraction of the turbulent fluxes, the closure scheme becomes critical and LES performance is affected by the uncertainties associated with the turbulence closure. Evidence shows that incorrect LES predictions occur in regions close to boundaries, or in a statistically stable fluid (Mason, 1994). In effect as thermal stability increases, or as the flow approaches a surface, the characteristic size of the eddies decreases, and the turbulent convection is increasingly 'accomplished' by the sub-grid scale model. Patton and Shaw (1998) simulated a windbreak flow using the LES technique,

and investigated its performance against wind tunnel velocity measurements. Although the mean flow proved to be well reproduced, the match was much less satisfactory for the streamwise and vertical velocity variances. Those disappointing performances may stem from (this is a speculation) an inaccurate sub-grid scale closure, revealed by the fact that the turbulent motions created by the windbreak had a characteristic length smaller than mesh spacing of the grid. To date, Patton and Shaw's (1998) study remains the only attempt to test LES for a windbreak flow against experimental data. Provisionally, it seems that LES does not necessarily provide a more reliable means to generate a windbreak flow field than the simpler (although still quite elaborate) 'Reynold's Averaged Navier Stokes' (RANS) approach.

In this latter numerical technique, the flow is decomposed into a resolved-scales component (the mean flow) and a fluctuating (turbulent, unresolved) component, and is then calculated by solving the time-averaged Navier Stokes equations (here in steady-state form, and assuming crosswind symmetry):

$$\frac{\partial}{\partial x}\left(\overline{u}^2 + \overline{u'^2} + \frac{\overline{p}}{\rho}\right) + \frac{\partial}{\partial z}\left(\overline{u}\,\overline{w} + \overline{u'w'}\right) = SU \qquad (1.3)$$

$$\frac{\partial}{\partial x}\left(\overline{w}\,\overline{u} + \overline{w'u'}\right) + \frac{\partial}{\partial z}\left(\overline{w}^2 + \overline{w'^2} + \frac{\overline{p}}{\rho}\right) = SW \qquad (1.4)$$

$$\frac{\partial \overline{u}}{\partial x} + \frac{\partial \overline{w}}{\partial z} = 0 \qquad (1.5)$$

Here SU and SW are momentum sink terms which account, in our situation, for the drag exerted by the windbreak on the flow. The reader will recognize the budget equation for the horizontal momentum (Eq. 1.3), for the vertical momentum (Eq. 1.4) and the continuity equation (Eq. 1.5); as a reminder p represents the static pressure departure from an adiabatic and hydrostatic

reference state, and ρ is the mean air density. The prime symbol indicates an unresolved component of the flow, whereas bars pertain to the resolved scales of motion. The RANS equations are non linear and therefore are solved by iteration. The momentum fluxes carried by the unresolved scales of motion (the Reynold's stresses) are unknowns and must be modelled to close the equations. They are either parameterized (first order closure) assuming a gradient-diffusion scheme (i.e. invoking the K-theory, as explained earlier in the case of scalar diffusion), or estimated by solving their budget equation (second-order closure).

The first attempts to numerically solve the complex flow about a windbreak with a RANS model date back to the early 80's with Durst and Rastogi (1980) and Hagen et al. (1981), although earlier authors had examined the related problem of the effect of distributed drag on incident flow (eg. Lozowski, 1969). A few years after these first attempts, Wilson (1985) showed how a thin porous barrier should properly be represented in such numerical studies, and compared the skills of first and second order RANS closures to reproduce the flow impinging on a porous fence at perpendicular incidence, in a neutrally stratified atmosphere, as observed by Bradley and Mulhearn (1983). He concluded that RANS models simulate the mean velocity field reasonably well, noting that the gain in accuracy obtained with a second-order closure was only modest. Similar sentiments have been expressed by many authors for many other disturbed flows. He pointed out however that, irrespective of the closure option, the sharp acceleration over the fence was not very skillfully reproduced in low resolution solutions (these were not claimed to be grid independent), resulting in a slower rate of recovery than observed. More recently Wilson

(2004a) observed experimentally that thermal stratification and obliquity of the approaching flow reduced the sheltering effect of a fence. He subsequently tested (Wilson, 2004b) the ability of second-order RANS closures to capture this effect. Whereas the thermal stability impact was quite well mimicked, the response to obliquity was found to be excessive. i.e. the model underestimated the sheltering effect in oblique winds. He also pointed out that the RANS-simulated velocity variances compared poorly with observations, in the wake of the fence.

Despite these known weaknesses of the RANS approach, I considered the RANS model was the best option available to simulate the wind flow about a windbreak. The alternative LES technique is vastly more cumbersome to implement, and hasn't (yet) proven to be more skillful, as mentioned above. A second-order closure was preferred to the simpler first-order closure because it offers a "far more reliable approach to predicting complex flows than any eddy-diffusivity based model" (Launder, 1989), and because it more naturally accounts for thermal stratification (Wilson, 2004b).

1.4.3 Modelling particle filtration

Different approaches can be followed to treat the dispersion of particles by a natural shelterbelt, differing in the level of detail at which they describe the phenomenon. In the coarsest approach, the windbreak is considered as a whole unit in which the motion of particles is not explicitly described; the bulk particle entrapment efficiency can be determined from formulations derived for engineering purposes such as air filtration. In particular the filtration

of aerosols with fibrous thick filters has been extensively documented (see for instance Shaw, 1978), and presents obvious similarities with our situation, for vegetation elements constitute (in essence) 'cascade impactors'. The development of the theory of filtration on fibrous filters was built on achievements in aerodynamics of flow around a cylinder which started in the early 1930's with calculations of an idealized potential flow (Albrecht, 1931; Sell, 1931). The principles of the modern theory of particle deposition on a cylinder were formulated by Langmuir (1942). The total efficiency of a filter can be formulated as (Shaw, 1978)

$$E_F = 1 - \exp\left(-\frac{2E_{\mathrm{df}}\alpha d_f}{\pi a}\right) \tag{1.6}$$

where a is the diameter of the fibers, d_f is the thickness of the filter, α the packing density coefficient and E_{df} the single fiber efficiency of deposition. E_{df} is determined by solving the equation of motion for particles in a prescribed flow field. The flow bleeding through an array of cylinders arranged perpendicularly to it is well known (Shaw, 1978).

Corn leaves however are ribbon-shaped foils which are not necessarily oriented perpendicular to the flow, as Figure 1.3 indicates. Because the filter structure significantly affects the flow and ultimately the efficiency of a filter, the relevance of ideal flow models proposed for an array of cylinders is questionable. Admittedly, this problem could be overcome by estimating the flow around leaves in a more realistic way. When leaves are oriented neither parallel not perpendicular to the impinging wind, the air is diverted up over a certain distance along the leaf, before spilling around the edges. So far as I know, the solution for such a 3-d flow does not exist. The 2-d viscous flow about a ribbon

Figure 1.3: Corn leaves: not cylinders, not regular, and living in a turbulent flow.

oriented parallel or perpendicular to the flow is well known (Milne-Thomson, 1960) however, and the 3-d flow for intermediate angles could be estimated by linear interpolation between those two limits (Aylor, 1975). In this respect, the modelling of a bulk filter efficiency could be adjusted.

But more serious issues make this treatment of particle entrapment inapplicable to our situation. First of all, whereas the engineering models assume a steady and laminar approaching flow, the wind inside a natural shelterbelt is turbulent. In other words, the 'host flow' in which the obstacles are embedded is very heterogeneous and variable in time. As a result, the impact of the flow on deposition cannot be captured by a deposition efficiency (E_{df}) valid throughout the whole hedge. In addition, and most importantly, the host flow

(as opposed to the local flow around each impediment) inside the shelter belt is 3-dimensional whereas the formulation of filtration efficiency for an artificial filter assumes a 2-d flow. The three dimensionality stems from two factors: (i) the approaching flow as well as the structure of the vegetation are height dependent; (ii) the hedge has a finite height delimited by a bottom (ground) and a top boundary across which particle may escape the filter. It follows that this modelling strategy is not applicable to our complex situation.

An alternative approach, at the other end of the 'level of description scale', would consist in solving for the motion of particles inside the shelter-belt, accounting explicitly for the influence of the vegetation elements on the trajectories. This treatment requires to have a description of the windflow around each vegetation element, whose complex boundary demands an intricate mesh: a level of detail it was not realistic to attempt to provide even using a RANS model. To the contrary, feasible RANS computations yield the wind flow inside the corn belt in terms of *spatially averaged* statistics. In other words, the RANS computations handle the vegetation as a 'diffuse material' acting as a spatially-continuous sink of momentum. Effectively, the drag $SU(x,z)$ on the horizontal flow exerted by vegetation, is parameterized as

$$SU(x,z) \propto C_{\mathrm{d}}\, A(x,z)\, \overline{u}\, \sqrt{\overline{u}^2 + \overline{v}^2} \tag{1.7}$$

where C_{d} is the in situ drag coefficient, $A(x,z)$ is the vegetation area density (m^{-1}) and (as earlier) $\overline{u}$, $\overline{v}$ are the horizontal components of the mean velocity, respectively perpendicular and parallel to the fence. To restate the matter, the RANS model as here implemented does not solve the flow field explic-

itly in the vicinity of the vegetation impediments. The ideal way to proceed would be to compute the flow by DNS (Direct Numerical Simulation). Yet, as mentioned earlier, DNS is not practical as it requires computational power which is prohibitively high with the scales of motion we are concerned with. Because leaves have fairly simple geometrical shapes (finite length ribbons), an approximate analytical air flow about a leaf could be achieved, as mentioned earlier. Each time a particle entered in a zone affected by a specific vegetation element, the LS model could be provided appropriate velocity statistics for the local flow around the obstacle, given a host flow provided by the RANS model.

This approach is not only awkward, it is also unnecessary. The impaction efficiency of particles impinging on impactors has been experimentally measured on ideal obstacles (May and Clifford, 1967). Aylor (1982) provided a parameterization which fits May and Clifford's (1967) data for the impaction efficiency on a ribbon.

$$E_I = \frac{0.86}{1 + 0.442\, S_t^{-1.967}} \tag{1.8}$$

where $S_t = |v|\tau_p / L_v$ is the Stokes' number of the particle to the vegetation element, τ_p is the inertial time scale of a particle and L_v is the characteristic size of a vegetation element. It is therefore possible to handle the regions surrounding the vegetation elements as black boxes where the flow is not solved. Supplying the velocity of the host flow (available from the RANS simulations) and the orientation and dimension of the leaves (described in statistical terms derived from measurements) allows to determine the impaction efficiency. This is the third and intermediate approach, which has previously been used with success (eg. Jarosz et al., 2004). We follow this treatment in our modelling.

Upon impact on a vegetation element, a particle may rebound or remain stuck on its surface. Following Dahneke (1971, 1975), the rebound can be described in terms of an energy budget. A particle will rebound if its kinetic energy before impact is larger than the energy lost to adhesive forces and plastic deformation. The terms of the budget depend on the material of the particle and of the impactor's surface, and also on the angle of incidence of the particle's trajectory to the surface (Xu and Willeke, 1993). Paw U (1983) showed that the theoretical description of Dahneke (1975) satisfactorily captures observations of particle rebound on a cylinder. For practical purposes, Paw U (1983) identified a critical rebound velocity above which particles rebound. From his experimental measurements, he provides values for this rebound velocity and for the ratio of rebound velocity over impact velocity (V_r/V_i) for various particles and impinging surface materials, including glass and leaves of various plant species. He found that those quantities were fairly constant across the type of surface of the impactor, but however were highly dependent on the type of particles. For the purposes of this study, we retained the values measured for glass beads.

1.5 Presentation of the thesis, and novelty of this work.

1.5.1 An analytical solution for particle deposition on uniform terrain accounting for the 'Crossing Trajectory Effect'.

Chapter 2 of this study addresses the dispersion of heavy particles over uniform terrain. Availability of tools readily exploitable allowing to quantify

dispersion in relation with the meteorological conditions and the aerodynamical characteristics of the dispersing particles is of practical interest for pollution risk management. Wilson (2000) showed evidence that deposition of heavy particles could be satisfactorily simulated numerically. Whereas numerical models may be complicated to implement, an analytical solution is far more accessible, in particular to users in the 'real world' outside academia. In turn this work provides instead an analytical description for the deposition swath of heavy particles released from an elevated source. A few decades ago, Godson (1958) provided such an analytical solution; yet it performed poorly for it ignored a fundamental trait of heavy particle dispersion, viz. the Crossing Trajectory Effect (CTE). This phenomenon can be grasped in simple terms as follows: the paths of passive tracers and heavy particles differ, as the latter settle under gravity and, as a result of inertia, do not respond to the highest frequency motions of the driving turbulent fluid. In turn, they do not follow the flow streamlines, and the velocity auto-correlation of the driving fluid surrounding particles is reduced. In this study, Godson's (1958) analytical solution is re-examined and further developed, correcting the particle diffusivity for the CTE. This solution is a valuable investigation tool, as it provides clear insight into the parameters controlling dispersion. In addition, simple formulae relating the statistics of the deposition swath to the variable $\overline{u}(H_s)/w_g$ (ratio of the mean horizontal wind speed at source height to the particle settling velocity) are derived. This has real practical interest, for this variable is easily accessible and allows to capture the main features of the deposition pattern.

1.5.2 Provision of new experimental data.

The rest of this thesis work revolves around windbreaks, as a structure which interferes with particle dispersion patterns and could possibly be engineered to mitigate particle off-target drift. A windbreak alters the dispersion of a particle plume passing in its vicinity in two ways. Firstly it creates a marked disturbance in the windflow carrying dispersing particles. Secondly a fraction of the particles flowing through it remains entrapped on its constitutive elements. In this respect a windbreak plays the role of a particle filter. Prior experimental data pertaining to heavy particle dispersion in a windbreak flow do not exist, to my knowledge. Caput et al. (1973) measured ground deposition and concentration of particles released from ground upwind from a porous or impervious thin windbreak. However, the particles were aerosols of a diameter less than 5 μm, which behave therefore virtually like passive tracer particles. In turn those observations did not suit our purposes. Therefore experiments were carried out in this thesis work, with the objective of collecting a set of data against which the skills of the modelling tool could be tested.

In a first set of runs, the focus was on the impact of the disturbance of the flow by a fence on the dispersion patterns. Heavy particles were dispersed in a wind flow disturbed by an artificial thin windbreak (1 m high, 100 m long), the terrain being otherwise flat. They were collected downwind along a transect lined up with the prevailing wind direction, thus allowing to estimate the particle flux to ground along the deposition swath. The windbreak (seen on Figure 1.4) was porous and made of a plastic mesh with fine pores (2×2 mm^2) and narrow threads (1 mm in diameter). It stood downwind from

the source and was sufficiently long (100 m) to assume an infinite windbreak, i.e. the wind flow at the end of the windbreak did not affect the dispersing plume of particles. Its resistance coefficient $k_r = \Delta p/\rho U^2$ (where Δp is the pressure drop across the fence, and U is the bulk horizontal velocity of the flow bleeding through it; ρ is the air density) was measured in a wind tunnel by measuring the pressure upwind and downwind from a patch of windbreak material clamped to the wall of the tunnel; measurements of the pressure drop were carried out for wind velocities ranging from 0.4 to 10 m s^{-1} and are presented in Figure 1.5. The resistance coefficient decreases as the wind velocity increased. This type of dependency has been previously observed with certain types of screen fabric (Pinker and Herbert, 1967); it remains however relatively mild here. In standard meteorological conditions the velocity across the fence is of order 1 m s^{-1}, and the resistance coefficient is about $k_r \approx 1.8$. This numerical value was used as an input parameter in the RANS model to calculate the drag of the fence on the flow.

The particles were spherical glass beads of density $\rho = 2500\,\mathrm{kg\ m^{-3}}$ and of diameter d_p spanning $10 \leq d_\mathrm{p} \leq 50$ μm as Figure 1.6 shows. They were released from either a point source or a line source place parallel to the fence. As the windflow about an infinitely long fence is statistically two dimensional (no gradients in the direction parallel to the fence, i.e. $\frac{\partial}{\partial y} = 0$), using a line source allows to produce a particle concentration field which is also two dimensional, and thus is easier to model numerically. The line source was 15.75 m long and composed of nine point sources placed 1.75 m apart as shown on Figure 1.7.

Figure 1.4: Artificial fence (1 m high, 100 m long) erected in a straight fashion on a flat terrain

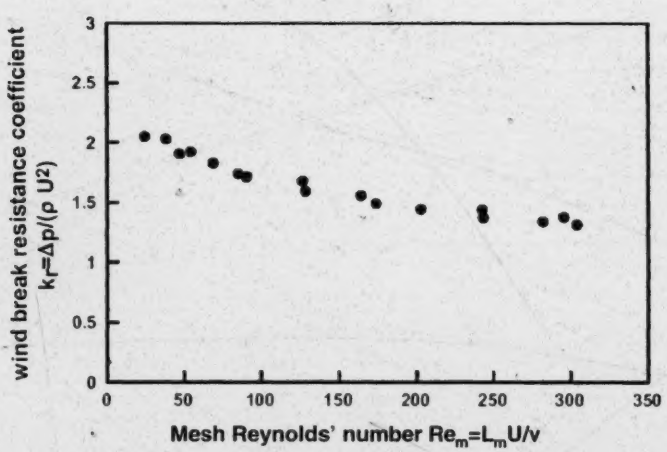

Figure 1.5: Resistance coefficient of the screen fabric measured in wind-tunnel, as a function of the Reynolds' number Re_{m} based on the fabric mesh size $L_{\mathrm{m}} = 2$ mm.

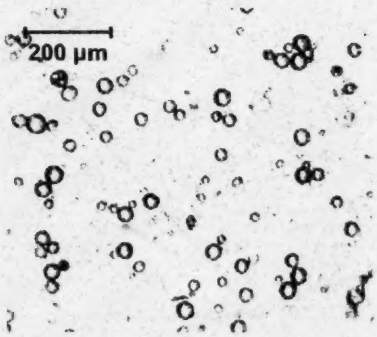

Figure 1.6: Spherical glass beads spread over a glass strip coated with glycerin

The point sources used are described in detail in section 3.2.1. It was anticipated that at some distance downwind, the plumes of the neighbouring sources would merge and would be equivalent to the plume released by a true line source. However, as explained in detail in appendix A-4, homogeneity along the lateral direction (i.e. parallel to the fence and to the line source) was not achieved. In turn, the model used was designed to capture the dispersion of particles in three dimensions. To measure deposition, particles were collected downwind in Petri dishes placed on a square tile to keep them leveled (Figure 1.8). Ideally, particles should be collected on flat surfaces. However, it was found (See appendix A-5 for details) that the short walls (18 mm) of the dishes did not interfere noticeably with deposition. The collectors were filled with an electrolyte solution; the particle laden liquid was then sampled and particles were counted with an automated machine (Details on the quality of the automated count are given in appendix A-6). The second set of experiments focused on the dispersion of particles within a natural corn shelterbelt which played the role of a particle filter. The shelterbelt was composed of 4

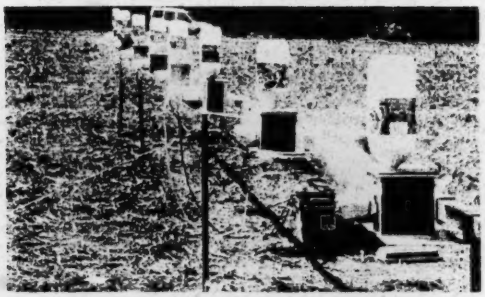

Figure 1.7: Line source composed of nine point sources lined up parallel to the windbreak

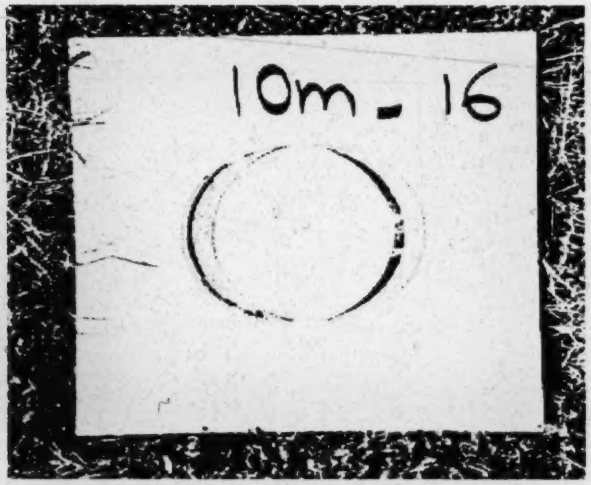

Figure 1.8: Petri dish filled with liquid and placed on a squared tile, used as a collector of beads depositing on ground.

rows of plants. It was about 3.2 m thick and 1.8 m high. A frontal view of the corn belt is shown on Figure 1.5.2, whereas Figure 1.10 presents a view in between two rows of plants.

Figure 1.9: Corn shelterbelt seen from outside

The experiment provided measurements of deposition fluxes on ground inside the corn belt, as well as observations of the flux carried by the mean flow across the vertical faces of the (thick) 'hedge'. Particle deposition on the ground was collected at eight locations spread evenly inside the hedge along a transect crossing it, following the same procedure as in the first set of experiments. The flux across the vertical faces was reconstructed as

$$F(z) = \overline{u}(z)\overline{c}(z) \tag{1.9}$$

where $\overline{u}(z)$ is the mean horizontal velocity perpendicular to the face, measured with a wind-cup and $\overline{c}(z)$ is the mean concentration in particles. The instrument used to measure concentration is described in section 4.2.2. Figure 1.11 shows the vertical profile of cup anemometers used to infer the average profile of horizontal velocity over the course of each run. Unfortunately, this photo-

Figure 1.10: Corn shelterbelt viewed from inside, between two rows of plants.

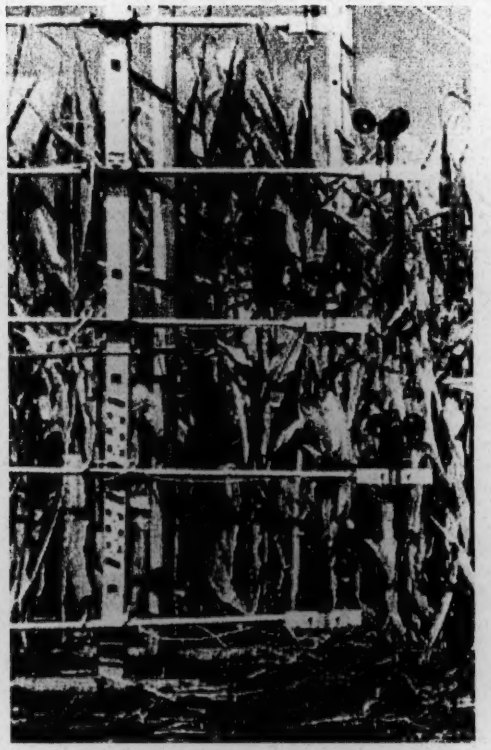

Figure 1.11: Vertical profile of wind cup anemometers measuring the horizontal velocity immediately upwind of the corn shelterbelt

graph does not show the instrument which trapped particles for concentration observations. The reader may imagine those instruments fixed at the opposite ends of the bars supporting the cup anemometers. Those data were used to test the numerical simulation of a Lagrangian Stochastic model which accounts explicitly for particle interaction with vegetation elements, viz. interception and deposition or rebound.

1.5.3 New evidence on the skills of a coupled RANS-LS model for heavy particle dispersion in a windbreak flow.

While particle dispersion over a level undisturbed terrain can be captured satisfactorily by analytical modelling, the complexities in the flow generated by the presence of a windbreak demand numerical investigation. In chapters 3 and 4, results of a coupled RANS-LS model for the dispersion of heavy particles about and inside a windbreak are presented and the performance of numerical simulations is analyzed in the light of the new experimental data collected during this Ph.D. study. Chapter 3 focusses on the impact of the flow disturbance generated by the presence of a fence on the deposition swath of heavy particles released from an elevated source. In chapter 4, the focus is on the impact of a thick natural windbreak as a filter of particles. A module treating particle deposition/rebound onto vegetation is added to the algorithm of the RANS-LS model in order to simulate the motion of particles traveling inside the hedge. The skills of the model are evaluated from a comparative study of the numerical simulations with the experimental results, in terms of deposition flux inside the hedge as well as particle concentration and streamwise fluxes along vertical profiles immediately upwind and downwind from the

shelterbelt.

1.5.4 A new insight into the dispersion patterns of heavy particles in windbreak flow.

The specific topic of heavy particle dispersion in a windbreak flow has never been examined to my knowledge. The RANS-LS model, after being validated as a satisfactory tool of investigation, is utilized to evaluate the overall effect of a windbreak on heavy particle dispersion. Chapter 3 examines how critical features of the windflow disturbance affect particle dispersion, with a highlight on deposition swath alteration. Subsequently, in chapter 4, the investigation focuses on the dispersion patterns inside and in the close vicinity of a natural (thick) shelterbelt. The effect of particle filtering by vegetation combined with the windflow disturbance on particle fluxes across the four boundaries of a thick windbreak and on the particle mass budget are under scrutiny. The analysis and discussion provided brings a valuable insight into the subject, which has received little attention (Ucar, 2001).

1.6 References.

Albrecht, F., 1931: Theoretical examinations on the sedimentation of dust from moved air and their application for the theory of dust filters. *Physikalische Zeitshrift*, **32**, 48-56.

Aylor, D. E., 1975: Deposition of particles in a plant canopy. *J. Appl. Meteorol.*, **14**, 52-57.

Aylor, D. E., 1982: Modeling spore dispersal in a barley crop. *Agric. Meteorol.*, **26**, 215-219.

Bennett, R., Y. Ismael, S. Morse, B. Shankar, 2004: Reductions in insecticide use from adoption of Bt cotton in South Africa : impacts on economic performance and toxic load to the environment. *J. Agric. Sci.*, **142**, 665-674.

Boldesa, U., A. Golbergb, J. Marañón Di Leoa, J. Colmana and A. Scarabino, 2002: Canopy flow and aspects of the response of plants protected by herbaceous shelterbelts and wood fences. *Journal of Wind Engineering and Industrial Aerodynamics*, **90**,1253-1270.

Bradley, E. F. and P. J. Mulhearn, 1983: Development of velocity and shear stress distributions in the wake of a porous shelter fence. *J. Wind. Eng. Ind. Aerodyn.*, **15**, 157-168.

Burns, R. M., 1974: Effects of spraying chemicals on young citrus trees for frost

protection. *California agriculture* **28**, 13-14.

Caput, C., Y. Belot, G. Guyot, C. Samie and B. Seguin, 1973: Transport of diffusing material over a thin wind-break. *Atmos. Environ.*, **7**, 75-86.

Cleugh, H. A., 1998: Effects of windbreaks on airflow, microclimates and crop yields. *Agroforestry Systems*, **41**, 55-84.

Cleugh H.A. and D. E. Hughes, 2002: Impact of shelter on crop microclimates: a synthesis of results from wind tunnel and field experiments. *Aust. J. Exp. Agric.*. **42**, 679-701.

Corrsin, S., 1974: Limitations of gradient transport models. *Advances in Geophysics*, **18A**, Academic Press, 25-60.

Dahneke, B. J., 1971: Capture of aerosol particles by surfaces. *J. Colloid. Interface Sci.*, **37**, 342.

Dahneke, B. J., 1975: Kinetic-theory of escape of particles from surfaces. *J. Colloid. Interface Sci.*, **50**, 89-107.

Davis, J. E., J. M. Norman, 1988: Effects of shelter on plant use efficiency. *Agric. Ecosystem Environ.*, **22/23**, 393-402.

Deardorff, J.W.: 1970: A numerical study of three-dimensional turbulent channel flow at large Reynold's numbers. *J. Fluid Mech.*, **41**, 453-480.

Denmead, O.T. and E. F. Bradley, 1985: Flux-gradient relationships in a forest canopy. *B.A. Hutchison and B.B. Hicks (Editors), The Forest-Atmosphere Interaction. Reidel, Dordrecht*, pp. 421-442.

Denmead, O.T. and E. F. Bradley, 1987: On scalar transport in plant canopies. *Irrig. Sci.*, **8**, 131-149.

Dickey, L. D., 1988: Crop water use and water conservation benefits from windbreaks. *Agric. Ecosystems Environ.*, **22/23**, 381-392.

Durst, F. and A. K. Rastogi, 1980: Turbulent flow over two dimensional fences, in Turbulent Shear Flows 2. Springer-Verlag, Berlin, pp. 218-232.

Gil, Y., C. Sinfort, 2005: Emission of pesticides to the air during sprayer application: A bibliographic review. *Atmos. Environ.*, **39**, 5183-5193.

Godson, W. L., 1958: The diffusion of particulate matter from an elevated source. *Archiv. F. Met. Geophys. und Biokl. A* **10**, 305-327.

Hagen, L. J., E. L. Skidmore, P. L. Miller, J. E. Kipp, 1981: Simulation of effect of wind barriers on airflow. *Trans. ASAE*, **24**, 1002-1008.

Harris, M., B. Ree, J. Cooper, J. Jackman, J. Young, R. Lacewell, A. Knutson, 1998: Economic impact of pecan integrated pest management implementation in Texas. *J. Econ. Entomol.*, **91**, 1011-1020.

Hodges L., M. N. Suratman, J. R. Brandle, 2004: Growth and yield of snap beans as affected by wind protection and microclimate changes due to shelterbelts and planting dates. *Hortscience*, **39**, 996-1004.

Horrigan, L., R. S. Lawrence, P. Walker, 2002: How sustainable agriculture can address the environmental and human health harms of industrial agriculture. *Environ. Health Perspect.*, **110**, 445-456.

Jarosz, N, B. Loubet, L. Hubert, 2004: Modelling airborne concentration and deposition rate of maize pollen source. *Atmos. Environ.*, **38**, 5555-5566.

Johnson, R. J. and M. M. Beck, 1988: Influences of shelterbelts on wildlife management and biology. *Agric. Ecosystem Environ.*, **22/23**, 301-335.

Klein, E. K., X. Foueillassar, P. H. Gouyon, C. Laredo, 2003: Corn pollen dispersal: Quasi-mechanistic models and field experiments. *Ecol. Monogr.*, **73**, 131-150.

Kort, J., 1988: Benefits of windbreaks to field and forage crops. *Agric. Ecosystems Environ.*, **22/23**, 165-190.

Kosovic, B., J. A. Curry, 2000: A Large-Eddy Simulation study of a quasi-steady, stably stratified atmospheric boundary layer.

Langmuir, I, 1942: Report on smokes and filters, OSRD No. 865, Office of Scien-

tific Research and Development, Office of Technical Services, Washington, DC.

Launder, B. E., 1989: Second-moment closure: Present and future? *Int. J. Heat Fluid Flow*, **10**, 282-300.

Legg, B. J., Raupach M. R., 1982: Markov chain simulation of particle dispersion in inhomogeneous flows: The mean drift induced by a gradient in Eulerian velocity variance. *Boundary-Layer Meteorol.*, **24**, 3-13.

Leuzzi, G., P. Monti, 1998: Particle trajectory simulation of dispersion around a Building. *Atmos. Environ.*, **32**, 203-214.

Li, F. R., L. Y. Zhao, T. H. Hua Zhang, T. H. Zhang, Y. Shirato, 2004: Wind erosion and airborne dust deposition in farmland during spring in the Horqin Sandy Land of eastern Inner Mongolia, China. *Soil Tillage Res.*, **75**, 121 - 130.

L'humanité, 1997: Printemps dévastateur dans les vignes et vergers du Sud. *Journal l'Humanité*, 23rd April 1997. Available online at http://www.humanite.fr/journal/1997-04-23/1997-04-23-777262.

Lozowski, E.P., 1969: Numerical simulation of flow through and around a dilute localized assemblage of particles. Ph.D. thesis, University of Toronto (Department of Physics).

Madelin M., G. Beltrando, 2005: Spatial interpolation-based mapping of the spring frost hazard in the Champagne vineyards. *Meteorol. Appl.*, **12**, 51-56.

Marlange, R. C., 1967: Ability to induce frost resistance in vines using leaf sprays of chemicals. *Phyton*, **87**, 87.

Mason, P. J., 1989: Large-Eddy Simulation of the convective atmospheric boundary layer. *J. Atmos. Sci.*, **46**, 1492-1516.

Mason, P. J., 1994: Large-Eddy Simulation: a critical review of the technique. *Q. J. R. Meteorol. Soc.*, **120**, 1-26.

Mason, P. J., D. J. Thomson, 1987: Large-Eddy Simulations of the neutral-static-stability planetary boundary layer. *Q. J. R. Meteorol. Soc.*, **113**, 413-443.

Matthews, G. A and N. Thomas, 2000: Working towards more efficient application of pesticides. *Pest Manag. Sci.*, **56**, 974-976.

May, K. R., R. Clifford, 1967: The impaction of aerosol particles on cylinders, spheres, ribbons and discs. *Ann. Occup. Hyg.*, **10**, 83-95.

May, M. J., 2003: Economic consequences for UK farmers of growing GM herbicide tolerant sugar beet. *Ann. Appl. biol.*, **142**, 41-48.

McNaughton, K. G., 1988: Effects of windbreaks on turbulent transport and microclimate. *Agric. Ecosystems Environ.*, **22/23**, 17-39.

McNaughton, K. G., 1989: Micrometeorology of shelter belts and forest edges.

Phil. Trans. R. Soc. Lond., **B 324**, 177-194.

Milne-Thomson, L.M., 1960: *Theoretical hydrodynamics.* Macmillan, 660p.

Nathan, R., 2005: Long-distance dispersal research: building a network of yellow brick roads. *Diversity and Distributions*, **11**, 125-130.

Papesch, A. J. G., 1992: Wind tunnel test to optimize barrier spacing and porosity to reduce wind damage in horticultural shelter systems. *J. Wind Eng. Ind. Aerod.*, **44**, 2631-2642.

Patton, E. G. and R. H. Shaw, 1998: Large-Eddy Simulation of windbreak flow. *Boundary-Layer Meteorol.*, **87**, 275-306.

Paw U, K. T., 1983: The rebound of particles from natural surfaces. *J. Colloid Interface Sci.*, **93**, 442-452.

Pinker, R. A., M. V. Herbert, 1967: Pressure loss associated with compressible flow through square mesh wire gauzes. *J. Mechanical Engineering Sci.*, **9**, 11-23.

Plate, E. J., 1971: The aerodynamics of shelterbelts. *Agric. Meteorol.*, **8**, 203-222.

Porskamp H. A. J., J. M. G. P. Michielsen, J. F. M. Huismans, 1994: The reduction of the drift of pesticides in fruit growing by a windbreak. *IMAG-DLO*

report 94-29, Institute of Agricultural and Environmental Engineering, Wageningen, Netherlands. 29 pp.

Rieger, M. A., M. Lamond, C. Preston, S. B. Powles, R. T Roush, 2002: Pollen-mediated movement of herbicide resistance between commercial canola fields. *Science : (Wash. D.C.)*, **296**, 2386-2388.

Sawford, B. L., 1985: Lagrangian statistical simulation of concentration mean and fluctuation fields. *J. Clim. Appl. Meteorol.*, **24**, 1152-1166.

Sawford, B. L., 1999: Rotation of trajectories in Lagrangian stochastic models of turbulent dispersion. *Boundary-Layer Meteorology*, **93**, 411-424.

Sawford, B. L., F. M. Guest, 1991: Lagrangian statistical simulation of the turbulent motion of heavy particles. *Boundary-Layer Meteorol.*, **54**, 147-166.

Sell, W., 1931: Procedures for investigation of air filters. *Z. Verein. Deutsches Ing.*, **75**, 295-296.

Shaw, D. L., 1988: The design and use of living snow fences in North America. *Agric. Ecosystems Environ.*, **22/23**, 351-362.

Shaw, D. T., 1978: Fundamentals of aerosol science. Wiley, New York, 372pp.

Taylor, G. I., 1921: Diffusion by continuous movements. *Proc. London Math. Soc. Ser.*, **2**, 196-212.

Thomson, D. J., 1987: Criteria for the selection of stochastic models of particle trajectories in turbulent flows. *J. Fluid. Mech.*, **180**, 529-556.

Ucar, T., F. R. Hall, 2001: Windbreaks as a pesticide drift mitigation strategy: a review. *Pest Manag. Sci.*, **57**, 663-675.

Van Eimern, J., R. Karschon, L. A. Razumova, G. W. Robertson, 1964: Windbreaks and shelterbelts, *World Meteorol. Org. Technical Note*, **59**, 191 pp.

Wang, H., E. S. Takle, J. M. Shen, 2001: Shelterbelts and windbreaks: Mathematical modeling and computer simulations of turbulent flows. *Annu. Rev. Fluid Mech.*, **33**, 549-586.

Wilson, J. D., 1985: Numerical studies of flow through a windbreak. *J. Wind Eng. Indust. Aero.*, **21**, 119-154.

Wilson, J. D., 1997: A field study of the mean pressure about a windbreak. *Boundary-Layer Meteorol.*, **85**, 327-358.

Wilson, J. D., 2000: Trajectory models for heavy particles in atmospheric turbulence: comparison with observations, *J. Appl. Meteorol.* **39**, 1894-1912.

Wilson, J. D., 2004a: Oblique, stratified winds about a shelter fence. Part I: Measurements. *J. Appl. Meteorol.*, **43**, 1149-1167.

Wilson, J. D., 2004b: Oblique, stratified winds about a shelter fence. Part II: Comparison of measurements with numerical models. *J. Appl. Meteorol.*, **43**, 1392-1409.

Wilson, J.D., G.W. Thurtell, G.E. Kidd, 1981a: Numerical simulation of particle trajectories in inhomogeneous turbulence. I. Systems with constant turbulent velocity scale. *Boundary-Layer Meteorol.*, **21**, 295-313.

Wilson, J.D., G.W. Thurtell, G.E. Kidd, 1981b: Numerical simulation of particle trajectories in inhomogeneous turbulence. II. Systems with variable turbulent velocity scale. *Boundary-Layer Meteorol.*, **21**, 423-441.

Wilson, J.D., G.W. Thurtell, G.E. Kidd, 1981c: Numerical simulation of particle trajectories in inhomogeneous turbulence. III. Comparison of predictions with experimental data for the atmospheric surface-layer. *Boundary-Layer Meteorol.*, **21**, 443-463.

Wilson, J. D. and B. L. Sawford, 1996: Lagrangian stochastic models for trajectories in the turbulent atmosphere. *Bound.-Layer Meteorol.*, **78**, 191-210.

Wilson, J. D. and T. K. Flesch, 1997: Trajectory curvature as a selection criterion for valid Lagrangian stochastic models. *Boundary-Layer Meteorol.*, **84**, 411-425.

Woods, N., I. P. Craig, G, Dorr, B. Young, 2001: Spray drift of pesticides arising from aerial application in cotton. *J. Environ. Qual.*, **30**, 697 - 701.

Xu, M., K. Willeke, 1993: Impaction and rebound of particles at acute incident angles. *Aerosol Sci. Tech.*, **18**, 143-155.

Chapter 2

An approximate analytical solution for the deposition of heavy particles released from an elevated line source

Paper published in 'Boundary-Layer Meteorology', a journal of Springer.

Authors: T. Bouvet and J.D. Wilson[1]

[1]Authors are cited in the order of their respective contributions. John Wilson provided guidance, and contributed to the writing and editing of the paper.

Contents

2.1 Introduction 48

2.2 The analytical solution 49

2.2.1 The Rounds-Godson solution 49

2.2.2 Accounting for the Crossing Trajectory Effect (CTE) 52

2.3 Discussion and test of the analytical solution . . . 56

2.3.1 On the assumption of 'far field' dispersion 56

2.3.2 Neglect of turbulent deposition 58

2.3.3 Test against experimental results and Lagrangian Stochastic (LS) simulations 62

2.4 An even simpler description implicit in the analytical solution 69

2.5 Conclusion 72

2.6 References 73

2.1 Introduction

In the context of particle dispersion in the atmosphere, numerical modeling is a powerful tool of investigation. However, the price of the flexibility it offers is a loss of physical transparency. An analytical solution offers two major advantages over numerical treatment: first, it gives direct insight on the parameters controlling dispersion and the physics at play. Secondly, it is rapid and easy to use, whereas numerical simulation may be difficult. Thus, numerical and analytical treatments may be regarded as complementary.

Developing the work of Rounds (1955), Godson (1958) presented an analytical solution for the concentration field and the deposition swath of heavy particles released from an elevated line source over uniform terrain. The solution is founded on various assumptions, of which the strongest is to approximate turbulent convection as a diffusion process, and with the heavy particle diffusivity equated with the eddy viscosity that is implicit in the logarithmic wind profile. Here we further develop the Rounds-Godson solution, modifying it to account for the crossing trajectory effect (Csanady, 1963). As we will show, simple adjustments to Godson's solution significantly improve its performance, and ensure satisfactory analytical results over a wide range of particle sizes and meteorological conditions. Our criteria for performance of the analytical solution include both experimental data (Hage, 1961; Walker, 1965) and numerical simulations using a Lagrangian Stochastic (LS) model. The LS model is known (Wilson, 2000) to be fairly accurate for heavy particle dispersion over uniform terrain.

2.2 The analytical solution

2.2.1 The Rounds-Godson solution

In a steady-state regime, if one neglects streamwise turbulence and invokes gradient diffusion closure for the turbulent fluxes, then heavy particle transport and dispersion in a horizontally uniform flow can be described by the following mass conservation equation

$$\overline{u}\,\frac{\partial c}{\partial x} = \frac{\partial}{\partial z}\left(K\,\frac{\partial c}{\partial x} + w_g\,c\right) \tag{2.1}$$

where $\overline{u} = \overline{u}(z)$ is the mean horizontal velocity, $c = c(x,z)$ is the particle concentration, $K = K(z)$ is the particle diffusivity and w_g is the gravitational settling velocity of particles, namely the equilibrium velocity of a heavy particle falling in a static fluid. If the particle is spherical and small enough that Stokes' law holds, then $w_g = g\,\tau_p$, where g is the gravitational acceleration and $\tau_p = \frac{\rho d_\mathrm{p}^2}{18\,\mu}$ is the particle's acceleration time scale, ρ being the density of the particle, d_p its diameter, and μ the dynamic viscosity of the air. Here and throughout this article, equations and variables are given (with a few obvious exceptions) in non-dimensional form, the source height H_s and the friction velocity u_* being taken as length and velocity scales.

Rounds (1955) derives an approximate solution of equation (2.1) for an elevated line source releasing particles into a neutral (non-stratified) atmosphere. Godson (1958) generalizes Round's solution to the case of thermally stratified atmosphere. The forms used for the profiles of vertical diffusivity $K(z)$ and horizontal wind speed $\overline{u}(z)$ are derived from the (now obsolete, yet evidently useful) formulations suggested by Deacon (1949):

$$\overline{u} \;=\; \frac{1}{k_v\,(1-\nu)}\left[\left(\frac{z}{z_0}\right)^{1-\nu} - 1\right] \tag{2.2}$$

$$K = k_v z_0^{1-\nu} z^{\nu} \tag{2.3}$$

where k_v is the Von Karman constant and z_0 is the roughness length (defined as the height where the mean horizontal wind speed vanishes). ν is a stability parameter which relates to the Monin-Obukhov length $L_{\rm mo}$ as

$$\nu = 1 - \frac{\ln(\varphi_m(z/L_{\rm mo}))}{\ln(z/z_0)} \tag{2.4}$$

where φ_m is the Monin-Obukhov universal function for momentum; note that $\nu > 1$ for unstable conditions, $\nu = 1$ at neutral stability, and $\nu < 1$ for unstable conditions. The wind velocity profile (equation (2.2)) satisfies $\overline{u}(z_0) = 0$ m s^{-1} and tends to the logarithmic form $\overline{u} = (1/k_v)\ln(z/z_0)$, under neutral conditions, when $\nu \to 1$. No closed form solution to the heavy particle advection-diffusion equation (2.1) can be achieved with the wind and diffusivity parameterizations (2.2)-(2.3), as such. However, the problem can be solved if the profiles (2.2)-(2.3) are approximated in the following manner:

$$\overline{u} = q\left(\frac{z}{z_0}\right)^{\alpha} \tag{2.5}$$

$$K = \xi k_v z \tag{2.6}$$

where

$$\xi = \frac{2}{1+\nu} z_0^{1-\nu} \tag{2.7}$$

$$q = \frac{1}{k_v \alpha}(2z_0)^{\alpha+\nu-1} \tag{2.8}$$

$$\tag{2.9}$$

$$1 + \alpha = \gamma = \begin{cases} \frac{1 - z_0^{1-\nu}}{\frac{1}{2-\nu} - z_0^{1-\nu}} & \nu \neq 1 \\ \frac{ln(z_0)}{1+ln(z_0)} & \nu = 1 \end{cases} \tag{2.10}$$

The parameters ξ, α, and q are determined by requiring that (in a short-hand notation)

$$\int_0^1 (2.2)dz = \int_0^1 (2.5)dz \tag{2.11}$$

$$\left.\frac{d(2.2)}{dz}\right|_{z=1/2} = \left.\frac{d(2.5)}{dz}\right|_{z=1/2} \tag{2.12}$$

$$\int_0^1 (2.3)dz = \int_0^1 (2.6)dz \tag{2.13}$$

Note that z is dimensionless, so that $z = 1$ is the source height. The bottom boundary of the domain ('the ground') is placed at $z = 0$; it is assumed perfectly absorbing, and the diffusive flux to ground is neglected. Thus the lower boundary condition is specified by the deposition flux:

$$D(x) = w_g\, c(x, z = 0) \tag{2.14}$$

or equivalently

$$\left[K\left(\frac{\partial c}{\partial z}\right)\right]_{z=0} = 0 \tag{2.15}$$

Based on the boundary condition (2.14)-(2.15) and on the profiles (2.5)-(2.6), a solution to equation (2.1) is achieved. By application of equation (2.14), the flux of particles to ground normalized by the rate of emission Q is:

$$\frac{D(x)}{Q} = \frac{1}{A\,\Gamma(p)} \exp\left(-\frac{A}{x}\right)\left(\frac{A}{x}\right)^{1+p} \tag{2.16}$$

where

$$p = \frac{w_g}{\xi\, k_v\, \gamma} \tag{2.17}$$

$$A = \frac{\overline{u}(H_s)}{\xi\, k_v\, \gamma^2} \tag{2.18}$$

and where $\Gamma(p)$ is the Gamma function of parameter p: $\Gamma(p) = \int_0^\infty t^{p-1}e^{-t}dt$. According to this solution, the deposition swath has the distribution of a Gamma function relative to the variable A/x, and with shape parameter $(p+2)$.

However the solution of Godson actually omits an important feature of heavy particle dispersion, the 'Crossing Trajectory Effect' (henceforth called

CTE) first identified by Csanady (1963). In the following paragraphs, after briefly recalling the physics underlying the CTE, a simple adjustment to the analytical solution which allows to account for the CTE will be presented.

2.2.2 Accounting for the Crossing Trajectory Effect (CTE)

By definition, velocity statistics of passive tracer particles are strictly identical to the velocity statistics of particles of the carrying fluid. However heavy particles respond to gravity and to some extent fall out through the fluid, so as a result, the sample of fluid velocities 'seen' by heavy particles is not the same as the one seen by passive tracer particles. In other words, the velocity statistics of the driving fluid surrounding a particle differ, depending on whether this particle is passive or otherwise. In particular, the correlation time scale, which is a measure of the fluid velocity persistence along a particle trajectory, is altered. In the case of passive tracer particles, velocity de-correlation stems only from eddy decay in time. Because heavy particles 'fall out' through eddies, the fluid velocity along their trajectories is additionally space-decorrelated. In consequence the velocity auto-correlation function for heavy particles $R_{HP}(\zeta)$, defined as $R^{i,j}_{HP} = \overline{v_i(t)v_j(t+\zeta)}/(\sigma_{v_i}\sigma_{v_j})$, is expected to be smaller than its passive tracer particle counterpart $R_L(\zeta)$ when ζ (the time of separation) is much larger than the particle inertial time scale τ_p (when $\zeta \ll \tau_p$, then $R_{HP}(\zeta) \approx 1$ and $R_{HP}(\zeta) \geq R_L(\zeta)$; this is a consequence of inertia). The time scale for dispersion of heavy particles (henceforth called $T_{HP} = \int_0^\infty R_{HP}(\zeta)d\zeta$) is accordingly reduced relative to the integral time scale $T_L = \int_0^\infty R_L(\zeta)d\zeta$. Figure (2.1) illustrates how critical the CTE can be in the dispersion of heavy particles; it presents experimental data for deposition along with the corresponding analytical solution in two situations: when the CTE is

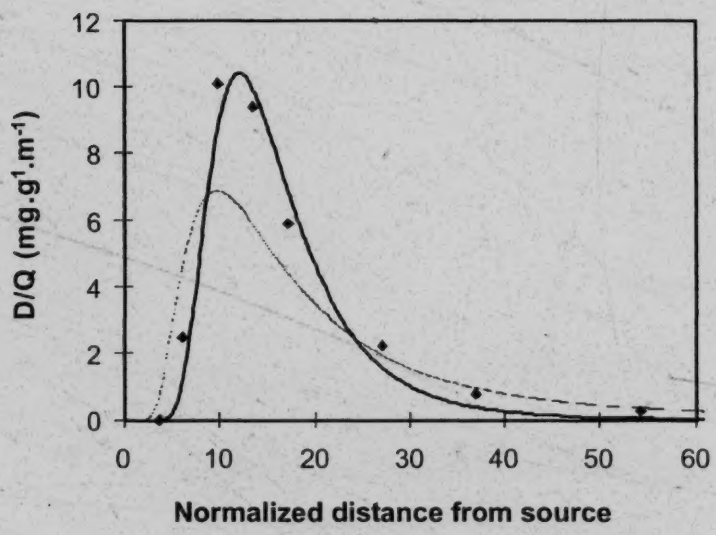

Figure 2.1: Normalized deposition rate of heavy particles (settling velocity $w_g = 0.19$ m s^{-1}), released 7.4 m above ground, in a stable atmosphere ($u_\star = 0.18$ m s^{-1}, $z_0 = 0.016$ m, $L_{\rm mo} = 16$ m). Comparison between experimental data of Hage (1961), shown by dots, and analytical solutions in two cases: the solution of Godson, when the CTE is not included (dashed line), and the revised analytical solution, when the CTE correction is included (solid line).

accounted for (by the method described below), and when it is not (Godson's solution). Clearly, in this example, the CTE is significant, and accounting for it offers a major improvement in the analytical solution. We therefore propose below a simple adjustment to the eddy diffusivity, allowing to take the CTE into consideration in the analytical solution.

To reconcile the eddy diffusion treatment with Taylor's (1921) Lagrangian treatment, one must require that the eddy diffusivity of tracer particles K_L satisfies[2]

$$K_L = \sigma_w^2 \int_0^\infty R_L(\zeta) d\zeta \tag{2.19}$$

In the far field limit, when the travel time is much larger than T_L, the particle diffusivity is linearly related to T_L:

$$K_{L,\infty} = \sigma_w^2 T_L \tag{2.20}$$

This result applies for the motion of passive tracer particles in the far field of a source and in homogeneous turbulence. We will consider it as a pattern for the heuristic modification of heavy particle diffusivity (K_{HP}) in inhomogeneous turbulence, by writing

$$K_{HP,\infty} = \sigma_w^2 T_{HP} \tag{2.21}$$

Sawford and Guest (1991), following Csanady (1963), suggest that T_{HP} be parameterized in a heuristic fashion as

$$T_{HP} = \frac{T_L}{\sqrt{1 + \left(\beta \frac{w_g}{\sigma_w}\right)^2}} \tag{2.22}$$

where σ_w is the fluid vertical velocity variance and $\beta = \sigma_w T_L / L_E$ is an empirical parameter relating Eulerian and Lagrangian scales. By combining equa-

[2]In the interests of clarity, in the remainder of this section (only) we attach the subscript HP (or L) to the diffusivity for heavy particles (or tracer particles).

tions (2.21) and (2.22), the heavy particle diffusivity in the far field is

$$K_{HP,\infty} = K_{L,\infty}\left[1 + \left(\beta\frac{w_g}{\sigma_w}\right)^2\right]^{-1/2} \tag{2.23}$$

We justify this adjustment for $K_{HP,\infty}$ by the evidence (see Figure (2.1)) that it improves the agreement of the analytical solution with observations, and remind the reader that dispersion of particles in the near-field is outside the scope of this article (discussion on this point follows in paragraph 2.3.1). Therefore, we drop the far field subscript (∞), on the understanding that the analytical solution is to be applied in the far field of the source. As Godson showed, Eq. (2.16) applies for any generalization of the eddy diffusivity, provided it can be written in the form (2.6); in particular, ξ should not be a function of height. This requirement can be accommodated by writing

$$\frac{K_{HP}}{K_L}(z) \approx \frac{K_{HP}}{K_L}(H_s) = \left[1 + \left(\beta\frac{w_g}{\sigma_w(H_s)}\right)^2\right]^{-1/2} \tag{2.24}$$

Then the parameter ξ becomes

$$\xi = \varphi(\nu, z_0)\,\psi\left(\frac{\beta\, w_g}{\sigma_w(H_s)}\right) \tag{2.25}$$

where $\varphi(\nu, z_0)$ is the adjustment made by Godson (Eq. 2.7) to generalize the diffusivity to stratified atmospheres, and $\psi\left(\frac{\beta\, w_g}{\sigma_w(H_s)}\right)$ is the additional correction for heavy particle diffusivity, presented in Eq. 2.24. With this new formulation for ξ, the analytical solution (2.16) accounts approximately for both thermal stratification and for the crossing-trajectory effect. Eq. (2.25) implicitly assumes the Schmidt number $S_c = 1$, i.e. the eddy diffusivity for tracer material is assumed identical to the eddy diffusivity for momentum.

2.3 Discussion and test of the analytical solution

2.3.1 On the assumption of 'far field' dispersion

The formulation that is proposed for the eddy-diffusivity K (Eq. 2.6), and in turn the solution Eq. 2.16 as a whole, stands on the assumption that particles reach the 'far field' of the source, i.e. that particle travel time is much larger than the velocity autocorrelation time scale (T_{HP}). Indeed, only by invoking a dependency of the eddy-diffusivity on time (or distance) from the source can the advection-diffusion equation be forced to describe the near-field (eg. Deardorff, 1978). The 'far field' assumption is however reasonable. Figure (2.2) shows the computed mean number (N) of time intervals $T_{HP}(t)$ that elapse during a particle's trajectory from the source to its point of deposition. Note that turbulence is not homogeneous in the boundary layer, and that T_{HP} decreases as the particle approaches the ground. Therefore, T_{HP} is not constant along a particle's trajectory. Were turbulence homogeneous (and therefore T_{HP} constant), N would simply equal the ratio t/T_{HP} of the travel time of a particle to the velocity autocorrelation timescale. The mean N may be loosely interpreted as the number of independent velocity 'choices' made by a particle along its flight, and one may consider the far field to have been reached when $N \gg 1$. We see on Figure (2.2) that in standard meteorological conditions ($0.1 \leq u_* \leq 0.6$ m s^{-1}), $N \geq 7$ for particles ($w_g \leq 1.3$ m s^{-1}) released from a source elevated at $H_s = 0.1$ m. N is larger when the source is higher (not shown), thus the assumption that particles reach the far field is reasonable. It may lead to slight quantitative errors, in particular for large particles, but the analytical solution ought to capture at least the right qualitative behavior.

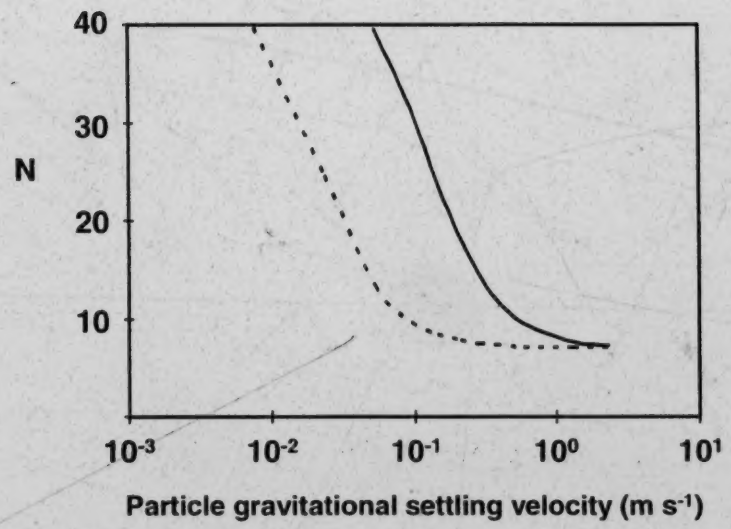

Figure 2.2: Estimation of the number N of independent velocity choices made by a particle along its trajectory to its point of deposition, as a function of particle gravitational settling velocity (w_g). N has been computed with the LS model as the average number of elapsed intervals T_{HP} during the trajectory to deposition. The simulation is performed in a neutrally stratified atmosphere, with source height $H_s = 0.1$ m, $z_0 = 0.01$ m and $u_\star = 0.1$ m s^{-1} (dashed line) or $u_\star = 0.6$ m s^{-1} (solid line).

2.3.2 Neglect of turbulent deposition

Gravitational settling is the simplest and most obvious mechanism for deposition. However the overall deposition rate is not unaffected by the fluid velocity fluctuations, and we will call the resulting contribution to deposition the 'turbulent deposition'. Brookes and Hanratty (1994) conceptualize the turbulent deposition in terms of three mechanisms: free-flight, turbophoresis, and turbulent diffusion. The total turbulent deposition flux is the sum of these three components, the importance of each one of which varies with the distance to ground.

The solution of Rounds-Godson (2.16) is built on the assumption that gravitational settling is the *only* mechanism of deposition, as seen in Eqs. 2.14-2.15. To account for turbulent deposition, the lower boundary condition could appropriately be written

$$D(x, z_b) = V_{dep}\, c(x, z_b) \tag{2.26}$$

where z_b ($\geq z_0$) denotes the top of a shallow constant flux layer. As Slinn (1982) suggests, the deposition velocity V_{dep} is the superimposition of the gravitational settling velocity (w_g) and a component (V_{turb}) ascribable to turbulent deposition:

$$V_{dep} = w_g + V_{turb} \tag{2.27}$$

McCoy and Hanratty (1975) summarized the experimental results for turbulent deposition velocity collected by Friedlander and Johnstone (1957), Schwediman and Postma (1961), Wells and Chamberlin (1967), Farmer (1969), Schmel (1971), Forney and Spielman (1974) and Liu and Agarwal (1974). From this

extensive data base, McCoy and Hanratty proposed the parameterization

$$V_{turb} = \begin{cases} 3.25 \times 10^{-4}\,\tau_p^2 & 0.2 < \tau_p < 22.9 \\ 0.17 & \tau_p \geq 22.9 \end{cases} \qquad (2.28)$$

where V_{turb} and τ_p are non-dimensionalized with friction velocity and kinematic viscosity as scales, respectively. The case $\tau_p \leq 0.2$ is not relevant to this work, for the corresponding particles are submicronic and behave virtually like passive fluid particles.

Figure (2.3) presents the ratio $V_{turb}/(V_{turb}+w_g)$ as a function of w_g, where $w_g = g\,\tau_p$ and V_{turb} is calculated according to Eq. 2.28; evidently turbulent deposition can represent a significant component of total deposition. It was necessary therefore to assess the error induced by *not* accounting for turbulent deposition in the analytical solution of Rounds-Godson (i.e. Eq. 2.16, which assumes Eqs. 2.14-2.15 at the lower boundary). This we did by comparing the analytical solution against finite difference numerical solutions of Eq. 2.1 supplemented by the improved lower boundary condition (Eqs. 2.26-2.28). Details are given in appendix A-1. The results are shown on Figure (2.4), in the situation of neutrally stratified atmosphere, and where $u_\star = 0.35\ \mathrm{m\,s^{-1}}$, $H_s = 1$ m, $z_0 = 0.01$ m. The small discrepancy between the numerical and the analytical solution where they *both* assume the same (simpler) lower boundary condition (Eqs. 2.14-2.15) shows that discretization errors in the numerical resolution are negligible. The numerical solution built with the lower boundary condition (Eq. 2.26) is clearly distinguishable from the analytical solution; in particular, the peak deposition rate is noticeably stronger (i.e. ignoring turbulent deposition causes a reduced deposition peak). The most significant discrepancy between the Rounds-Godson solution and the numerical solution being the magnitude of the deposition peak, we present on Figure (2.5) the fractional

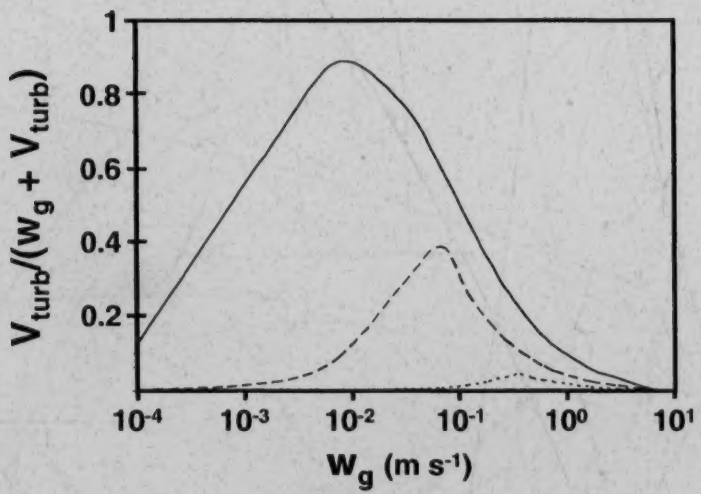

Figure 2.3: Fractional contribution of turbulent deposition ($V_{turb}c$) to total deposition ($(V_{turb} + w_g)c$), as a function of particle gravitational settling velocity ($w_g = \tau_p g$), when $u_* = 0.6$ m s^{-1} (solid line), $u_* = 0.3$ m s^{-1} (dashed line) and $u_* = 0.1$ m s^{-1} (dotted line). V_{turb} is calculated according to Eq. 2.28.

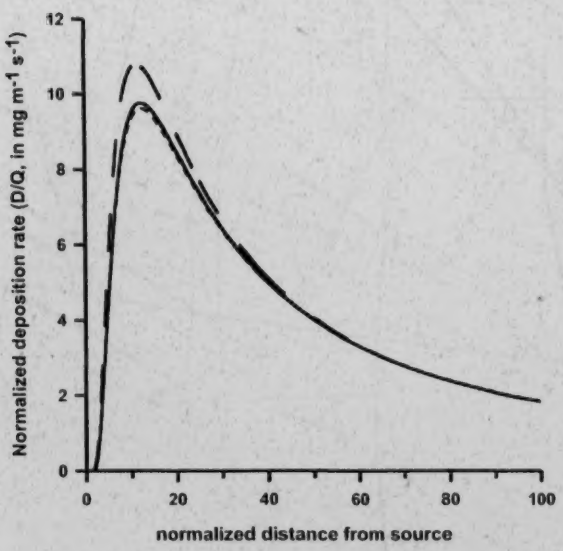

Figure 2.4: Deposition swath of heavy particles ($w_g = 6.6\ \mathrm{cm\,s^{-1}}$) released at $H_s = 1$ m in a neutrally stratified atmosphere, where $u_* = 0.35\ \mathrm{m\,s^{-1}}$ and $z_0 = 0.01$ m. The solid curve and the short-dashed curve represent respectively the analytical solution and the numerical solution of the advection-diffusion Eq. 2.1 when turbulent deposition is ignored (lower boundary condition Eqs. 2.14-2.15). The long-dashed curve shows the numerical solution when turbulent deposition is included (lower boundary condition, Eq. 2.26).

error E in this quantity (relative to the numerical solution taken as truth) as a function of $u_\star$, τ_p. It can be seen that $|E| \geq 20\%$ when $u_\star \geq 0.3\,\mathrm{m\,s^{-1}}$ and $w_g \leq 8 \times 10^{-2}\,\mathrm{m\,s^{-1}}$. In this domain of the $w_g - u_\star$ space, we consider that the analytical solution is not reliable.

2.3.3 Test against experimental results and Lagrangian Stochastic (LS) simulations

Testing the analytical solution by comparing the deposition swath with its experimental or numerical counterpart can become confusing, especially when the number of comparisons is large. We therefore focus on four variables which characterize the deposition swath: the position (x_{peak}) and magnitude $(D/Q)_{peak}$ of the deposition peak, the standard deviation (σ_x) of the deposition location, and the distance from the source over which 90% of the particles will have been deposited ($x_{90\%}$). The analytical solution (Eq. 2.16) implies that

$$x_{peak} = \frac{A}{1+p} \tag{2.29}$$

$$\left(\frac{D}{Q}\right)_{peak} = \frac{[(1+p)/e]^{1+p}}{A\,\Gamma(p)} \tag{2.30}$$

$$\sigma_x = \frac{A}{p-1}\sqrt{\frac{1}{p-2}} \tag{2.31}$$

where σ_x is defined analytically only for $p \in [2;\infty]$. Finally, the recovered fraction is related to the distance from source by:

$$\mathrm{Rec}(x) = 1 - \frac{\Gamma_{A/x}(p)}{\Gamma(p)} \tag{2.32}$$

where $\Gamma_{a/x}(p)$ is the incomplete Gamma function of parameter p, defined as

$$\Gamma_{A/x}(p) = \int_0^{A/x} e^{-t} t^{p-1} dt \tag{2.33}$$

The relationship $\mathrm{Rec}(x)$ can be inverted numerically in order to obtain the recovery distance as a function of the corresponding recovered fraction.

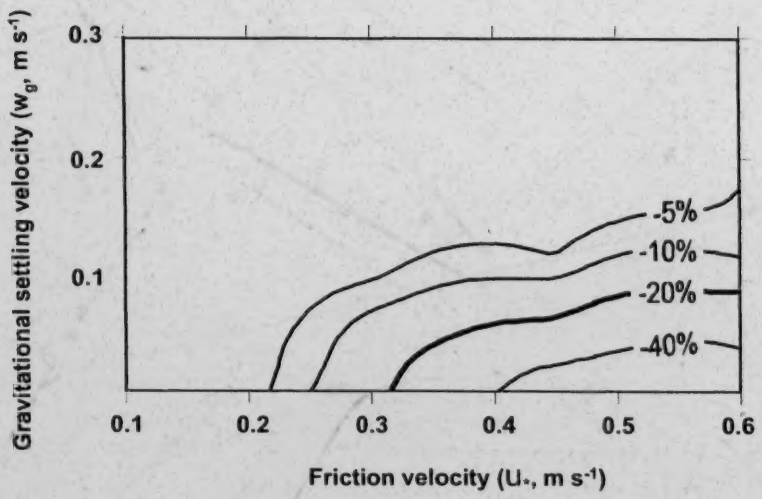

Figure 2.5: Fractional Error in the approximate analytical solution, relative to a numerical solution of the advection-diffusion equation (Eq. 2.1) with the more realistic lower boundary condition (Eqs. 2.26-2.28). The other boundary conditions and the parameterizations for $\overline{u}$ and K are the same as assumed in the analytical treatment, and the atmosphere is taken as neutrally stratified. We found that the height of the source does not affect the distribution of the error in the $w_g - u_*$ space.

We first test the refined analytical solution against the experimental data collected by Hage (1961) and Walker (1965) over a fairly broad range of micrometeorological conditions ($u_\star \in [0.18, 0.57]$ m s^{-1}; $H_s/L_{mo} \in [-0.37, 0.50]$; $z_0/H_s \in [5.4 \times 10^{-4}, 5.8 \times 10^{-3}]$; $w_g/u_\star \in [0.25; 1.66]$). Figures 2.6-2.7 compare the analytical solutions for the position and the magnitude of the peak of the deposition swath, with their experimental counterparts. There is some uncertainty in the experimental values, for only 'samples' (discontinuous values) of the deposition swath are available. Thus, values for the peak location are interpolated; likewise, the values used for the magnitude of the peak are at best equal to the real values, and otherwise underestimations. In spite of the uncertainty inherent to the experimental data, one observes a very good match between the theoretical and experimental values. This shows the satisfactory performance of the analytical solution, at least in the range of particle sizes used. Note that reducing the Schmidt number to $S_c = 0.63$ as other authors have suggested (eg. Wilson, 2000) does not improve the agreement with the experimental data of Hage (1961) and Walker (1965).

In order to test the analytical solution over a wider spectrum of conditions, we compare analytical results for the four swath statistics (x_{peak}, $(D/Q)_{peak}$, σ_x, $x_{90\%}$) with corresponding predictions of a first-order Lagrangian stochastic model (for details of the model, please see appendix A-2). These comparisons are performed over an extensive range of particle sizes and meteorological conditions ($u_\star \in [0.1, 0.5]$ m s^{-1}, $H_s/L_{mo} \in -0.4; 0.4$, $w_g/u_\star \in [0.02, 52.68]$, and the results are presented in Figures (2.8a-d). Each statistic (x_{peak}, $(D/Q)_{peak}$, σ_x or $x_{90\%}$) is plotted as a function of $\overline{u}(H_s)/w_g$, resulting in a remarkably simple organization of the data, in both of the two (quite extreme) test situations of thermal stratification ($H_s/L_{mo} = 0.4$ or

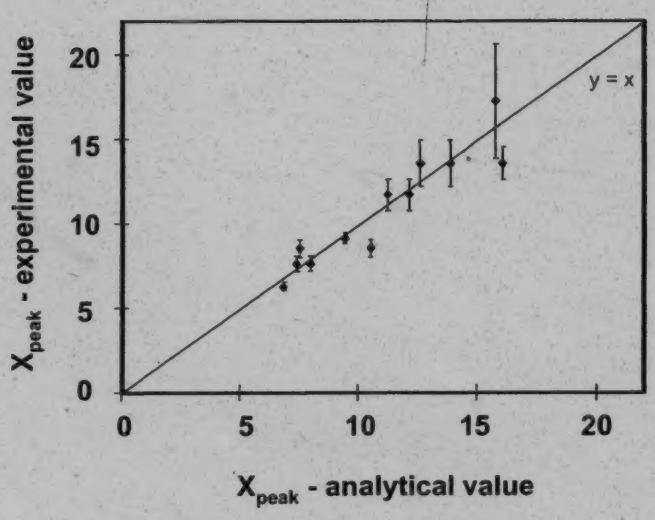

Figure 2.6: Comparison between the experimental value and the analytical solution for the position of the peak along the deposition swath. The error bars represent the uncertainty in the experimental values. Conditions: $u_\star \in [0.18\,,\,0.57]\ \mathrm{m\,s^{-1}}$; $H_s/L_{mo} \in [-0.37\,,\,0.50]$; $z_0/H_s \in [5.4 \times 10^{-4}\,,\,5.8 \times 10^{-3}]$; $w_g/u_\star \in [0.25,\ 1.66]$.

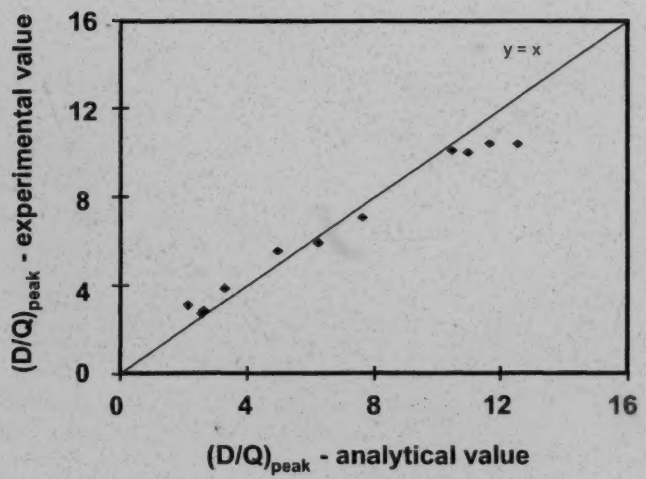

Figure 2.7: Comparison between the experimental value and the analytical solution for the normalized peak deposition rate. Conditions: $u_\star \in [0.18, 0.57]$ m s^{-1}; $H_s/L_{mo} \in [-0.37, 0.50]$; $z_0/H_s \in [5.4 \times 10^{-4}, 5.8 \times 10^{-3}]$; $w_g/u_\star \in [0.25, 1.66]$.
NB: Because experimental data are discontinuous along the deposition swath, the peak experimental value is likely to be an under-evaluation of the actual peak value.

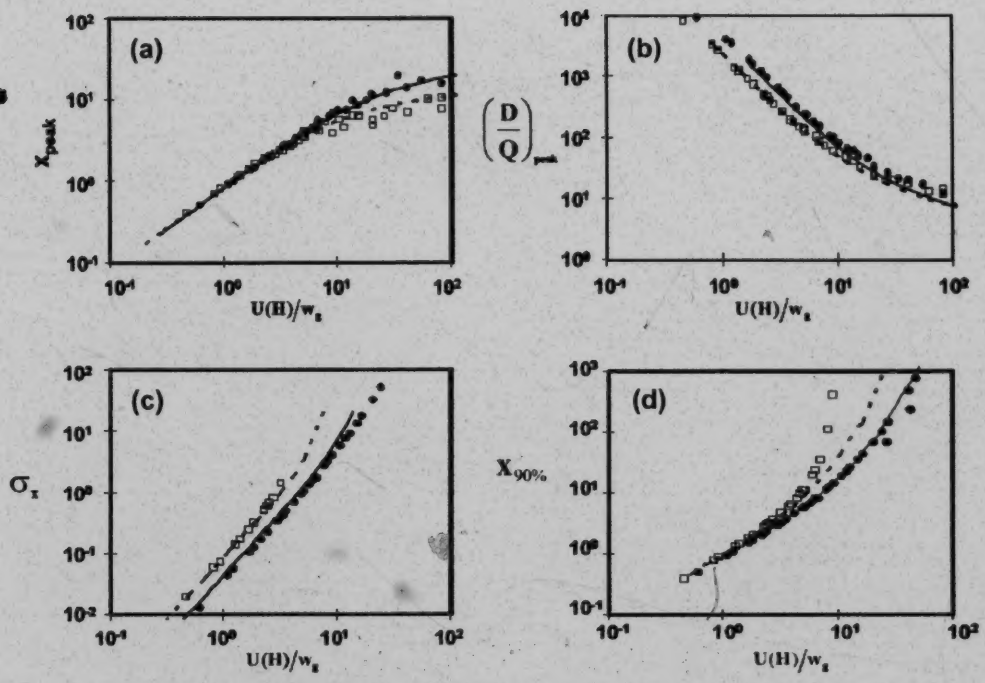

Figure 2.8: Comparison between the analytical solution and the corresponding LS solution for (a) the location of the deposition peak (x_{peak}); (b) the magnitude of the normalized deposition peak ($[D/Q]_{\text{peak}}$); (c) the standard deviation of the deposition location (σ_x); (d) the '90% recovery distance' ($x_{90\%}$).

The solid line and the dots present respectively the analytical and the LS model solutions in the stable case ($H_s/L_{mo} = 0.4$). The dashed line and the squares present respectively the analytical and the LS model solutions in the unstable case ($H_s/L_{mo} = -0.4$).

Conditions: $u_\star \in [0.1\,,\,0.5]$ m s^{-1}; $w_g/u_\star \in [0.02\,,\,52.68]$; $z_0/H_s = 5 \times 10^{-3}$; $\beta = 1$.

$H_s/L_{mo} = -0.4$). As far as x_{peak} is concerned (Figure 2.8a), a discrepancy between the analytical and the LS model solutions becomes noticeable in the stable case for $\overline{u}(H_s)/w_g > 10$. For $(D/Q)_{peak}$ (Figure 2.8b), a growing discrepancy arises beyond $\overline{u}(H_s)/w_g \approx 30$, in both cases of stratification. The graphic presenting $\sigma_x(\overline{u}(H_s)/w_g)$ - Figure (2.8c) - is fairly incomplete, for $(\sigma_x)_{analytical}$ has a restricted domain of definition, as is clear by inspection of Eq. 2.31, and furthermore $(\sigma_x)_{LS}$ could not be computed with the LS model for large $\overline{u}(H_s)/w_g$; in effect, under such conditions, a fraction of the particles released would deposit at a virtually infinite distance from the source. Since these particles do not deposit in the computational domain, the probability density function of the deposition location is incomplete, explaining why $(\sigma_x)_{LS}$ could not be computed. However, in the restricted domain where σ_x is defined and computed, the match between the analytical and LS model results is very satisfactory in both cases of stratification. Finally, Figure (2.8d) shows how the analytical solution compares with LS results in terms of the recovery distance $x_{90\%}$. In a stable atmosphere the match is almost perfect, even for very large values of $\overline{u}(H_s)/w_g$. But in an unstable atmosphere, the analytical and LS model solutions diverge at $\overline{u}(H_s)/w_g > 7$. In summary, the match between the analytical solution and the more sophisticated LS model is excellent for the four criteria tested, as long as the variable $\overline{u}(H_s)/w_g$ remains below 7. For larger values, the analytical solution gives a correct qualitative trend, but fails quantitatively in some conditions over one or more criteria.

2.4 An even simpler description implicit in the analytical solution

The value of β is regarded as a constant in the following discussion, and set to unity, following Raupach (2002). In addition since the analytical solution has been shown to be reliable only provided $\overline{u}(H_s)/w_g < 7$, the following discussion is restricted to this domain of validity.

According to the analytical formula for the deposition swath (Eq. 2.16), A and p are the driving variables. However, their interpretation is not simple. A dissection of parameters A and p allows to retrieve the more fundamental variables w_g, $u_\star$, ν (the stability parameter) and z_0. The variable $\overline{u}(H_s)/w_g$ in some sense integrates the influences of those 'fundamental parameters'. In addition, it allows a remarkable collapse of data for the four deposition swath characteristics. In other words, $\overline{u}(H_s)/w_g$ properly accounts for most of the variability when all z_0, ν, $u_\star$ and w_g are variable. As an illustration, Figure (2.9) presents the relationship between x_{peak} and $\overline{u}(H_s)/w_g$ when the friction velocity, thermal stability, gravitational settling velocity, and roughness length are all variable ($u_\star \in [0.1, 0.5]\, m\, s^{-1}$, $H_s/L_{mo} \in \{-0.4; 0.4\}$, $w_g/u_\star \in [0.02, 52.68]$, $z_0/H_s \in [2 \times 10^{-4}; 5 \times 10^{-2}]$). The residual variability (i.e., the variability not 'explained' by $\overline{u}(H_s)/w_g$) is seen in the width of the envelope that encompasses the cloud of dots. It is essentially due to the variability in z_0 when $\overline{u}(H_s)/w_g < 7$, and it remains small.

From a regression analysis, we derived the following relationships between the four statistics and $\overline{u}(H_s)/w_g$ (in all cases, the fraction of variance explained, R^2, is larger than 0.990):

$$x_{peak} \propto [\overline{u}(H_s)/w_g]^{0.9} \tag{2.34}$$

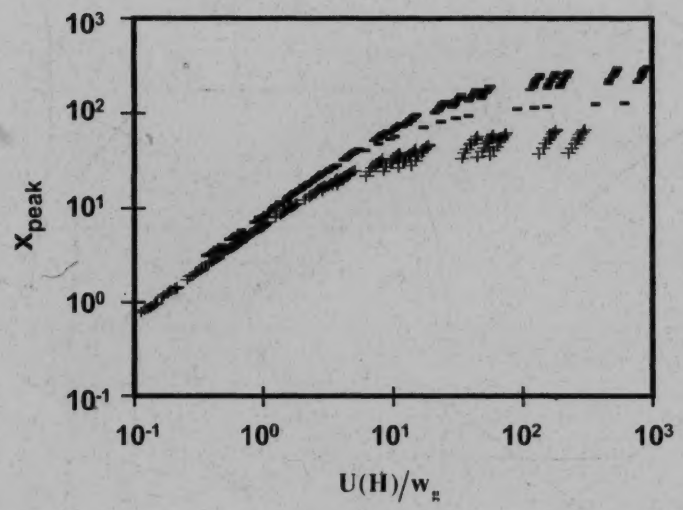

Figure 2.9: Analytical solution of the location of the deposition peak (x_{peak}) over a wide range of conditions: $u_\star \in [0.1\,,\,0.5]\ \mathrm{m\,s^{-1}}$; $w_g/u_\star \in [0.02\,,\,52.68]$; $H_s/L_{mo} \in [-0.4\,,\,0.4]$; $z_0/H_s = [2 \times 10^{-4}\,;\,5 \times 10^{-2}]$; $\beta = 1.0$.
The 'dash' symbols (-) represent the situation $z_0/H_s = 2 \times 10^{-4}$, whereas the 'plus' symbols (+) represent the situation $z_0/H_s = 5 \times 10^{-2}$.

$$\left(\frac{D}{Q}\right)_{peak} \propto [\overline{u}(H_s)/w_g]^{-11/6} \quad (2.35)$$

$$x_{90\%} \propto [\overline{u}(H_s)/w_g]^{5/4} \quad (2.36)$$

$$\sigma_x \propto [\overline{u}(H_s)/w_g]^2 \quad (2.37)$$

Interestingly x_{peak} is very well approximated by the ballistic impact point, defined as (here in dimensional form)

$$x_{bal} = \int_0^{H_s/w_g} \overline{u}(H_s - w_g t)\, dt \quad (2.38)$$

i.e. x_{bal} is the hypothetical location where a particle would deposit if it did not experience turbulence along its trajectory.

Eqs. 2.34-2.37 show that for growing $\overline{u}(H_s)/w_g$, the characteristic length scales of the deposition swath (i.e. x_{peak}, σ_x and $x_{90\%}$) increase, whereas $(D/Q)_{peak}$ drops. Large $\overline{u}(H_s)/w_g$ means that mean horizontal convection is stronger than mean vertical transport, thus a greatly extended deposition swath is no surprise. Large $\overline{u}(H_s)/w_g$ also correlates with long time of flight before deposition, and therefore long action time for turbulence to disperse particles. This is consistent with the corresponding large spread (large σ_x and small $(D/Q)_{peak}$).

2.5 Conclusion

A simple adjustment to the Rounds-Godson solution for heavy particle deposition to account for the Crossing Trajectories Effect has significantly improved that solution, and could be easily transposed to the solution for the concentration field given by Rounds (1955). Tests and analysis of such a corrected solution will be addressed in a future work.

The refined analytical solution for deposition that we propose proves very skillful when $\overline{u}(H_s)/w_g < 7$. The distance of recovery, the location and intensity of the peak are all valuable information in the context of pollution management, and can all be calculated analytically. Consequently this solution may be of practical interest, for it is very easily accessible. It is also shown that the simple variable $\overline{u}(H_s)/w_g$ exerts a key control on the deposition swath as a whole, and suffices to give a good estimate of it. However, the analytical solution is not suitable to handle dispersion over disturbed terrain, or from a complex source distribution; in such cases numerical modeling becomes necessary.

2.6 References

Barad, M.L.: 1958, 'Project Prairie Grass, a field program in diffusion', *Geophysical Research Papers* **59** I-III.

Brooke, J. W. and Hanratty, T. J.: 1994, 'Free-flight mixing and deposition of aerosols', *Phys. Fluids* **6** (10), 3404-3415.

Csanady, G. T.: 1963, 'Turbulent diffusion of heavy particles in the atmosphere', *J. Atmos. Sci.* **20**, 201-208.

Deacon, E. L.: 1949, 'Vertical diffusion in the lowest layers of the atmosphere', *Quart. J. R. Meteorol. Soc.* **75**, 89-103.

Deardorff, J. W.: 1978, 'Closure of second- and third-moment rate equations for diffusion in homogeneous turbulence', *Phys. Fluids* **21**, 525-530.

Farmer, R. A.: 1969, *'Liquid droplets trajectories in two-phase flow'*, PhD thesis, Massachussets Institute of Technology.

Forney, L. J. and Spielman, L. A.: 1974, 'Deposition of coarse aerosols from turbulent flow', *J. Aerosol Sci.* **5**, 257-271.

Friedlander, S. K. and Johnstone, H. F.: 1957, 'Deposition of suspended particles from turbulent gas streams', *Ind. Eng. Chem.* **49**, 1151-1156.

Godson, W. L.: 1958, 'The Diffusion of Particulate Matter from an Elevated Source', *Archiv. F. Met. Geophys. und Biokl. A* **10**, 305-327.

Hage, K. D.: 1961, 'On the dispersion of large particles from a 15-m source in the atmosphere', *J. Meteorol.* **18**, 534-539.

Liu, Y. H. and Agarwal, J. K.: 1974, 'Experimental observation of aerosol deposition in turbulent flow', *J. Aerosol Sci.* **5**, 145-155.

McCoy, D. D. and Hanratty, T. J.: 1977, 'Rate of deposition of droplets in annular two-phase flow', *Int. J. Multiphase Flow* **3**, 319-331.

Patankar, S.V.: 1980, 'Numerical Heat Transfer and Fluid Flow', Hemisphere Publ.

Raupach, M. R.: 2002, 'Diffusion of heavy particles in a turbulent flow', *Geophys. Monograph., Environmental Mechanics: Water, Mass and Energy Tranfer in the Biosphere* **129**, American Geophysical Union, Washington, 301-316.

Rounds, W.: 1955, 'Solutions of the two-dimensional diffusion equations', *Trans. Amer. Geophys. Union* **36**, 395-405.

Sawford, B. L.: 1991, 'Lagrangian stochastic simulations of the turbulent motion of heavy particles', *Boundary-Layer Meteorol.* **54**, 147-166.

Slinn, W. G. N.: 1982, 'Predictions for particle deposition to vegetative canopies',

Atmos. Environ. **16**, 1785-1794.

Sehmel. G. A.: 1971. 'Particle diffusivities and deposition velocities over a horizontal smooth surface', *J. Colloid. Interface Sci.* **37**, 891-906.

Schwediman, L. C. and Postma, A. K.: 1961, 'Turbulent deposition in sampling lines', USAEC Report No. HW-65309.

Taylor, G. I.: 1921, 'Diffusion by continuous movements', *Proc. London Math. Soc. Ser. 2* **20**, 196-212.

Walker, E. R.: 1965, 'A particulate diffusion experiment', *J. Appl. Meteorol.* **4**, 614-621.

Wells, A. C. and Chamberlin, A. C.: 1967, 'Transport of small particles to vertical surfaces', *Br. J. Appl. Phys.* **18**, 1793-1799.

Wilson, J. D.: 2000, 'Trajectory models for heavy particles in atmospheric turbulence: comparison with observations', *J. Appl. Meteorol.* **39**, 1894-1912.

Chapter 3

Observations and modelling of heavy particle deposition in a windbreak flow

Paper accepted in 'Journal of Applied Meteorology', a publication of the American Meteorological Society.

Authors: T. Bouvet, J.D. Wilson and A. Tuzet[1]

[1]Authors are listed in the order of their respective contributions. The last two authors have made contributions in the writing and editing of the paper, and in financially supporting the experiment.

Contents

3.1 Introduction 78

3.2 The experiment 79

3.2.1 Material 81

3.2.2 Micro-meteorological measurements 85

3.2.3 Deposition measurements 85

3.3 The particle transport model 86

3.3.1 Generalized Langevin equation 87

3.3.2 Adjustments to the Langevin equation for heavy particle dispersion 89

The Crossing Trajectory Effect (CTE) 89

The Continuity Effect 90

3.3.3 Reproducing the experimental conditions 91

Treatment of vertical and cross-wind dispersion . . . 92

Particle entrapment by the fence 101

On the values used for χ 103

3.4 Results 105

3.4.1 Micrometeorological data 105

3.4.2 Deposition 105

3.4.3 Discussion and Conclusions 109

3.5 References 119

3.1 Introduction

Controlling the advection of heavy particles is an issue of concern from an environmental and an agricultural perspective. For instance, wind erosion of soil is a major cause of fertility loss in arid regions (Li et al., 2004), and the drift of agricultural chemicals like pesticides (Woods et al., 2001) and fertilizers causes pollution and economic losses for farmers. Over the past few years, promotion of GM (Genetically Modified) crops has raised the problem of controlling the advective fluxes of GM genes, for it is necessary to confine pollen grains inside their original crop in order to prevent them from invading the genomes of other plants (Klein et al., 2003). These examples illustrate the importance of finding efficient strategies to mitigate heavy particle drift in the atmosphere.

The complexity of the physics underlying the transportation of particles in disturbed turbulent flows requires the use of numerical modeling as a tool of investigation. Reynolds (2000) showed the good skills of his Lagrangian Stochastic (LS) model for simulating the dispersion of heavy particles in a turbulent (inhomogeneous) pipe flow. Wilson (2000) analyzed the capabilities of simple LS models for the dispersion of heavy particles in the atmosphere over level terrain, with reference to measurements of particle deposition by Hage (1961) and Walker (1965). However, experimental data pertaining to the dispersion of heavy particles in a *disturbed* atmospheric flow are limited and the skills of LS models in this situation have been documented by only a few studies (Jarosz et al., 2003, 2004 for instance). The objective of this paper is to present new observations of heavy particle deposition, both in undisturbed winds, and in the disturbed winds about a porous fence. These data will then

be used to investigate the accuracy of a first-order, single particle Lagrangian Stochastic trajectory model that is based on existing parameterizations and an estimated field of wind statistics furnished by solving the momentum equations with a Reynolds stress turbulence closure.

Section 3.2 will present the new experimental results of deposition of heavy particles dispersing in an undisturbed flow (over level terrain) or in a flow disturbed by an artificial windbreak. Section 3.3 will cover the model, emphasizing adjustments made to Thomson's (1987) passive tracer model in order to mimic heavy particle dispersion. Finally in Section 3.4, we will compare numerical simulations with the observations.

3.2 The experiment

The experiment was conducted during the summers of 2002 and 2003 in Thiverval Grignon (Yvelines, France; latitude 48.85°, longitude 1.92°, altitude 150 m) in a field belonging to the *Institut National Agronomique*; the site was flat, even and covered with short grass. Two series of experiments were carried out, one in August 2002 with a point source (series P), and one in August 2003 with a line source (series L). The particle type, fence, deposition collectors and the experimental procedure were the same across both series. During periods ranging from 20 to 30 minutes, the particles were released upwind from the fence, which stretched in a direction normal to the prevailing wind, and were collected downwind from that fence. Simultaneously, wind velocity and temperature were measured in the undisturbed upwind flow over the course of each run. The configuration of the experiments is sketched on Figure 3.1.

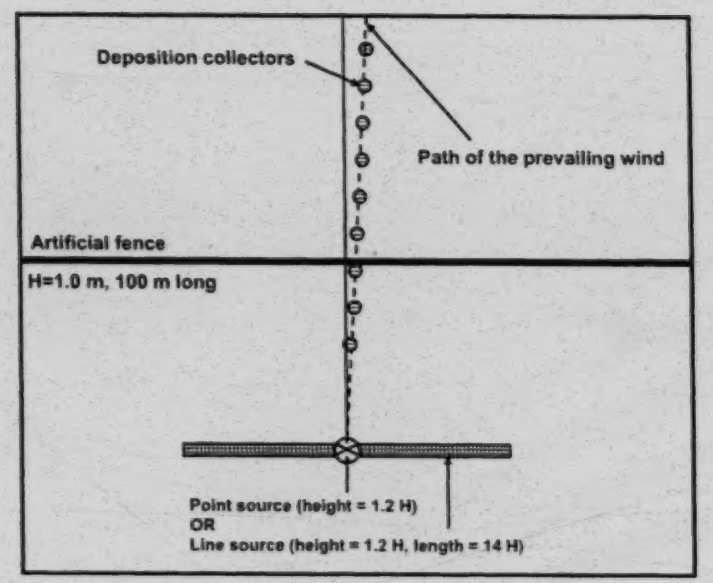
Deposition collectors
Path of the prevailing wind
Artificial fence
H=1.0 m, 100 m long
Point source (height = 1.2 H)
OR
Line source (height = 1.2 H, length = 14 H)

Figure 3.1: Top view schematic of the experimental setup. The line source lies parallel to the fence and the deposition collectors are placed along a transect that crosses the fence and is oriented in the prevailing wind direction. Note that the proportions are not respected on this schematic.

3.2.1 Material

The particles were spherical glass beads of density 2500 kg m^{-3} whose diameter (d_p) ranged from 10 to 50 μm (see Figure 3.2). We report in this paper the observed deposition of 34 ± 2 μm beads, for which class the settling velocity spans $7.7 \leq w_g \leq 9.8$ cm s^{-1}.

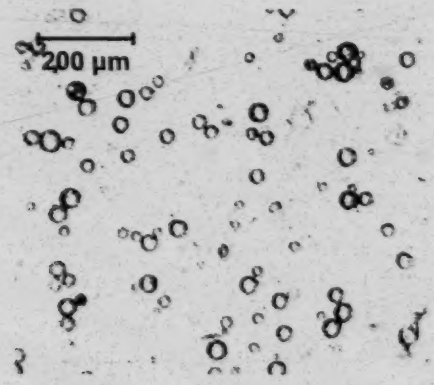

Figure 3.2: Picture of the spherical glass beads used in the experiments (here deposited over a glass strip coated with glycerin).

Series P used a point source hung from a light tripod so as to minimize interference of the source with the flow. The source height was adjustable, and particles were released under gravity (see Figure 3.3). The source consisted of a bead reservoir atop a plastic funnel, from the base of which particles were released from an orifice of diameter 1.5 mm. A small electric motor, whose rotation was unbalanced due to a metal rod fixed off-center relative to the axis of the motor, caused vibrations that rendered the beads somewhat fluid and facilitated particle flow through the funnel and the outlet. The experiments were run only in dry conditions, when the particles did not agglomerate and

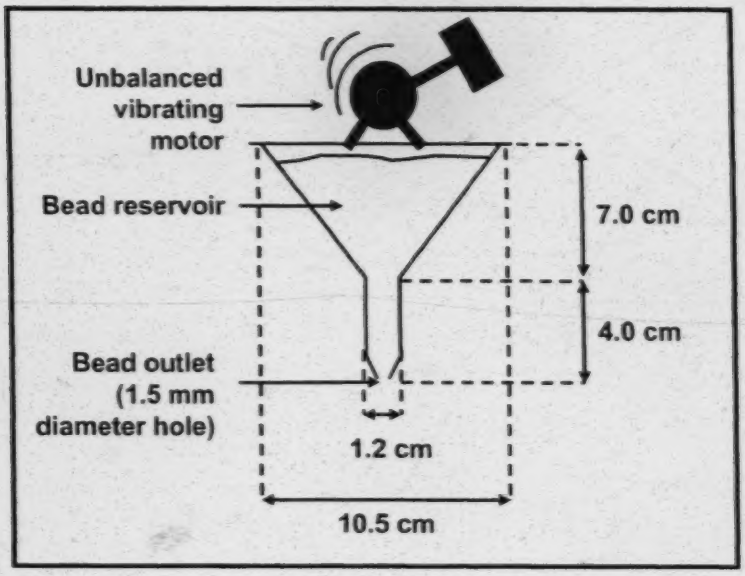

Figure 3.3: Schematic of the point source used in runs P.

clog the source. The release rate proved fairly steady throughout a run and among runs (see appendix A-3 for details).

In Series L the objective of using a line source was to simplify the numerical modeling of the dispersion experiments. In effect, the wind flow about a straight fence is statistically two-dimensional i.e. statistics of the flow do not vary in the direction parallel to the fence, and this holds even though the wind does not blow normally to it; releasing particles from a line source parallel to the fence renders the dispersion simulation two-dimensional as well. The line source was composed of nine point sources spaced at 1.75 m intervals, and each mounted on a horizontal metal rod whose height could be adjusted. As Figure 3.4 shows, each point source consisted of a wheel (100 mm in diameter) punched with holes (3 mm in diameter) along its periphery, the wheel being

partially immersed in the bead reservoir and rotated by an electric motor. Particles were blown out as the laden holes passed in front of a pressurized

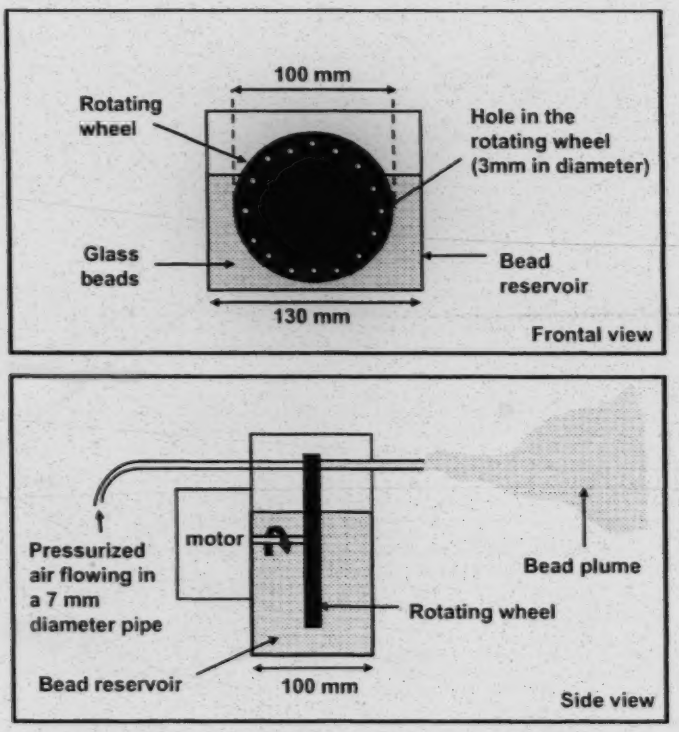

Figure 3.4: Frontal (upper schematic) and side (lower schematic) view of an element that composes the line source used in runs L.

airstream. Each source was operated by its own motor, however all the motors were mounted in parallel and powered by the same electrical (DC) supply, in order to have all the wheels rotate at the same speed. It was anticipated that some distance downwind the plumes generated by the individual point sources would merge, and lateral homogeneity in particle concentration would result. However as shown in appendix A-4, lateral homogeneity of the plume was not

achieved, mostly because individual sources composing the line source themselves had different release rates. Therefore, we measured the total mass of particles released from each individual source over each run, and expressed the source distribution as $Q(y_i) = Q_0 f(y_i)$, where $Q(y_i)$ is the release rate at the (discrete) location of the source y_i, Q_0 is the overall magnitude of the release rate, and $f(y_i)$ is the (measured) profile factor. Although we know Q_0 for the ensemble of beads of all sizes (bead diameter $5 \leq d_p \leq 45$ μm), we do not know Q_0 for beads of a particular diameter range because the size distribution of beads proved not to be constant across runs, and was not measured systematically. This remark applies to run series P and L.

An artificial porous plastic fence (height H=100 cm, length Y=100 m) was erected in a straight line perpendicular to the prevailing wind direction (112°-292°). Its resistance coefficient

$$k_r = \frac{\Delta p}{\rho \overline{u}^2} \tag{3.1}$$

(pressure drop Δp across the fence when installed so as to block a uniform, normally-incident reference flow, normalized by the dynamic pressure $\rho\overline{u}^2$, where ρ is the air density and $\overline{u}$ is the mean velocity) was measured by fixing a sample in a wind tunnel, and proved to vary slightly with the Reynolds number ($R_{em} = U\, L_m/\nu$) based on the mesh size L_m of the fence material (U is the bulk air velocity through the mesh and ν is the kinematic viscosity); a dependency of this type for screens has been previously reported, eg. by Pinker and Herbert (1967). In the range of the observed wind velocities during the experiments, $k_r \approx 1.8$.

3.2.2 Micro-meteorological measurements

A 3-dimensional ultrasonic anemometer (type R2, Gill) placed 3 m above ground and 70 m upwind from the fence, in the undisturbed flow where Monin-Obukhov similarity theory applies, measured reference flow statistics: the friction velocity ($u_\star$), the Monin-Obukhov length (L_{mo}), the surface roughness length (z_0), and the mean and standard deviation ($\overline{\theta}$, σ_θ) of the wind direction, specified relative to the normal to the fence. In addition for runs L, independent estimates of $u_\star$, L_{mo} and z_0 were inferred from mean horizontal windspeed and temperature measurements made with cup anemometers (CIMEL CE155, operating range $0.3 - 50.0\ \mathrm{m\,s^{-1}}$) and Copper-Constantan thermocouples in the reference flow at six levels (0.6 m, 1.1 m, 2.0 m, 3.0 m, 4.5 m, 6.0 m).

3.2.3 Deposition measurements

The experiments were all run when the obliquity of the mean wind relative to the normal of the fence was less than 25^o. The deposition rate was sampled at discrete locations along a transect starting from the source and running parallel to the prevailing wind direction, by means of Petri dishes (135 mm in diameter, 18 mm high) placed on the ground and filled with an electrolyte solution (isoton®). Although not perfectly flat, the collectors proved to not noticeably interfere with the measurement, as shown in appendix A-5. After each experimental run, the particle-laden isoton® was transferred from the Petri dishes to an automated liquid phase counter (Multisizer Coulter Counter®, Beckman Coulter Inc.). The machine counted the samples three times and yielded the result as a spectral distribution with respect to bead diameter (4 μm resolution). This automated procedure proved to overestimate

the particle count by 34% on average when compared with an optical count (see appendix A-6 for details); however, this bias has no impact on the results presented in this study, as explained later in section 3.4.2. From the particle count we inferred the particle deposition rate (g m^{-2} s^{-1}) of beads with diameter in the range 34 ± 2 μm. The error bars shown on the graphs of deposition swaths (Figures 3.8-3.15) represent the standard deviation of the three counts.

3.3 The particle transport model

An LS model computes an ensemble of independent particle trajectories emanating from the source, by generating for each particle a time series of velocity and integrating it with respect to time. Dispersion statistics are then inferred from the ensemble of particle paths.

In the limit of a small particle slip Reynolds number $R_{ep} = |\mathbf{v} - \mathbf{u}| d_p / \nu$, where d_p is the particle diameter and $|\mathbf{v} - \mathbf{u}|$ is the fluid to particle relative velocity, the equations of motion for a spherical particle are, following Sawford and Guest (1991):

$$\frac{dv_i}{dt} = \frac{u_i(\mathbf{x}, t) - v_i}{\tau_p} + g_i \tag{3.2}$$

$$\frac{dx_i}{dt} = v_i \tag{3.3}$$

Here v_i is the particle velocity, and $u_i(\mathbf{x}, t)$ is the fluid velocity evaluated at the position $\mathbf{x}$ of the particle at time t ; g_i is the gravitational acceleration; and τ_p is the particle inertial time scale. In this limit of small R_{ep} the approximation of Stokesian drag is valid, and

$$\tau_p = \frac{\rho_p \, d_p^2}{18 \mu} \tag{3.4}$$

where ρ_p is the particle density and μ is the dynamic viscosity of the air.

The drag term (the first term on the right hand side of Eq. 3.2) is then linearly related to the particle relative velocity. However Wilson (2000) showed that provided $\tau_p/T_L << 1$ (where T_L is the Lagrangian time scale at source height), heavy particle trajectories could be satisfactorily *approximated* merely by imposing the particle gravitational settling velocity $w_g = \tau_p\, g$ on what was (otherwise) a velocity time series appropriate to the motion of fluid elements along the trajectory of a heavy particle, viz.

$$v_i = u_i + w_g\, \delta_{i3} \tag{3.5}$$

where δ_{ij} is the Kronecker delta, and u_i stems from a Lagrangian stochastic model for fluid element trajectories, modified slightly (as specified below) to account for the inertia of a heavy particle. In this study, $\tau_p/T_L << 1$; therefore instead of using Eq. 3.2 to calculate heavy particle velocities, we used Eq. 3.5 in conjunction with a generalized Langevin equation to model the evolution of fluid element velocity u_i.

3.3.1 Generalized Langevin equation

We use Thomson's (1987) formulation of the Langevin equation as the basis for the modeling of the motion of fluid elements. The velocity u_i and position x_i of a fluid element evolve jointly as a 6-dimensional Markov process

$$du_i = a_i(\mathbf{x}, \mathbf{u})\, dt + b_{ij}\, dW_i \tag{3.6}$$

$$dx_i = u_i\, dt \tag{3.7}$$

where dW_i is a three dimensional Wiener process (White noise), i.e. a stochastic process whose mean is zero ($< dW_i >= 0$) and whose correlation is such that

$< dW_i(t) dW_j(t+dt) >= \delta_{ij} dt$. The first term on the right hand side of Eq. (3.6) involves the conditional mean acceleration a_i, and the second is a stochastic term resulting from the fluctuating pressure and viscous forces. Following Thomson (1987) we require

$$a_i = -\frac{C_0 \epsilon}{2} \delta_{ij} \Gamma_{jk} (u_k - \overline{u}_k) + \frac{\phi_i}{g_a} \tag{3.8}$$

$$b_{ij} = \sqrt{C_0 \epsilon}\, \delta_{ij} \tag{3.9}$$

in order to satisfy the 'well-mixed constraint' and the Kolmogorov hypothesis of local isotropy. In Eqs. 3.8-3.9 ϵ is the rate of dissipation of the turbulent kinetic energy and C_0 is the Kolmogorov 'universal constant' associated with the Lagrangian velocity structure function. For multidimensional LS models, $C_0 \approx 4.4$ (Du, 1997). Γ_{ij} $(= \tau_{ij}^{-1})$ is the inverse of the Reynolds stress tensor τ_{ij}; u_k and $\overline{u}_k$ are the k-components of respectively the instantaneous Lagrangian velocity and time average wind velocity. In heterogeneous Gaussian turbulence, the term ϕ_i / g_a in Eq. 3.8 is

$$\begin{aligned} \frac{\phi_i}{g_a} = {} & \overline{u}_l \frac{\partial \overline{u}_i}{\partial x_l} + \frac{\partial \overline{u}_i}{\partial x_j} (u_j - \overline{u}_j) + \frac{1}{2} \frac{\partial \tau_{il}}{\partial x_l} \\ & + \frac{1}{2} \overline{u}_m \frac{\partial \tau_{il}}{\partial x_m} \Gamma_{lj} (u_j - \overline{u}_j) + \frac{1}{2} \frac{\partial \tau_{il}}{\partial x_k} \Gamma_{lj} (u_j - \overline{u}_j)(u_k - \overline{u}_k) \end{aligned} \tag{3.10}$$

We do not know the probability density functions of the velocity in the disturbed flow about the fence, which surely would not be precisely Gaussian. Nevertheless we chose to formulate ϕ_i / g_a as in Eq. 3.10 on the principle of simplicity, regarding it as reasonable because, as noted by Flesch and Wilson (1992; Sec. 4) in the context of dispersion in canopy flow, the effects of severe horizontal inhomogeneities likely are more important than the effects of skewness and kurtosis. Our choice is also supported by the findings of Leuzzi and Monti (1998), who demonstrated the good skills of Eq. 3.10 for the dispersion

of fluid elements in a disturbed flow.

3.3.2 Adjustments to the Langevin equation for heavy particle dispersion

The Lagrangian Stochastic model described above allows to simulate the velocity time series of passive tracer particles. Yet, in consequence of their inertia, heavy particles do not follow the fluid streamlines and sample different fluid velocities. Reynolds (2000) suggests that LS models for passive tracer particles are still appropriate to simulate fluid velocities along heavy particle trajectories, provided the Lagrangian time scale is appropriately modified to account for the Crossing Trajectory Effect (CTE).

The Crossing Trajectory Effect (CTE)

The CTE was first described by Yudine (1959), and later by Csanady (1963), Wells and Stocks (1983), and others. Passive tracer particles remain in the same fluid environment during their (Lagrangian) trajectory, and the fluid velocity along those trajectories decorrelates with time, as a result of eddy decay. The time scale of the velocity auto-correlation associated with this phenomenon is called the Lagrangian time scale (T_L). On the other hand, heavy particles fall out of eddies under the action of inertia and gravity, and continuously change their driving fluid environment. The consequence is a reduction in the velocity auto-correlation. As Hinze (1975, p.470) notes, the auto-correlation of a heavy particle can be considered as "the result of the combined effect of the Lagrangian auto-correlation of the originally 'surrounding' fluid and of the spatial Eulerian correlation corresponding to the distance at the instant considered between the centroids of the discrete particle and of the originally surrounding fluid". Applying this idea, Sawford and Guest

(1991), following Csanady (1963), suggested the autocorrelation timescale may be parameterized

$$T_{p\alpha} = \frac{T_{L\alpha}}{\sqrt{1 + (\beta \frac{w_g}{\sigma_\alpha} \frac{E\alpha}{E\delta})^2}} \tag{3.11}$$

where α labels the direction of dispersion; δ labels the direction of sedimentation (in the present case, the vertical axis); σ_α is the velocity standard deviation in direction α; $_E$ is the Eulerian length scale; and

$$\beta = \frac{T_L}{T_E} = \sigma \frac{T_L}{E} \tag{3.12}$$

is an empirical factor of order 1 relating Eulerian and Lagrangian scales (Corrsin, 1963). Raupach (2002) gave experimental evidence for the utility of Eq. 3.11, which we therefore retain. There is no general agreement on the value of β, experimental studies reporting values ranging from 1 to 20 (Wells, 1982). Given the strong heterogeneity of the windbreak flow, it makes sense to relate β to local characteristics of the flow. Following Saffman (1962), we write

$$\beta = \chi \frac{\overline{u}}{\sigma_u} \tag{3.13}$$

where $\chi = {}_L/_E$ is the ratio of the Lagrangian to Eulerian length scales; $\overline{u}$ and σ_u are respectively the local mean and standard deviation of the streamwise velocity. From the experimental observations of Sato and Yamamoto (1987) and the analytical study of Wang et al. (1988), we expect $0.1 \leq \chi \leq 1$. When prescribing the value of χ in this range, β is of order 1 in all the runs we present.

The Continuity Effect

As noted by Csanady (1963), in the limit of frozen turbulence (i.e. when the particles fall through eddies in a period much shorter than the turbulence time

scale), the Lagrangian autocorrelation of the lateral (relative to the direction of the drift) fluid velocity is negative over some range of lag-times. Physically, this means that a back-flow occurs along the direction of the drift, and it results in a reduced integral time scale for lateral dispersion, the 'continuity effect'. Raupach (2002) shows that the longitudinal (relative to direction of dispersion considered) correlation length scale is twice the lateral correlation length scale, thus we adjust Eq. 3.11 to

$$T_{p\alpha} = \frac{T_{L\alpha}}{\sqrt{1 + (\beta \frac{w_g}{\sigma_\alpha} \gamma)^2}} \tag{3.14}$$

where $\gamma = {}_{E\alpha}/_{E\delta} = 1$ when one considers dispersion parallel to the drift (i.e. $\alpha = \delta$), and $\gamma = 2$ otherwise ($\alpha \neq \delta$).

3.3.3 Reproducing the experimental conditions

To compute particle trajectories, wind velocity statistics must be provided along the particles' paths. Thus for each experimental run we calculated a synthetic flow field in a computational domain 200 H long and 50 H high (where H is the height of the fence), using a Reynolds Averaged Navier-Stokes (RANS) wind model with a second-order turbulence closure (Wilson, 2004). The inflow profiles of the velocity statistics were specified as the 1-dimensional (1-d) equilibrium solution for prescribed approach flow state and orientation (u_*, L_{mo}, z_0, $\overline{\theta}$). The RANS model provided the disturbed field of all statistics (up to the second order) of the wind flow about the wind break, i.e. fields of mean velocity, Reynolds stress τ_{ij} and turbulent kinetic energy dissipation rate ϵ. Please note that the modelled flow statistics were consistent with the available (ie. single upwind point) micro-meteorological parameters as determined by the sonic anemometer (see Tables 1-2). In particular the modelled flow

statistics accounted for both the obliquity of the wind flow to the fence and the thermal stratification of the air. As an illustration, Figure 3.5 presents the disturbance in the mean horizontal wind speed and turbulent kinetic energy caused by a fence erected perpendicularly to the flow, in the conditions of run P5. Through the averaging process inherent to RANS modelling, detailed information is lost about the instantaneous fluid structure. With the Lagrangian Stochastic model, we reconstruct the fluctuating velocity along particle trajectories, 'driving' the LS model with the RANS flow field resolving the fence. More precisely, the wind statistics at a particular location $\mathbf{x}$ were obtained from a linear interpolation in between the values provided by the RANS model at the four mesh points adjacent to $\mathbf{x}$. As an illustration, Figure 3.6 shows a side view of trajectories simulated by the LS model in an undisturbed flow (Panel a) and in a fence-disturbed flow (Panel b), in the meteorological conditions of run L1. This clearly shows the dramatic impact of the fence on the trajectories of heavy particles. The simulations of particle dispersion were run with 34 μm diameter glass beads ($w_g = 8.7$ cm s^{-1}), for comparison with the observed deposition pattern of 34 ± 2 μm ($7.7 \leq w_g \leq 9.8$ cm s^{-1}) beads. In runs L, the particles' trajectories were initiated at the location of one of the nine individual source according to the distribution $f(y)$ of the line source. A top view of particle trajectories of run L1 ($\overline{\theta} = 12.4°$, $\sigma_\theta = 20.1°$) is shown on Figure 3.7. It illustrates the source distribution of the line source (series L), as well as the wind direction variability.

Treatment of vertical and cross-wind dispersion

The Langevin equation (Eq. 3.6) accounts for the fluctuation of the wind velocity in the three directions. The velocity statistic pertaining to the vertical

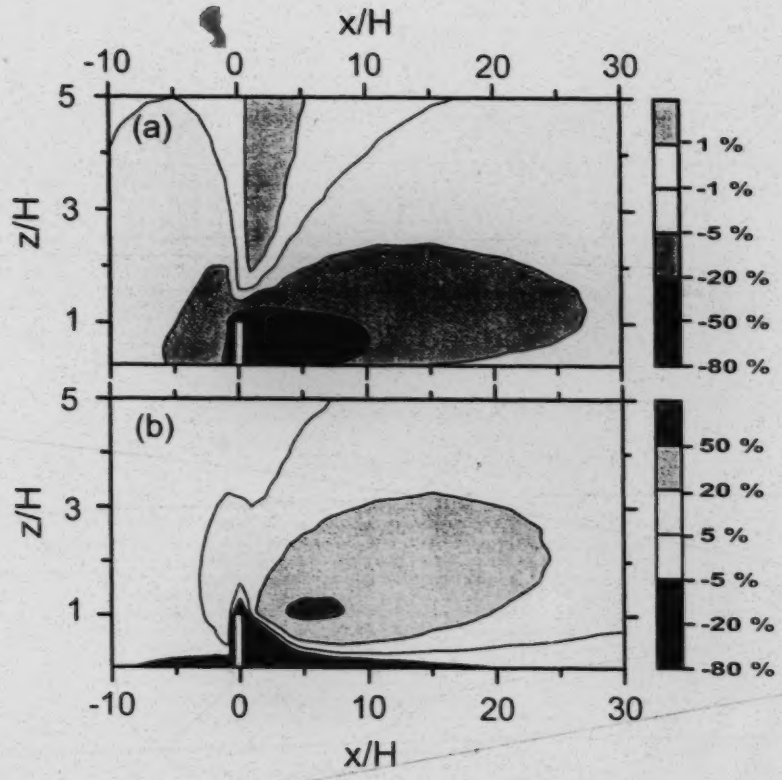

Figure 3.5: Windbreak induced disturbance of the horizontal average velocity field (Panel a) and of the turbulent kinetic energy field (Panel b), in percent difference relative to the undisturbed values at the same height. The simulations were runs in the conditions of run P5: $u_* = 0.53\ \mathrm{m\,s^{-1}}$, $L_{\mathrm{mo}} = -83$ m, $z_0 = 0.04$ m, $\overline{\theta} = 6.2°$, $k_r = 1.73$.

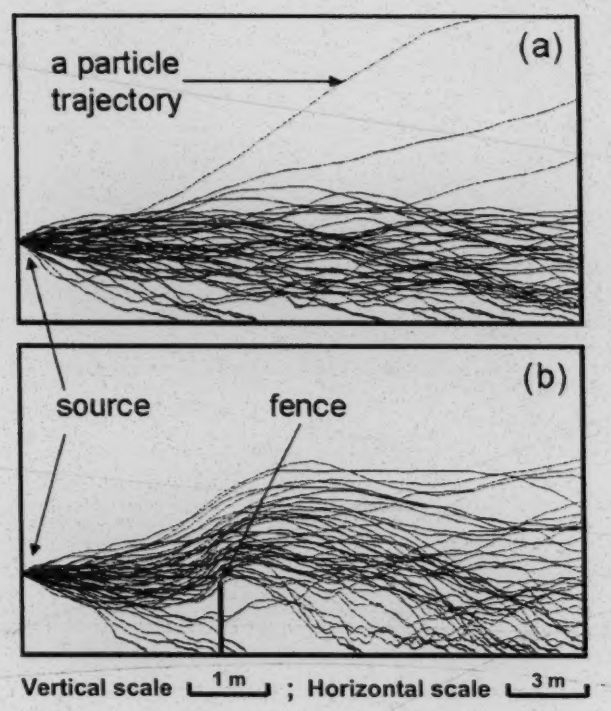

Figure 3.6: Side view of particle trajectories simulated by the LS model coupled with the RANS model which supplies the wind flow statistics. Trajectories are simulated in an undisturbed wind field (Panel a) or in a wind field disturbed by an infinitely thin fence (Panel b). The micro-meteorological conditions are those of run L1.

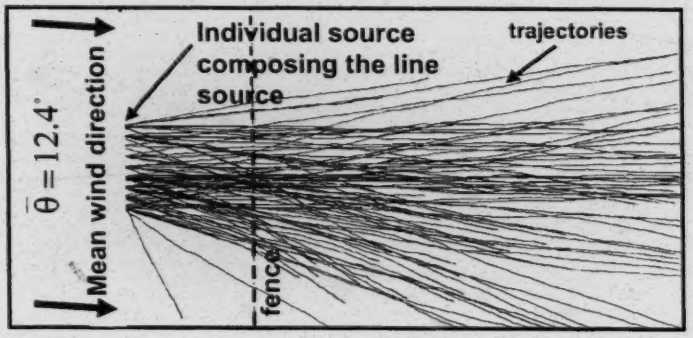

Figure 3.7: Top view of the trajectories of particles released by the line source, computed in the conditions of run L1 ($\overline{\theta} = 12.4°$, $\sigma_\theta = 20.1°$).

dispersion is the variance of the wind vertical velocity σ_w^2, whereas σ_u^2 and σ_v^2 control the particle horizontal dispersion (note: the component u is perpendicular to the fence, and v is parallel). These are calculated by the RANS model throughout the 2-dimensional flow domain. The inflow boundary profiles are an equilibrium (1-d) solution, subject to the upper (z_T) boundary condition

$$\sigma_u^2(z_T) = C_{uu}(z_T)\, u_*^2 \tag{3.15}$$

$$\sigma_v^2(z_T) = C_{vv}(z_T)\, u_*^2 \tag{3.16}$$

$$\sigma_w^2(z_T) = C_{ww}(z_T)\, u_*^2 \tag{3.17}$$

where u_*^2 is the (height-independent) shear stress of the equilibrium solution; the lower boundary condition is analogous. Here C_{uu} is the normalized velocity variance in an equilibrium surface layer, but recall that for the fence flow simulations coordinate axes are *not* precisely aligned with the mean wind. Therefore C_{uu} differs from its counterpart C_{uu0} defined relative to axes aligned with the mean wind, and we have the transformations

$$C_{uu}(z) = \cos^2(\overline{\theta})\, C_{uu0}(z) + \sin^2(\overline{\theta})\, C_{vv0}(z) \tag{3.18}$$

$$C_{vv}(z) = \sin^2(\overline{\theta})\, C_{uu0}(z) + \cos^2(\overline{\theta})\, C_{vv0}(z) \tag{3.19}$$

where $\overline{\theta}$ is the mean wind direction relative to the normal to the fence. Following Kroon and de Bruin (1993) we parameterized the stability-dependence of the coefficients C_{uu0} etc. as:

$$C_{uu0}(z_T) = C_{uu0}^* + 0.2 * (-z_T/(L_{mo} k_v))^{2/3} \tag{3.20}$$

$$C_{vv0}(z_T) = C_{vv0}^* + 0.2 * (-z_T/(L_{mo} k_v))^{2/3} \tag{3.21}$$

$$C_{ww}(z_T) = C_{ww}^* (1 - 3 z_T/L_{mo})^{2/3} \tag{3.22}$$

where L_{mo} was negative for our experiments, and $C_{uu0}^* = C_{uu0}(z = 0)$ (etc).

In summary, the computed equilibrium (1-d) profiles of velocity variance are known to be unrealistic at the interior of the computational domain, far from the upper and lower boundaries (eg. Fig. 6.2 of Bink, 1996) at which they are pinned to imposed (and plausible) values. In relation to computed (2-d) shelter-flow fields this is doubly significant: the (poor) 1-d profile serves as the inflow boundary condition; and the same implicit imperfection of the turbulence closure must impact the computed *disturbance* of the equilibrium fields (eg. Wilson, 2004, whose computed velocity standard deviations did not accord well with measurements in the lee of a fence).

Accepting that the computed fields of velocity variance will be imperfect, the best we can do is to enforce realistic (upper and lower) boundary values. Considering first the vertical velocity variance, Figure 3.8 presents the deposition swath computed for each of the specifications $C^*_{ww} = 1.5,\ 2.0$ or 2.5, the other parameters being otherwise consistent with the experimental conditions of run L2. Unsurprisingly, the numerically simulated deposition rates are sensitive to the value of C^*_{ww}, so in what follows we have prescribed for C^*_{ww} the values actually observed in each run, as reported in Table 3.1.

Turning to the horizontal spread, we first note that the sonic measurements of σ_u^2 and σ_v^2 in the 'undisturbed' flow upwind from the fence showed that C^*_{uu0} and C^*_{vv0} were very variable (see Table 3.1), and overall of larger magnitude than values usually reported for the surface layer over level terrain (see the range of values given by Loubet, 2000), viz.

$$C^*_{uu0} = 4.0 \tag{3.23}$$

$$C^*_{vv0} = 1.9 \tag{3.24}$$

Large values of C^*_{vv0} imply large wind direction variability, which is common

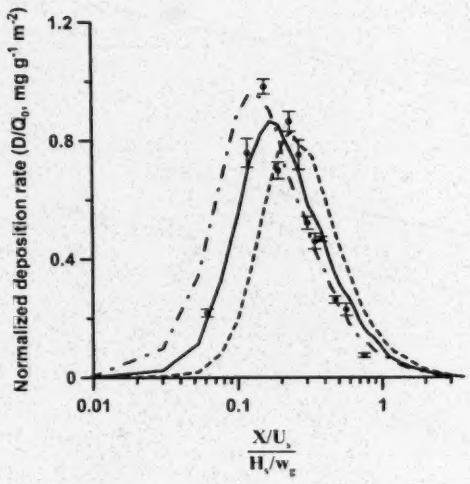

Figure 3.8: Deposition swath of particles dispersing in the experimental conditions of run L2. The dots present the experimental data, while the curves show the numerical simulations, when $C^*_{ww} = 1.5$ (dashed line), $C^*_{ww} = 2.0$ (solid line), or $C^*_{ww} = 2.5$ (dashed-dotted line).

when the wind is light (Brusasca et al., 1992). We did indeed record the largest variability in low wind conditions ($\sigma_\theta = 32.8°$ with mean cup windspeed $\overline{u}(z = 1\,\mathrm{m}) = 0.6\,\mathrm{m\,s^{-1}}$ in run P2). In the other runs however, the wind was stronger (see Table 3.1). We can only assume that the generally high variability of wind direction encountered in these experiments owes to the *wakes of buildings* that stood about 100 m upwind of the experiment site.

When using the standard values of the constants C^*_{uu0} and C^*_{vv0} (Eqs. 3.23-3.24), the lateral spread of particles as simulated by the LS model was significantly underestimated (see Figure 9). It therefore seemed justifiable to use the sonic measurements of $\sigma_\mathrm{u}, \sigma_\mathrm{v}$, and in modelling the experiments to impose boundary values (of $\sigma_\mathrm{u}, \sigma_\mathrm{v}$) that would be consistent with them. Unfortunately however, the RANS closure model cannot solve the wind field for just *any* specification of C^*_{uu0} and C^*_{vv0}, and in particular with the values we observed. Therefore we chose to multiplicatively re-scale the computed fields of σ_u, σ_v generated by the RANS model, using a constant multiplication factor for each component, so that these fields matched the observed σ_u, σ_v in the upwind flow. We shall label this approach to lateral dispersion 'treatment 1'. As shown in Figure 3.9, under treatment 1 the LS simulations better reproduce the observed lateral spread of particles.

Another approach to improving the simulation of crosswind spread ('treatment 2') is to require that (the computational) particles should travel in a flow field consistent with the *observed* distribution of the wind direction. In their dispersion simulation of passive tracers in low wind speed conditions, Brusasca et al. (1992) handled with some success the wind direction variability in a similar fashion. The true wind direction distribution is continuous, but we discretized it into fifteen directional classes centered on obliquity angles

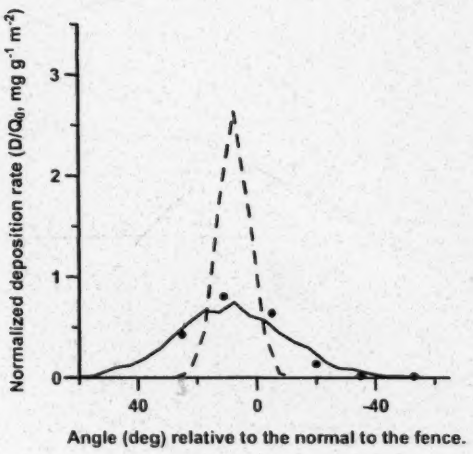

Figure 3.9: Cross-wind deposition swath of particles along the 20 m radius arc of circle centered on the source, for run P5.
Dots: experimental data; the error bars represent the standard deviation of the three automated counts.
Dashed line: LS Simulation with σ_u, σ_v fields generated from the standard values for C_{uu0} and C_{vv0} (Eqs. 3.23-3.24).
Solid line: Simulation with σ_u, σ_v fields corrected according to treatment 1.

$\theta_n = \overline{\theta} + 10n$, where $n \in [-7;7]$ and $\overline{\theta}$ is the mean wind direction relative to the normal to the fence. For each of these wind direction classes, we generated a different RANS flow field. The ensemble of computed LS paths sampled these fifteen direction classes so as to replicate the observed distribution of the wind direction over the period of the experimental run. In Figure 10 we present observations of cross-wind deposition swath for runs P1 (Panel 10a), P4 (Panel 10b), P5 (Panel 10c), and we show comparatively the simulation results obtained with the two alternative treatments of lateral dispersion. Since the agreement with the observed cross-wind swath is noticeably improved using treatment 2, for all further simulations treatment 2 has been retained.

Particle entrapment by the fence

In runs P3, P4, P5, L1 and L2, the windbreak not only disturbs the windflow carrying particles; it also physically obstructs the particle plume flowing through it, i.e. particles may deposit and remain entrapped on the fence. Raupach (2001) shows that the particle transmittance (κ) across a porous screen is related to the optical porosity (η) as:

$$\kappa \approx \eta^{m E_I} \tag{3.25}$$

where E_I is the efficiency of deposition onto the screen material and m is a meandering factor ($m \approx 1$ in our case, for the windbreak is thin). We may estimate the optical porosity of the present fence (η) from a relationship given by Pinker and Herbert (1967)

$$\eta \approx \sqrt{\frac{0.52}{k_r + 0.52}} \tag{3.26}$$

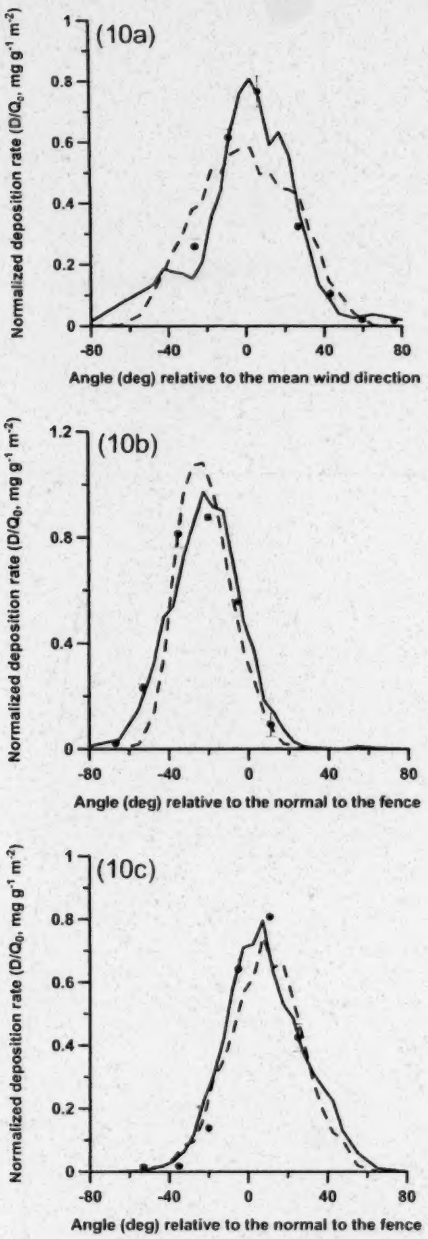
(10a)
Normalized deposition rate (D/Q0, mg g-1 m-2)
Angle (deg) relative to the mean wind direction
(10b)
Normalized deposition rate (D/Q0, mg g-1 m-2)
Angle (deg) relative to the normal to the fence
(10c)
Normalized deposition rate (D/Q0, mg g-1 m-2)
Angle (deg) relative to the normal to the fence

Figure 3.10: Cross-wind deposition swath of runs P1 (Panel 10a), P4 (Panel 10b), and P5 (Panel 10c), along a 20 m radius arc of circle centered on the source. Comparison between the experimental data (dots) and the LS simulations with treatment 1 (dashed line) or with treatment 2 (solid line) of the lateral dispersion. The error bars show the standard deviation of the three automated counts for each measurement.

which connects a barrier's optical porosity with its resistance coefficient k_r, a property we had measured in a wind tunnel: from $k_r = 1.8$ we deduce $\eta \approx 0.5$. As to the coefficient of impaction I, following Raupach et al. (2001)

$$E_I = \left(\frac{S_t}{S_t + 0.8}\right)^2 \tag{3.27}$$

where $S_t = 2\overline{u}\,\tau_p / L_m$ is the Stokes number of the particles relative to the screen material, L_m is the length scale of elements of the mesh on which particles impact, and $\overline{u}$ is the mean velocity of the flow bleeding through the screen. In modelling the experiments we randomly terminated a proportion $(1 - \kappa)$ of the particle trajectories that intersected the fence, so as to enforce the transmittance (κ) calculated with Eqs. 3.25-3.27. In our experimental conditions, $\kappa \approx 0.5$.

On the values used for χ

In principle, the values χ depend on the characteristics of the flow, and therefore may differ from one run to another, and even across different regions of a given flow. However a rigorous parameterization for χ is unavailable. Therefore, we kept χ constant. Figure 3.11 presents the LS computed deposition swath in the conditions of run P3 (see Table 3.1) when $\chi = (0.1, 0.5, 1.0)$, i.e. with values of χ spanning in the rage of values reported in the literature (see section 3.3.2). The results are very similar, showing that the computed deposition swath is not very sensitive to the value of χ. In the numerical simulations presented in this study, we prescribed $\chi = 0.3$.

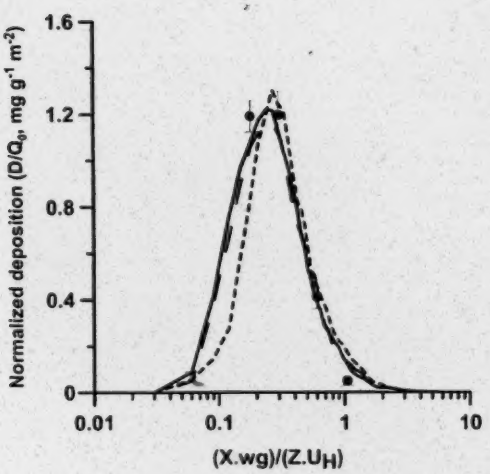

Figure 3.11: Deposition swath computed by the LS model in the experimental conditions of run P3, when $\chi = 0.1$ (solid curve), $\chi = 0.5$ (long dashed curve) and $\chi = 1.0$ (short dashed curve). The dots represent the experimental data.

3.4 Results

3.4.1 Micrometeorological data

The micrometeorological statistics ($u_\star$, $L_{\rm mo}$, z_0, $\overline{\theta}$, σ_θ) computed from the sonic anemometer measurements in the reference flow are presented in Table 3.2. Only in runs L1 and L2 could the statistics also be calculated from profile measurements, and in those two experiments we obtained a reasonably good match between the statistics obtained from the two independent methods. For run L1, the sonic anemometer measurements yielded $u^\star = 0.20$ m s^{-1}, $L_{\rm mo} = -15$ m and $z_0 = 3 \times 10^{-3}$ m when the profile technique gave $u_\star = 0.17$ m s^{-1}, $L_{\rm mo} = -56$ m and $z_0 = 5 \times 10^{-3}$. For run L2, the match is closer: $u_\star = 0.37$ m s^{-1}; $L_{\rm mo} = -120$ m and $z_0 = 8 \times 10^{-3}$ (from sonic anemometer) versus $u_\star = 0.36$ m s^{-1}; $L_{\rm mo} = -353$ m and $z_0 = 7 \times 10^{-3}$ (from profiles). This broad consistency, although limited to two experiments, suggests the sonic anemometer measurements are fairly reliable. Note that we do not have measurements of the velocity statistics in the wake of the fence allowing to verify the computed flow.

3.4.2 Deposition

Using the fully 3-dimensional trajectory model described in section 3.3 we numerically simulated the eight experimental runs documented in Tables 3.1-3.2. The numerical and experimental results for runs over level terrain are compared on Figure 3.12, while Figure 3.13 compares theory and observation for runs when the winds were disturbed by the fence. Deposition rates have been normalized by source strength Q_0 and are plotted against $(X\ w_{\rm g})/(\overline{u}_{\rm S}\ H_{\rm s})$, the normalized 'travel time' of particles built with X, the distance downwind

of the source, the gravitational settling velocity w_g, and the velocity $\overline{u}_s$ at the source height H_s. As the experimental source strength is unknown, we optimized agreement with the simulation by requiring minimal mean square error, ie. in effect we re-scaled the experimental deposition rates by an arbitrary factor that varied from run to run; Table 3.2 gives the values of Q_0 used to scale measured deposition, for each experiment. This re-scaling is justified by the fact that deposition rates are linearly related to the source strength. After this fitting procedure, for each run we computed the normalized root-mean-square error (n.r.m.s. error, Err) between the modelled and the (rescaled) observed deposition rates; please note we normalized using the model's *peak* deposition rate.

From a glance at the deposition swaths presented in Figures 3.12-3.13, the reader will notice that the computed normalized deposition rates peak at values within $0.9 \leq (D/Q_0)_{\text{peak}} \leq 2.2$ mg g^{-1} m^{-2}, except in runs P2 and P6 where deposition rates reach strikingly larger values (respective peak values $(D/Q_0)_{\text{peak}} = 14.0,\ 10.0$ mg g^{-1} m^{-2}) and where the deposition swathes are noticeably narrower. Qualitatively these higher peak deposition rates are accounted for by the prevailing light wind conditions of runs P2, P6, as a result of which the rate of spread was weak leading to strong concentration and intense deposition. The statistical relationship given by Bouvet and Wilson (2005) between the peak deposition and the variable $\overline{u}(z = H_s)/w_g$, valid for deposition over uniform terrain, predicts that the deposition peak in run P2, where $\overline{u}(z = H_s) = 0.6$ m s^{-1}, is 7 times larger than in run P1, where $\overline{u}(z = H_s) = 1.8$ m s^{-1}. This is consistent with our simulations which yield $(D/Q_0)_{\text{peak}} = 14.0$ for P2 versus $(D/Q_0)_{\text{peak}} = 2.2$ for P1. Although the wind is substantially stronger in run P6 ($\overline{u}(z = H_s) = 1.5$ m s^{-1} far upwind of

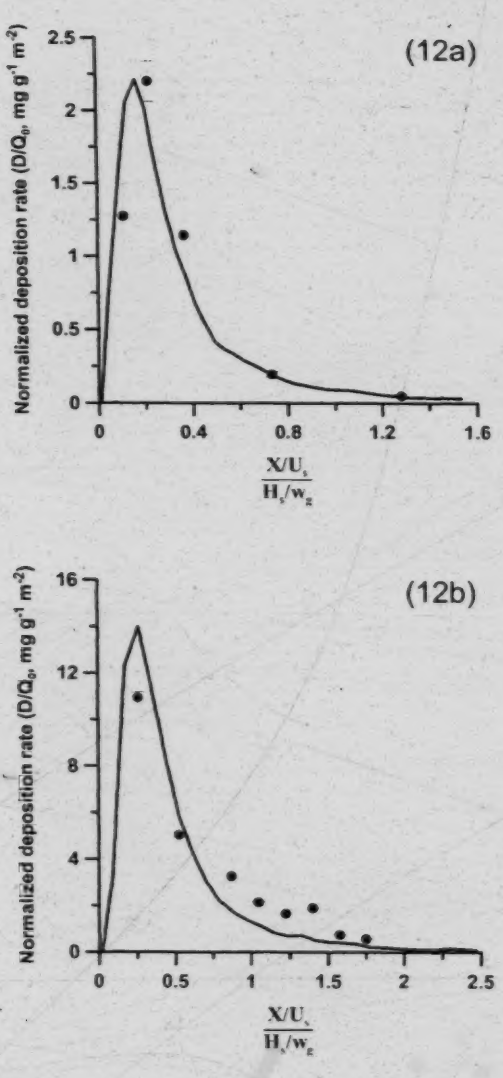

Figure 3.12: Deposition swath of particles after dispersion over uniform terrain: numerical results (solid line) versus experimental data (dots). The error bars show the standard deviation of the three automated counts for each measurement. Simulations for runs P1 (Panel 12a) and P2 (Panel 12b), with $\chi = 0.3$.

the fence in the undisturbed flow, the source was placed at the level of the fence; in turn particles sampled the reduced horizontal velocities behind the fence immediately after release, again with the result of a narrow and intense deposition swath.

In runs P1, P2 (Figure 3.12), the particles dispersed over homogeneous terrain (no fence). For case P1, the numerical result matches the experimental data rather well. For case P2, performed (as we noted above) under much lighter winds with stronger instability, the 'leading edge' of the swath was too close to the source to be revealed by the observations. It is therefore impossible to comment on the placement of the (model's) deposition peak, but evidently the model swath is too narrow. Nevertheless in view of the fact that model and observation are being compared on linear axes, it seems fair to say that the numerical model gives a satisfactory qualitative picture of the deposition swath for runs P1, P2 and indeed the normalized root-mean-square errors ($Err = 14.7\%, 10.2\%$ respectively) are satisfactorily low. These results are consistent with the conclusions of Wilson (2000), who tested LS models for heavy particle dispersion over level terrain against the experimental deposition data of Hage (1961) and Walker (1965) and reported that the 'Langevin' LS model (quite similar to the model used in our study) gave a reasonable estimate of the location, width and peak magnitude of the particle deposition swath.

The situation when a fence (artificial windbreak) disturbed the wind flow is presented on Figure 3.13. For three of the four runs (P3, P4, P6) that used a point source, there is a very satisfactory correspondence between the simulated and observed deposition swaths (Err is respectively 7.0%, 10.7% and 12.3%). The anomaly is run P5, for which the simulated deposition swath is displaced downwind relative to the observations and is too wide, with the

result that n.m.r.s. error $Err = 28.0\%$. With $u_* = 0.53\,\mathrm{m\,s^{-1}}$ this was the windiest of all the experiments, but it was not categorically windier than run P4 ($u_* = 0.46\,\mathrm{m\,s^{-1}}$). The simplest explanation for the mismatch of model and measurement for P5 would be to blame the sonic anemometer as having overestimated the shear stress; but this would be gratuitous, for we have no evidence to support that speculation.

For the final two experiments (L1 and L2, with a line source), the streamwise resolution of the deposition measurements was refined. The position of onset of the (modelled) deposition swath is too far downstream for run L1, but this experiment was performed during winds of a high turbulence intensity (ie. velocity fluctuations large in comparison with the mean wind; see Table 3.2), a factor which may well account for the curiously broad peak of the measured deposition swath, and which mitigates against the success of the simplistic Reynolds-stress turbulence closure. Despite the fairly mediocre match conveyed visually by Figure 3.13e, the figure of merit for run L1 is acceptable ($Err = 19.1\%$). The match is significantly better ($Err = 10.2\%$) in run L2. Again we emphasize that the comparability of model and measurements on a linear axis implies a rather satisfactory *practical* description of the causal mechanism of spread has been attained.

3.4.3 Discussion and Conclusions

The fence interferes with the dispersion of particles in two ways: firstly, it traps some of the particles flowing through it; secondly, it disturbs the wind flow carrying the particles. The importance of direct deposition must depend on the relative positions of source and fence. In run P3, with the source slightly above the top of the fence and just upstream, ground deposition is significantly

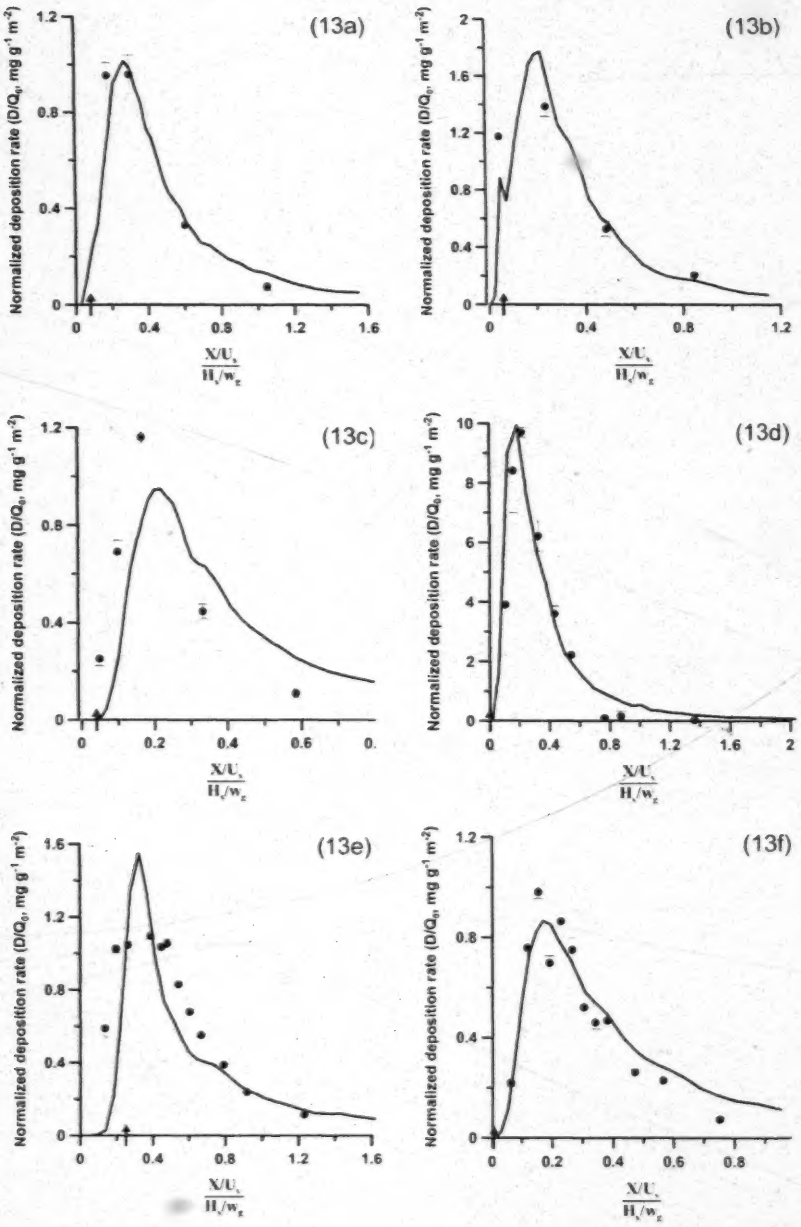

Figure 3.13: Deposition swath of particles dispersing about a fence: numerical results (solid line) versus experimental data (dots). The error bars show the standard deviation of the three automated counts for each measurement. The arrow placed on the horizontal axis shows the position of the fence. Simulations for runs P3 (Panel 13a), P4 (Panel 13b), P5 (Panel 13c), P6 (Panel 13d), L1 (Panel 13e) and L2 (Panel 13f), with $\chi = 0.3$.

reduced by particle entrapment on the fence, as shown by Figure 3.14 which contrasts the simulated deposition swaths when particles deposit onto the fence (according to Eq. 3.25) and otherwise.

The disturbance of the flow by the windbreak critically impacts the (ground) deposition pattern too. Figure 15 shows the influence of the wind disturbance for the conditions of run P3, contrasting the deposition swath as it would be *without* disturbance (case (a); the upwind, horizontally-uniform flow extended to the entire domain) and *with* disturbance, but excluding the direct filtering effect of the fence itself (case (b)). The wind disturbance lowers the peak deposition flux, and slightly shifts the position of the deposition peak downwind. Conservation of mass demands that to compensate the reduced peak deposition rate, the deposition swath in the disturbed flow must feature larger deposition rates in the trailing edge. However this is indistinguishable on Figure 15, where a small downwind increase is spread over a large area far from the source.

The fence alters wind velocity statistics in a complex way (eg. Figure 3.5) and the reader may wonder which (if any) aspect of the disturbance dominates the modification of the deposition swath. Figure 3.15 shows also the deposition swath that would result when the vertical velocity is artificially set to zero, the other velocity statistics being otherwise as provided by the RANS disturbed-flow solution (case (c)). Relative to a swath in (fully) disturbed flow (case (b)), in this (non-existent) case the deposition swath is shifted upwind, is narrower, and is more peaked. This shows the crucial role of the lifting of the particle plume by the positive mean vertical wind near the fence, which results in greater downwind drift and greater spread before deposition. If contrariwise the *horizontal* wind profile is held undisturbed (whereas the vertical velocity

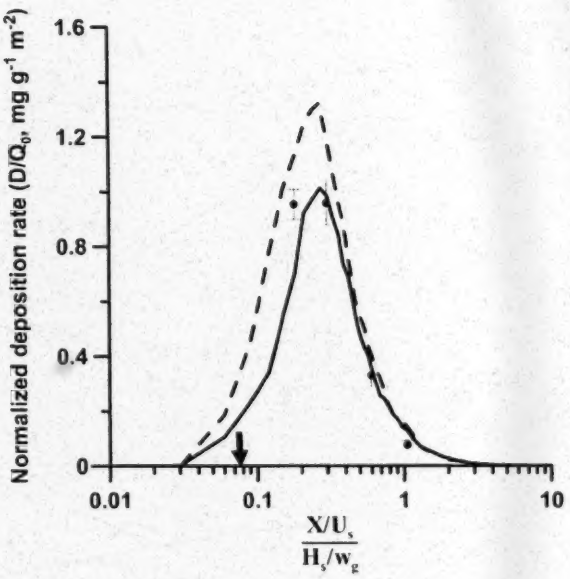

Figure 3.14: Normalized deposition swath of particles dispersing in a fence-disturbed flow computed in the experimental conditions of run P3, when particles flow freely through the fence without being entrapped (dashed line) or when particles are allowed to deposit onto the fence (solid line), with an entrapment rate of about 50%. The dots represent the experimental data, and the arrow placed on the horizontal axis shows the location of the fence.

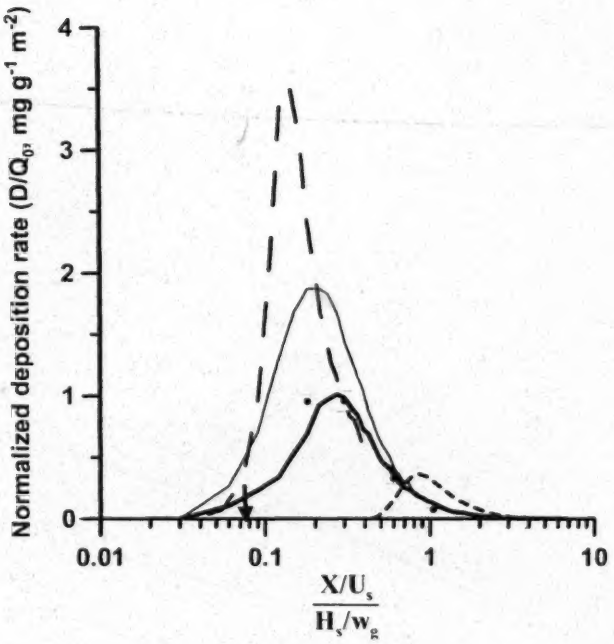

Figure 3.15: Computed deposition swath of particles dispersing in the reference flow (thin solid line, case a) or in a flow disturbed by the fence which does not entrap particles (thick solid line, case b), the experimental conditions being otherwise those of run P3. The dashed curves show the deposition swath of particles in a 'windbreak-disturbed flow', when the mean vertical velocity field (long-dashed curve, case c) or the mean horizontal velocity (short-dashed curve, case d) are forced artificially to equal values of the (undisturbed) reference flow, the other wind velocity statistics being otherwise unaltered. The dots represent the experimental data, and the arrow placed on the horizontal axis shows the position of the fence. (Note: Due to the crosswind spread and the use of a logarithmic axis, these deposition curves are not constrained to have equal area).

is permitted to act; case (d)), then relative to the swath in (fully) disturbed winds (case (b)) the deposition swath is shifted downwind, with wider spread and reduced peak deposition rate, i.e. the drastic horizontal wind velocity reduction in the vicinity of the windbreak causes particles to deposit significantly earlier, reducing spread. Thus, the disturbances to the mean *horizontal* wind and mean *vertical* wind affect the deposition swath in contrary senses, and the 'true' effect of the windbreak lies intermediate between those two asymptotic (and artificial) situations. On Figure 3.16 we show the particle concentration fields corresponding to the cases described above.

How reliable are the present results, where they hinge on the trajectory model? We know that fluid element trajectories in horizontally-uniform surface layer are calculated realistically by the LS (Langevin equation) model. The addition of a (known) settling velocity and a re-adjustment of the Lagrangian timescale to handle particle mass are simple adjustments that have worked well in the case of undisturbed surface-layer winds (Wilson, 2000). Thus presumably the weakest aspect of the trajectory modelling is the quality of the disturbed wind and turbulence fields provided by the RANS model. It is established (Wilson, 2004) that for modest angles of obliquity the wind model does a good job of diagnosing the field of the disturbed mean wind $\overline{u}, \overline{v}, \overline{w}$. However even after re-scaling to match the single-point sonic measurement, we have reason to fear there may be errors in the disturbed field of velocity variance as serious as 100% or worse; a similarly pessimistic assessment is warranted for the turbulent kinetic energy dissipation rate ϵ, and by implication for the effective Lagrangian timescale ($\propto \sigma_w^2/\epsilon$).

Yet despite those probable deficiencies of the provided fields of turbulence statistics, and despite inaccuracies inherent to experimental data, the

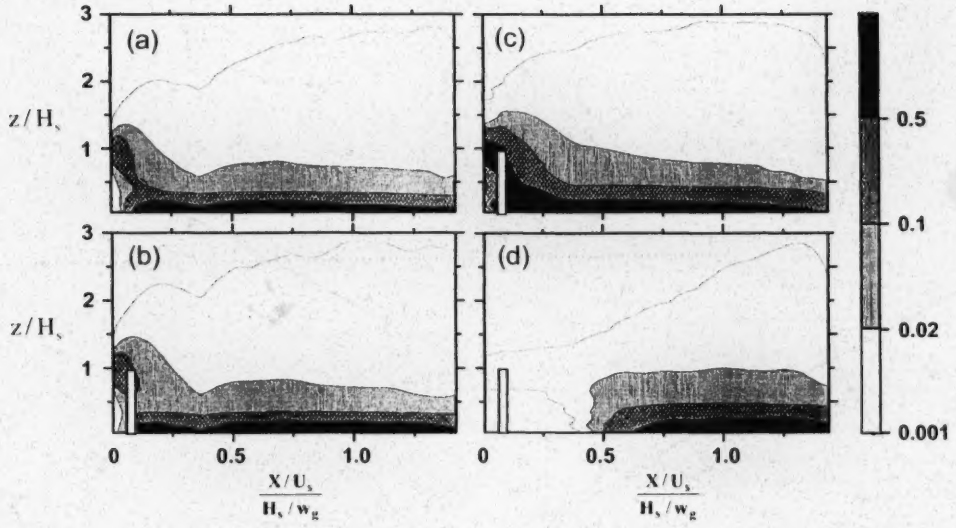

Figure 3.16: Normalized concentration (C/Q_0) fields of particles dispersed in various wind flows, in the experimental conditions of run P3: (a) undisturbed reference flow; (b) wind flow disturbed by the fence; (c) wind flow disturbed by the fence, but the mean vertical velocity is artificially set to zero; (d) wind flow disturbed by the fence, but the horizontal velocity is artificially forced to the undisturbed reference flow values at the same height. The white bar represents the windbreak.

model reproduces quite well the impact of the fence on the position of deposition peak, as well as the overall shape of the deposition swath; i.e. application of a Langevin-type particle trajectory model driven by a RANS-computed flow field has provided an adequate description of the fate of particles in the flow. Interestingly, the model seems to reproduce with about the same level of skill the dispersion of particles over uniform terrain, or about a fence. This complements the results of Leuzzi and Monti (1998), who showed that the LS model gave a useful description of (fluid element) trajectories in a wind field disturbed by buildings. Our results also suggest that the existing heuristic parametrizations for the crossing trajectory and continuity effects are useful, although setting $\chi = {}_L/_E = \text{constant}$ in this heterogeneous flow is at best a crude approximation. Therefore the present model can be regarded as satisfactory as long as it is the qualitative features of heavy particle dispersion that are of interest. In that respect, it is a valuable tool for the investigation of the dispersion pattern about an obstacle, and it can provide insight into the controlling variables.

In conclusion, a satisfactory theoretical framework for the dispersion of heavy particles in a turbulent flow remains to be provided; understanding of the underlying physics is still at an early stage, and the ad-hoc parameterizations proposed to mimic the observed behavior of heavy particles are crude and qualitative. In future it would be worthwhile to test such parameterizations against experimental data collected in better controlled conditions (eg. wind tunnel). This would reduce to a minimum the uncertainties relative to the experiment and to the modelling of the wind flow, and therefore allow to test more specifically the capabilities of the trajectory model.

Run	C^*_{uu0}	C^*_{vv0}	C^*_{ww}
P1	14.2	10.7	1.3
P2	16.9	17.5	1.5
P3	8.9	16.4	1.3
P4	5.0	5.4	1.4
P5	7.2	7.9	1.3
P6	9.6	12.9	1.5
L1	22.4	23.6	2.0
L2	12.0	13.1	2.2

Table 3.1: Values of C^*_{uu0}, C^*_{vv0} and C^*_{ww}, the normalized variances (in the limit $z/L_{mo} \rightarrow 0$) of the wind velocity in respectively the along-wind, the cross-wind and the vertical direction, calculated from the values of C_{uu0}, C_{vv0} and C_{ww} measured at $z = 4$ m according to Eqs. 3.20-3.22.

Run label	Fence			Source			micro-meteorology				
	Presence	heignt x length (m^2)	resistance coefficient K_r	type of source	Normal distance from fence (x/H)	height (z/H)	Release rate Qo ($\#.s^{-1}$) $x10^{-6}$ (tuned)	Mean wind direction θ (°)	Standard deviation of wind direction σ_θ (°)	Friction velocity U_* ($m\ s^{-1}$)	Monin-)bukhov length L_{mo} (m)	Roughness length Z_o (m)
P1	-	NA	NA	point	2.50	1.16	1.3	NA	28.3	0.33	-31.9	0.12
P2	-	NA	NA	point	2.50	1.16	1.8	NA	32.8	0.16	-19.2	0.22
P3	+	1x100	1.92	point	2.50	1.16	1.5	7.8	28.5	0.34	-18.5	0.06
P4	+	1x100	1.86	point	2.50	1.16	1.2	-20.1	14.7	0.46	-101.1	0.07
P5	+	1x100	1.73	point	2.50	1.16	Not Available	6.2	16.0	0.53	-82.9	0.04
P6	+	1x100	2.04	point	0.00	1.16	0.9	23.1	30.2	0.27	-17.7	0.11
L1	+	1x100	1.92	linear	8.00	1.12	5.0	12.4	20.1	0.17	-56.0	0.005
L2	+	1x100	1.72	linear	0.30	1.30	2.0	23.0	17.8	0.36	-353.0	0.007

Legend: NA Not applicable

Presence Run with (+) or without (-) fence

Table 3.2: Experimental conditions based on measurements recorded over the time duration of each run (20 to 30 min).

3.5 References

Aliseda, A., A. Cartellier, F. Hainaux, J. C. Lasheras, 2002: Effect of preferential concentration on the settling velocity of heavy particles in homogeneous isotropic turbulence. *J. Fluid Mech.*, **468**, 77-105.

Bink, N. J., 1996: The structure of the atmospheric surface layer subject to local advection. Ph.D. dissertation, Wageningen Agricultural University, 206 pp.

Bouvet, T., J. D. Wilson, 2005: An approximate analytical solution for the deposition of heavy particles released from an elevated line source. *Boundary-Layer Meteorol.*, in press.

Brusasca, G., G. Tinarelli, D. Anfossi, 1992: Particle model simulation of diffusion in low wind speed and stable conditions. *Atmos. environ*, **26**, 707-723.

Corrsin, S., 1963: Estimates of the relations between Eulerian and Lagrangian scales in large Reynolds number turbulence. *J. Atmos. Sci.*, **20**, 115-119.

Csanady, G. T., 1963: Turbulent diffusion of heavy particles in atmosphere. *J. Atmos. Sci.*, **20**, 201-208.

Du, S., 1997: Universality of the Lagrangian velocity structure function constant (C_0) across different kinds of turbulence. *Boundary-Layer Meteorol.*, **83**, 207-219.

Flesch, T. K., J. D. Wilson, 1992: A two-dimensional trajectory-simulation model for non-Gaussian, inhomogeneous turbulence within plant canopies. *Boundary-Layer Meteorol.*, **61**, 349-374.

Hage, K. D., 1961: On the dispersion of large particles from a 15-m source in the atmosphere. *J. Meteorol*, **18**, 534-539.

Hinze, J. O., 1975: Turbulence. 2nd. ed. McGraw-Hill, 790pp.

Jarosz, N., B. Loubet, B. Durand, A. McCartney, X. Foueillassar, L. Huber, 2003: Field measurements of airborne concentration and deposition rate of maize pollen. *Agric. For. Meteorol.*, **119**, 37-51.

Jarosz, N., B. Loubet, L. Huber, 2004: Modelling airborne concentration and deposition rate of maize pollen. *Atmos. Environ.*, **38**, 5555-5566.

Klein, E. K., X. Foueillassar, P. H. Gouyon, C. Laredo, 2003: Corn pollen dispersal: Quasi-mechanistic models and field experiments. *Ecol. monogr.*, **73**, 131-150.

Kroon, L.J.M., H.A.R. de Bruin, 1993: Atmosphere-vegetation interaction in local advection conditions: effect of lower boundary conditions. *Agric. For. Meteorol.*, **64**, 1-28.

Leuzzi, G., P. Monti, 1998: Particle Trajectory Simulation of Dispersion around a Building. *Atmos. Environ.*, **32**, 203-214.

Li, F. R., L. Y. Zhao, T. H. Hua Zhang, T. H. Zhang, Y. Shirato, 2004: Wind erosion and airborne dust deposition in farmland during spring in the Horqin Sandy Land of eastern Inner Mongolia, China. *Soil tillage res.*, **75**, 121 - 130.

Loubet, B., 2000: Modélisation du dépôt sec d'ammoniac atmosphérique à proximité des sources. Ph.D. dissertation, Université Paul Sabatier, pp 360. [Available online at http://tel.ccsd.cnrs.fr/documents/archives0/00/00/32/50/tel-00003250-00/tel-00003250.pdf]

Maxey, M. R., 1987: The Gravitational Settling of Aerosol Particles in Homogeneous Turbulence and Random Flow Fields. *J. Fluid Mech.*, **174**, 441-465.

Pinker, R. A., M. V. Herbert, 1967: Pressure loss associated with compressible flow through square-mesh wire gauzes. *J. Mechanical Engineering Sci.*, **9**, 11-23.

Raupach, M. R., 2002: Diffusion of heavy particles in a turbulent flow. *Geophys. Monogr., Environmental Mechanics: Water, Mass and Energy Tranfer in the Biosphere*, No. 129, Amer. Geophys. Union, 301-316.

Raupach, M. R., N. Woods, G. Dorr, J.F. Leys, H.A. Cleugh, 2001: The entrapment of particles by windbreaks, *Atmos. Environ.*, **35**, 3373-3383.

Reynolds, A. M., 2000: On the formulation of Lagrangian stochastic models for

heavy-particle trajectories. *J. Colloid Interface Sci.*, **232**, 260-268.

Saffman, P. G., 1962: An approximate calculation of the Lagrangian auto-correlation coefficient for stationary homogeneous turbulence. *Appl. Sci. Res., Sec. A*, **11**, 245-255.

Sato, Y., K. Yamamoto, 1987: Lagrangian measurement of fluid-particle motion in an isotropic turbulent field. *J. Fluid Mech.*, **175**, 183-199.

Sawford, B. L., F. M. Guest, 1991: Lagrangian statistical simulation of the turbulent motion of heavy particles. *Boundary-Layer Meteorol.*, **54**, 147-166.

Thomson, D. J., 1987: Criteria for the selection of stochastic models of particle trajectories in turbulent flows. *J. Fluid Mech.*, **180** , 529-556.

Walker, E. R., 1965: A particulate diffusion experiment. *J. Appl. Meteorol.*, **4**, 614-621.

Wang, L. P. and R. Maxey, 1993: Settling velocity and concentration distribution of heavy particles in homogeneous isotropic turbulence. *J. Fluid Mech.*, **256** , 27-68.

Wang, L. P., D. E. Stock, B. K. Lamb, 1988: On the relationship between Lagrangian and Eulerian Scales for Kraichnan's Gaussian random velocity field. Preprints, *8th Symposium on Turbulence and Diffusion*, San Diego, CA, Amer. Meteorol. Soc., 92-95.

Wells, M. R., 1982: The effects of crossing trajectories on the diffusion of particles in a turbulent fluid. *Ph.D. Thesis*, Washington State University.

Wells, M. R., and D. E. Stock, 1983: The effects of crossing trajectories on the dispersion of particles in a turbulent flow. *J. Fluid Mech.*, **136**, 31-62.

Wilson, J. D., 2000: Trajectory Models for Heavy Particles in Atmospheric Turbulence: Comparison with Observations. *J. Applied Meteorol.*, **39**, 1894-1912.

Wilson, J. D., 2004: Oblique, Stratified Winds about a Shelter Fence. Part II: Comparison of Measurements with Numerical Models. *J. Applied Meteorol.*, **43**, 1392-1409.

Woods, N., I. P. Craig, G. Dorr, B. Young, 2001: Spray drift of pesticides arising from aerial application in cotton. *J. Environ. Qual.*, **30**, 697 - 701.

Yang, C. Y., and U. Lei, 1998: The role of turbulent scales in the settling velocity of heavy particles in homogeneous isotropic turbulence. *J. Fluid Mech.*, **371**, 179-205.

Yudine, M. I., 1959: Physical considerations on heavy particle diffusion. *Adv. Geophys.*, **6**, 185-191.

Chapter 4

Filtering of windborne particles by a natural windbreak.

Paper submitted to 'Boundary-Layer Meteorology', a journal of Springer.

Authors: T. Bouvet, B. Loubet, J.D. Wilson and A. Tuzet[1]

[1] Authors are cited in the order of their respective contributions. The last three authors have made contributions in the writing and editing of the paper, and in supporting the experiment, either financially or technically.

Contents

4.1 Introduction 126

4.2 Particle entrapment by a shelterbelt: measured particle fluxes 129

4.2.1 Host flow 135

4.2.2 Particle concentrations and fluxes 135

4.3 Theoretical model of particle filtration 139

4.3.1 Resolved scales of motion 139

4.3.2 Modelling of a virtual source 141

4.3.3 Parameterization of deposition and rebound on leaves. 143

4.4 Results 145

4.4.1 Micrometeorology of the host flow 145

4.4.2 The wind flow about the shelter belt 146

4.4.3 Particle concentration and fluxes 150

4.4.4 Comparison with the treatment of entrapment by Raupach et al. (2001) 160

4.4.5 Particle dispersion patterns. 163

4.5 Conclusions 173

4.6 References 174

4.1 Introduction

A previous paper (Bouvet et al., 2006) provided new measurements of the deposition of heavy particles in disturbed micro-meteorological flow, specifically in the region of a thin artificial windbreak. Comparative simulations, using a first-order Lagrangian Stochastic (LS) trajectory model coupled with a RANS (Reynolds Averaged Navier Stokes) second-order closure wind & turbulence model, reproduced fairly satisfactorily the mean features of the deposition swath, i.e. its overall shape and horizontal extent, and the location and intensity of the deposition peak. Here we extend and complement that investigation, by addressing the case where the windbreak not only perturbs the mean streamlines of the airflow carrying the particles, but also heavily filters the passing airstream (the case of a thick, natural windbreak), with a focus on particle dispersion *inside* the hedge. The general context of the project is the use of windbreaks as a measure to control the drift and deposition of sizeable particles near ground, an environmental manipulation with a long history (and probably indeed *pre*-history) in relation to soil erosion[2](Dong et al., 2000), and which is familiar now in terms of highway fences to control snow drift (Shaw, 1988). A comprehensive understanding of windbreaks is demanded if we wish to engineer their use to, for instance, control the off-target drift of pesticides (Wood et al., 2001), minimize genetical pollution of the environment by genetically modified genes carried by wind-blown pollen (Klein et al., 2003), or reduce spread of pathogenic agents (Aylor, 1990; Waggoner and Taylor, 1958). Furthermore in these contexts it is clear that a good process-based under-

[2]Taking the global view, soil degradation caused by wind erosion has negatively impacted up to about 5 million km^2 of land surface, or over 40% of the total of degraded lands (Oldeman et al., 1991).

standing on micro-meteorological time-scales (circa 30 min) does not entirely suffice, for the role of extreme events (to take but one example, thunderstorm gust fronts), which almost by definition it is difficult to incorporate, may be a critical one.

Regarding the present state of our knowledge in regard to windbreaks as airstream 'filters', Raupach et al. (2001) provided an interesting and useful analysis for the restricted case of a 'thin windbreak', specifically where the ratio W/H of windbreak width (W, alongstream) to height H is so small that variation of windspeed across the windbreak can be neglected. These authors were able to relate the ratio $\kappa = \overline{c}_2/\overline{c}_1$ of particle mean concentrations immediately downwind ($\overline{c}_2$) and upwind ($\overline{c}_1$) of the fence to the optical porosity of the windbreak[3]: evidently if $V_b(z)$ is the bulk mean windspeed 'at' the thin windbreak (the 'bleed' velocity) then

$$D = V_b\,(\overline{c}_1 - \overline{c}_2) = V_b\,\overline{c}_1\,(1 - \kappa) \qquad (4.1)$$

is the local rate of filtration of particles by the windbreak (in Sec. 4.4.4 we will schematically apply this model to the present experiments, for which it proves ambiguous). This is a good beginning, but it remains to work out a useable treatment of natural (thick) hedges and shelterbelts, which are regarded (Maber, 1998) as more efficient particle traps than artificial thin windbreaks. As vegetation elements are obstacles to particles, a thick natural shelterbelt constitutes, in essence, a multiple impactor. There is an engineering literature regarding such types of filters, largely focused around specification of a bulk

[3]Throughout this paper subscripts 0, 1, 2 will respectively designate properties measured far upwind from the shelterbelt (0), along its upstream face (1), and along its downstream face (2).

filtering efficiency factor (eg. Shaw, 1978) as a function of the thickness of the filter, the trapping efficiency of a single trapping element, and the packing density of the filter. However these treatments do not carry over to the filtering of the wind by a natural windbreak, for the engineering models assume a steady and laminar (uniform) flow at entry to the filter. Grunert et al. (1984) provided recommendations on the structure of shelterbelt to maximize particle filtering, based on field and wind tunnel measurements. Although valuable, the results they presented are partial and essentially qualitative. In short, the subject we address has as yet received rather little attention (Ucar, 2001).

In Section (4.2) we describe bead dispersion measurements about a *natural thick shelterbelt*, focusing on vertical profiles of particle concentration and (streamwise) flux measured immediately upwind and downwind of a corn shelter belt, as well as the ground deposition flux within its boundaries; this study has many similarities with the work of Bouvet et al. (2006), indeed is identical as regards the experimental site and many aspects of the methodology. Section (4.3) will describe a numerical model of shelterbelt filtration, and since the model is an extension of that described by Bouvet et al. (viz., LS trajectory model coupled to a RANS wind model), we shall emphasize what is different from the earlier work, namely addition of an algorithm for deposition/rebound onto vegetation. In Section (4.4) we assess the capability of the RANS-LS model to mimic particle transport and deposition *inside* this natural windbreak, examine performance of the simpler 'thin windbreak' theory, and conclude by examining the (modelled) pattern of particle concentration and deposition across a wider region in proximity to the shelterbelt.

4.2 Particle entrapment by a shelterbelt: measured particle fluxes

As already noted, the present experiments were conducted in the same flat, even field of the earlier trials (Bouvet et al. 2006), amid short (10 cm) stubble, while the 'windbreak', which stretched in a direction normal to the prevailing wind, was composed of four rows of corn: the row-spacing was 0.8 m and the inter-plant spacing along the row was 0.15 m. At the time of the experiments the canopy height $H = 2.0 \pm 0.3$ m. As windbreak width $W \approx 3.2$ m, the aspect ratio $W/H \approx 1.6$, a value that (by design) should render inapplicable the thin-windbreak entrapment theory of Raupach et al. (2001). In what follows we define the origin of the streamwise axis ($x = 0$) to lie at the centre of the windbreak.

To provide information that would be needed by any theoretical description of deposition to leaves, measurements were made with a digitizer to determine the height distribution of leaf azimuth (Figure 4.1) and zenith (Figure 4.2) angles, as well as the 1-sided leaf area density profile $A = A(z)$ and its (height-varying) projections onto the horizontal and vertical planes (i.e. A_{xy}; and A_{xz}, A_{yz} respectively perpendicular and parallel to the hedge), shown on Figure 4.3. The Leaf Area Index (LAI) could be calculated from the digitizer data as $LAI = \int_0^H A(z)dz$. An independent estimate of the LAI was achieved from leaf dimensions that were measured manually, on plants chosen randomly in each of the four rows. The two results were very consistent ($LAI = 3.52$ versus $LAI = 3.54$).

During runs of 15 min duration, spherical glass beads of density 2500 kg m^{-3}, whose diameter ranged from 10 to 50 μm, were released from a 'line' source

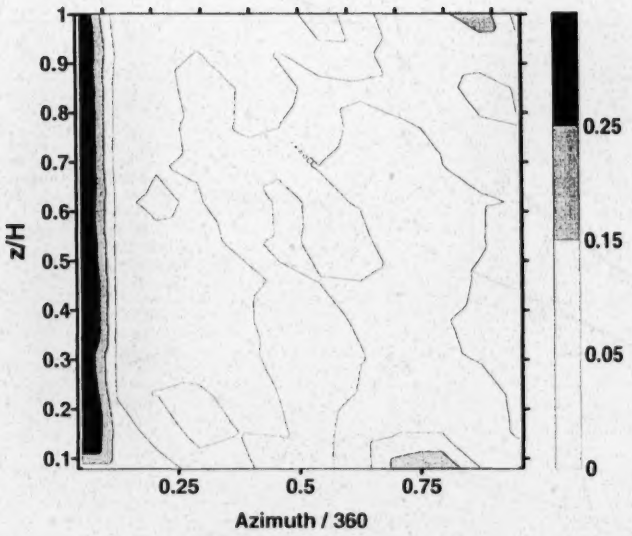

Figure 4.1: Vertical profile of the leaf azimuthal angle distribution. The color represents the proportion of leaves (measured by their area) across the azimuthal directions. Notes: 0, 0.5 and 1 represent the direction perpendicular to the windbreak, whereas 0.25 and 0.75 represent the parallel. The probability distribution is calculated separately in horizontal layers of width $\Delta z/H = 0.1$, and is discretized in 12 angle classes of width 30°. The probability p_i that a leaf's azimuth angle belongs to the range $\alpha_i \pm 15^\circ$ is calculated as $p_i = \int_{\alpha_i-15}^{\alpha_i+15} f_\alpha(x)\,dx$, where f_α is the probability density distribution of azimuthal angle in a horizontal layer.

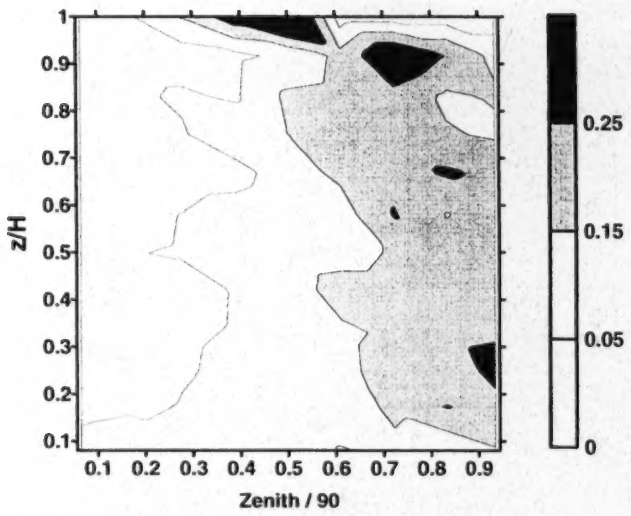

Figure 4.2: Vertical profile of the leaf zenith angle distribution. The color represents the proportion of leaves (measured by their area) across the zenithal directions, in a horizontal layer. Notes: 0 represents the horizontal, whereas 1 represents the vertical direction. The probability distribution is calculated separately in horizontal layers of width $\Delta z/H = 0.1$, and is discretized in 9 angle classes of width 10°. The probability p_i that a leaf's zenith angle belongs to the range $\theta_i \pm 5^\circ$ is calculated as $p_i = \int_{\theta_i-5}^{\theta_i+5} f_\theta(x)\,dx$, where f_θ is the probability density distribution of zenith angle in a horizontal layer.

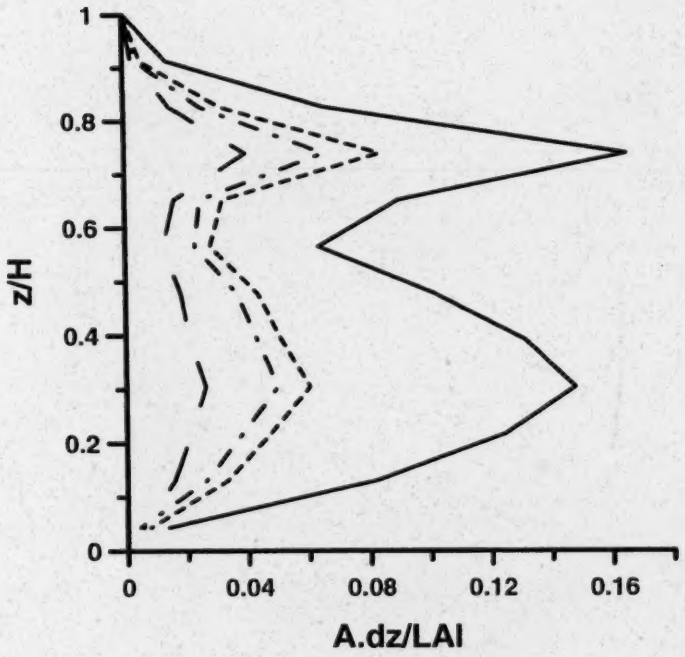

Figure 4.3: Vertical profile of vegetation leaf area density $A(z)$ (solid curve) and its projections $A_{xy}(z)$ (short dashed curve), $A_{xz}(z)$ (long dashed curve), $A_{yz}(z)$ (dashed dotted curve), normalized by the leaf area index (LAI). Notes: $LAI = 3.7$ and $dZ = 0.1H$; the upper peak reflects the leaves pointing upward, while the lower peak represents the dry leaves pointing downward near ground.

(see Bouvet et al., 2006) upwind from the windbreak. Five runs (labelled R1 to R5) were carried out, whose experimental conditions are detailed in Table 1. As detailed below, we measured the mean particle flux densities along the vertical faces of the corn belt, and the deposition flux to ground within the windbreak. The configuration of the experiments is sketched on Figures 4.4-4.5. In runs R1 and R2, the measurements were split into two particle size ranges: $10 - 25\mu$m and $30 - 50\mu$m, labelled respectively with suffices 'a' and 'b' (R1a, R1b, R2a, R2b).

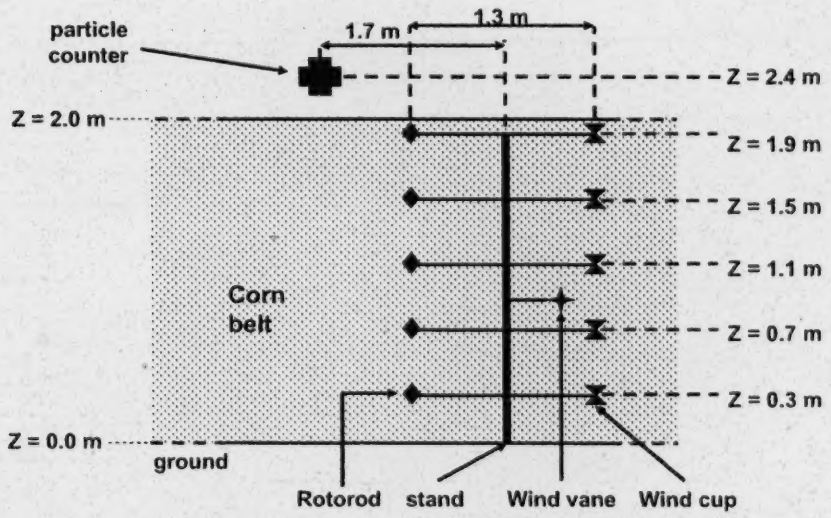

Figure 4.4: Side view of the experimental setup.
Note: the instruments measuring the micrometeorology of the host flow are not represented on this schematic.

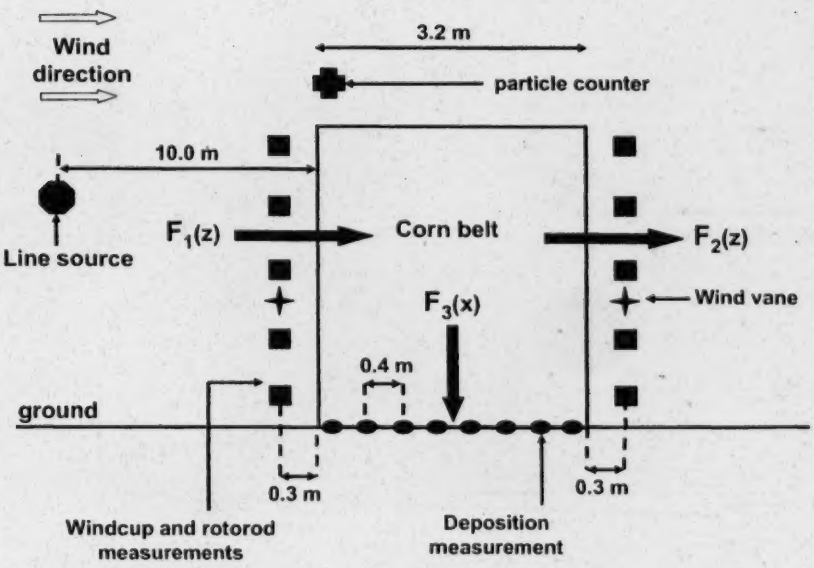

Figure 4.5: Frontal view of the experimental setup.
Note: the instruments measuring the micrometeorology of the host flow are not represented on this schematic.

4.2.1 Host flow

Cup wind speed ($s = \sqrt{u^2 + v^2}$) and temperature were measured at six levels (0.6, 1.1, 2.0, 3.0, 4.5, 6.0 m) in the undisturbed flow at a distance of 72.5 m upwind from the windbreak, where the Monin-Obukhov similarity theory applies (CIMEL CE155 cup anemometers, operating range $0.3 - 50.0\ \mathrm{m\,s^{-1}}$; shielded and ventilated Copper-Constantan thermocouples). In addition, the approaching wind direction (θ_0) was measured with a wind vane (MCB, Courbevoie, France).

From these reference measurements and using the Monin-Obukhov Similarity Theory (MOST), we derived estimates of the 15 min friction velocity (u_{*0}), Monin-Obukhov length (L_{mo}), heat flux (Q_h), roughness length (z_0) and mean ($\overline{\theta_0}$) and standard deviation ($\sigma_{\theta 0}$) of the wind direction. Independent estimates of u_{*0}, Q_h and L_{mo} were available from a 3-dimensional ultrasonic anemometer (type R3, Gill) placed 4 m above ground, upwind in the approach flow. Note that throughout this paper, the overbar denotes the time average over the duration of an experimental run.

4.2.2 Particle concentrations and fluxes

Figure 4.5 shows the three (of four) particle exchange fluxes (F_1, F_2, F_3) to/from the shelterbelt volume, that we were able to determine from the experimental runs. $F_1(z) = \overline{u}_1(z)\overline{c}_1(z)$ and $F_2(z) = \overline{u}_2(z)\overline{c}_2(z)$ estimate the horizontal fluxes of particles transported by the mean wind across (respectively) the upwind and downwind side-boundaries of the corn belt, and were evaluated (only) 0.3 m from the sides of the corn belt, at levels $z/H = (0.15,\ 0.35,\ 0.55,\ 0.75,\ 0.95)$. At these faces the mean horizontal velocity component $\overline{u}$, defined as the component perpendicular to the windbreak, was estimated from local cup windspeed

(s) and wind direction (θ) measurements performed with the same instruments as in the upwind flow, as

$$\overline{u} = \overline{s}\ \cos(\overline{\theta}) \tag{4.2}$$

Mean concentration $\overline{c}$ was measured using particle trapping instruments based on the design of Jarosz et al. (2003), and resembling the commercial instrument known as the 'rotorod'. As shown on Figure 4.6, these instruments consisted of spinning-arms which trapped particles whose inertia prohibited their escape from the swept-out volume. Each trap was composed of a 2 mm square-section brass rod, bent into a U-shape to give two vertical arms, these being 50 mm long and spaced a distance $D = 80$ mm apart. The arms were mounted to 1.2V (DC) electric motors so as to rotate at about $\Omega = 300$ rpm (note: Ω was determined specifically for each individual trap) and sample about 15 liters of air per minute. It so happened that for the specific conditions of the experiments, viz. particle release rate Q, position of detectors relative to source, 15 min integration (etc.), 15 L min^{-1} represented a sampling rate that yielded a statistically satisfactory count (small ratio of standard deviation to mean number of particles per unit area of the trapping surface), while avoiding saturation (ie. too many beads captured, with resulting ambiguity as to collection efficiency). Particles lying in the volume swept out by the rotating arms were deposited onto plastic strips (dimension $w \times h = 2 \times 50$ mm^2) attached to the arms, these strips being coated with a thin layer of silicon grease to ensure the intercepted particles remained stuck. After each run, the sample strips were detached and mounted on a microscope slide for visual counting with a light microscope. In order to alleviate the workload associated with the counting, bead counts were made on a sub-sample area (about 25%

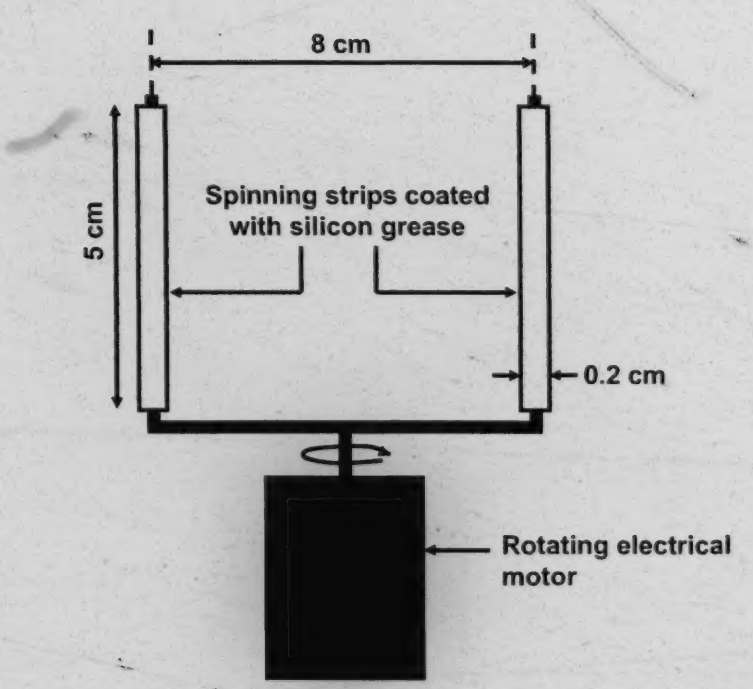

Figure 4.6: Schematic of a the particle trap instrument.

of the total surface of the strips) with the aid of a stencil scribed evenly with 10 slots of 0.45 mm width each and placed over the slide. Thereby we achieved a systematic sampling which allowed to account for heterogeneity of the bead distribution on the strips. The average particle concentration, $\overline{c}$ was determined as

$$\overline{c} = \frac{N_p}{2\,w\,h\,\Omega\,\pi\,D\,\Delta t\,E} \tag{4.3}$$

where N_p is the number of particles counted on the two arms of each trap, Δt is the duration of an experimental run and E_I is the efficiency of impaction of the particles on the arms, calculated according to Aylor's (1982) fit to May and Clifford's (1967) data for impaction on a cylinder:

$$E_I = \frac{0.86}{1 + 0.442\,S_t^{-1.967}} \tag{4.4}$$

where $S_t = |v|\tau_p/L$ is the Stokes' number of the particle to the impactor and L is the characteristic size of this impactor. With a rotational speed of 300 rpm, $27\% \leq E_I \leq 86\%$ when $10 \leq d_p \leq 50$, i.e. E_I is highly sensitive to the particle diameter. In runs R1 and R2, the optical count was split into a class of small beads ($10 \leq d_p \leq 25$ μm) and a class of large beads ($30 \leq d_p \leq 50$ μm). For the other runs, no size class distinction was attempted, and all beads with diameter $10 \leq d_p \leq 50$ μm were counted.

The deposition flux F_3 was sampled on ground at eight locations (spaced 0.4 m apart) across the corn belt, as indicated on Figure 4.4. As in the earlier trials (Bouvet et al., 2006) depositing particles were collected in electrolyte-filled Petri dishes and enumerated by a liquid phase spectral counter (Multisizer Coulter Counter®, Beckman Coulter Inc., 4 μm diameter-resolution). Unfortunately these electrolyte samples proved to be heavily polluted by alien

particles in the range of diameters $d_p \leq 20\mu$m, and we were able to extract a meaningful deposition rate only for runs R1, R2 for the aggregate size class $30 \leq d_p \leq 50\mu$m. The deposited samples did however prove useful in another role, namely they allowed us to estimate (by interpolation) the particle size distribution at heights intermediate between ground and the top of the windbreak, where we operated an FM-100 particle spectrometer (Droplet Measurement Technologies, Inc., Boulder, CO, USA).

4.3 Theoretical model of particle filtration

4.3.1 Resolved scales of motion

For comparison with the experiments, theoretical particle dispersion statistics (concentration field, flux field) were derived from an ensemble of computed particle trajectories, using the LS model described by Bouvet et al. (2006) to which it was necessary to add an algorithm parameterizing capture by leaves (see below). The LS model was driven by a synthetic wind flow computed specifically for each experimental run, over a domain having $266H$ streamwise and $55H$ vertical extent.

It would be tedious and unnecessary to elaborate on the wind model, described and tested in some detail by Wilson et al. (2001) and Wilson(2004), and which is based on the second-order closure of Rao et al. (1974). Suffice it to say that for each of the runs documented in Table (1), the wind model provided the spatial field, throughout the specified domain, of all velocity moments up to the second order, based on a prescribed upstream flow reproducing the measured micrometeorological statistics (u_*, L_{mo}, z_0, $\overline{\theta}$). The profile of the effective drag coefficient $c_D(z)$ was tuned for a best match with

the measured profiles of the mean wind $\overline{u}_1(z), \overline{u}_2(z)$ at the entry and exit faces of the shelterbelt. The impact of $c_D(z)$ on the flow model is through localized sinks for mean horizontal momentum and velocity variance, symbolically

$$\begin{aligned} \frac{\partial \overline{u}}{\partial t} &\propto -c_{\mathrm{d}}(z)\, A_{yz}(x,z)\, \overline{u}\, \sqrt{\overline{u}^2 + \overline{v}^2} \\ \frac{\partial \sigma_u^2}{\partial t} &\propto -c_{\mathrm{d}}(z)\, A_{yz}(x,z)\, \overline{u}\, \sigma_u^2 \end{aligned} \tag{4.5}$$

where within the shelter $A_{yz}(x,z) \equiv A_{yz}(z)$, the leaf area density profile, while outside the shelter $A_{yz}(x,z) = 0$ (for justification of eqns 4.5 see Wilson, 2004). By adjusting $c_{\mathrm{d}}(z)$ we were able to achieve a reasonably close match between the modelled and the measured horizontal velocity components $\overline{u}$, $\overline{v}$ at heights $z/H = (0.15, 0.35, 0.55, 0.75, 0.95)$ immediately upwind and downwind of the belt.

Particle trajectories were computed using the simplified approach (Wilson, 2000) wherein (in essence) a gravitational settling velocity w_g is merely superposed on what would (otherwise) be the trajectory of a fluid element. Thus particle inertia is not rigorously (or even explicitly) represented, and particle velocity variance is assumed to equal fluid velocity variance. Because trajectories are terminated on ground, Wilson called this approach (which had already been widely used) the 'Settling Sticky Fluid Element' method. For small enough values of the ratio τ_p/T_L of the particle's inertial (ie. Stokesian) time-constant to the integral scale of the driving turbulence, these approximations were proven to be acceptable, and without detailed investigation we assumed this restriction was met throughout our experimental flows.

The carrier fluid velocity was calculated using Thomson's (1987) well-mixed multi-dimensional algorithm for Gaussian inhomogeneous turbulence, with an adjustment to the effective Lagrangian decorrelation timescale to ac-

count for the crossing trajectory effect (Csanady, 1963). Velocity statistics required by the LS model (thus, provided by the RANS wind model) were the mean velocities, the Reynolds stress tensor τ_{ij}, and the turbulent kinetic energy dissipation rate ϵ. As an illustration, Figure 4.7 shows a side view of trajectories simulated by the LS model in the meteorological conditions of run R5.

4.3.2 Modelling of a virtual source

The observant reader will notice on Figure 4.7 that particles commenced their (imaginary) journeys from discrete locations slightly upwind from the hedge. Because this study focuses on the ability of the combined RANS/LS model to reproduce heavy particle dispersion *inside* the shelter belt, the actual (single) crosswind line source (at $z/H = 0.82$ or 0.95; $x/W = -3.6$) was represented in the computation by ten 'virtual' crosswind line sources at heights $z/H = (0.05,\ 0.15,\ 0.25,\ 0.35,\ 0.45,\ 0.55,\ 0.65,\ 0.75,\ 0.85,\ 0.95)$ and lying at $x/W = -0.60$. The intensity of those sources was determined so as to *reproduce the measured particle concentration profile upwind of the hedge*, according to

$$Q_j = \overline{c}_j \, dZ_j \, \overline{u}_j \tag{4.6}$$

Here Q_j is the point source intensity at level j, $\overline{u}_j$ is the component of the mean horizontal velocity perpendicular to the hedge (as computed by the RANS model), and dZ_j is the height of the bin over which the concentration $\overline{c}_j$ is averaged (note: in reality the concentration was only measured at $z/H = (0.15,\ 0.35,\ 0.55,\ 0.75,\ 0.95)$, and we interpolated linearly to intermediate levels). As in truth the physical particles were released further upwind than $x/W = -0.6$, the particle size distribution had time to evolve so as

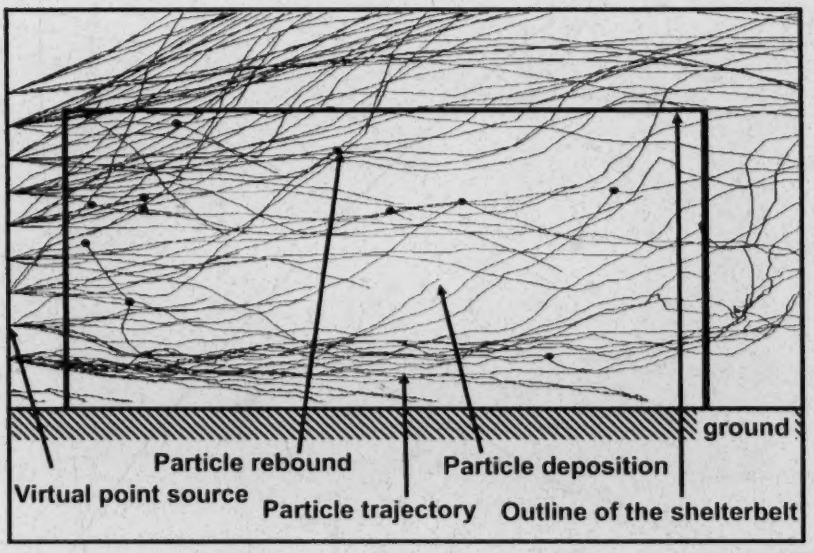

Figure 4.7: Side view of numerically simulated particle trajectories across the shelterbelt. Note: the shelterbelt is 2 m high and 3.2 m wide.

to become non-uniform along the vertical, by the time particles reached the virtual (computational) source plane. The particle size distribution was estimated at each level of the virtual source by linear interpolation (with respect to distance) between the distribution observed at the ground via the deposition measurements and the distribution measured at $z/H = 1.2$ with the FM-100 instrument.

4.3.3 Parameterization of deposition and rebound on leaves.

Along its trajectory across the corn belt a particle likely would have encountered stems and leaves on which it might impinge. Probability of impingement depends on the probability that the particle will 'encounter' a vegetation element[4], and (multiplicatively) on the probability of capture subsequent to (or conditional on) encounter. Following the approach of Wilson (2000) and Aylor and Flesch (2001), we expressed the probability of particle impingement P_I on vegetation over a time step dt as

$$P_\mathrm{I} = (v_x\, A_{yz}\, E_{\mathrm{I,yz}} \;+\; v_y\, A_{xz}\, E_{\mathrm{I,xz}} \;+\; v_z\, A_{xy}\, E_{\mathrm{I,xy}})\, dt \qquad (4.7)$$

where v_i is the particle velocity (which, note, we regard as 'resolved' in the modelling, whereas the motion carrying the particle onto or around an impediment such as a leaf remains unresolved), E_I is the efficiency of interception (by impaction or sedimentation), and A is the vegetation area density (m^{-1}). The subscripts or superscripts x, y and z denote respectively the direction perpendicular to the hedge, parallel to the hedge and the vertical; and the double subscript notation xy refers to the orientation of a surface whose normal is vertical, i.e. a horizontal surface, (etc). We assumed that the efficiency

[4]An 'encounter' is defined as the event of a trajectory segment, computed in the 'resolved flow' as if vegetation were not present, crossing a leaf or stem.

of interception of particles settling under gravity was total ($E_{\mathrm{l,xy}} = 1$), and estimated the efficiency of impaction $E_{\mathrm{l,xz}}, E_{\mathrm{l,yz}}$ according to Eq. 4.4 where $S_l = |v|\tau_p / L_{\mathrm{v}}$ is the Stokes' number of the particle to the vegetation element and L_{v} is the characteristic size of a vegetation element. We defined the latter as the width of a corn leaf projected on the plane perpendicular to the particle's trajectory.

After impacting a surface, a particle may rebound. As Dahneke (1971, 1975) describes in his theory analyzing the energy balance of particles impinging and rebounding on a surface, particles lose energy from adhesion forces and by plastic deformation of the particle and/or the surface. Rebound will occur if the kinetic energy at impact is large enough to overcome the loss of energy. Paw U (1983) showed that the theory of Dahneke (1975) adequately describes experiments with natural and artificial particles (glass beads, lycopodium spores and ragweed pollen of diameter $20 - 40$ μm) impinging on natural and artificial surfaces (Tulip poplar leaves, American elm leaves or glass). According to those experimental results, particles rebound if the velocity component perpendicular to the impinging surface before impact is above a 'critical rebound velocity'. Interestingly, Paw U (1983) showed that this critical velocity is approximately constant for each particle type. For glass beads, he reported a critical velocity

$$V_c = 0.28 \text{ m s}^{-1} \tag{4.8}$$

which we therefore invoked in the trajectory model. The ratio of the rebound velocity V_r to the impaction velocity V_i (known as the coefficient of restitution, e) also depends on the impaction velocity; Obviously, $V_r/V_i = 0$ as long as $V_i \leq V_c$; as V_i passes and exceeds V_c, V_r/V_i soars and levels off quickly. The

plateau value proves to be very similar across surface types, and on average $e = 0.82$ for glass beads. It is assumed in our model that

$$V_r = 0.82 V_i \tag{4.9}$$

when $V_i > V_c$. According to Xu and Willeke (1993), both the critical rebound velocity and the velocity of rebound depend strongly on the angle of incidence of the particle to the surface. In the experiment of Paw U (1983), the impactor used was a cylinder of glass wrapped with various types of leaves, so those results pertain to particles impinging and rebounding on surfaces with various angles of incidence, as in the case of our experiment. Therefore we assumed Paw U's results are directly applicable to our situation. Note that the parameters characterizing the vegetation which are involved in the equations describing deposition and rebound (Eqs. 4.7-4.9) were measured experimentally as mentioned in Section 4.2: the corn belt was characterized by digitalization measurements characterizing the architecture of vegetation along a vertical profile (split into 13 vertical levels along the height of the hedge), in terms of plant area density (m^{-1}) projected onto each of the three directions and leaf orientation distribution (azimuth and zenith). The dimensions of the leaves (measured manually) were used in the calculation of the Stokes number S_t in Eq. 4.4.

4.4 Results

4.4.1 Micrometeorology of the host flow

The micrometeorological conditions computed from the sonic anemometer measurements and the temperature and wind velocity profiles are consistent (See Table 4.2). The estimates of u_{*0} and Q_{h0} retained in the modelling are

averages of the 'sonic' and 'profile' values, and were used to infer L_{mo}. The roughness length z_0 was determined for a best fit between the observed mean velocity profile in the reference flow and a MOST parameterization of it based on the values of u_{*0} and L_{mo}, determined as mentioned above. The mean and standard deviation of the wind direction in the reference flow were given by the wind vane measurements. All the micrometeorological statistics are presented in Table 4.1 for each run.

4.4.2 The wind flow about the shelter belt

As an illustration, Figure 4.8 presents the disturbance generated by the hedge (relative to the undisturbed values at the same vertical level upwind in the reference flow) in the mean horizontal wind field (panel a) and in the turbulent kinetic energy (TKE, panel b), as computed by the RANS model in the conditions of run R3. The reader will notice a significant decrease in the mean wind velocity in the region ($-3 < x/W < 4,\ z/H \leq 1$): mean wind reduction exceeds 50% within the shelterbelt and in its immediate wake. On the other hand the mean wind accelerates over the top of the windbreak; the accelerated zone stretches fairly high (over $z/H = 3$), but only in the region $0 < x/W < 1.5,\ 1.2 < Z/H < 2.2$ does the speed increase exceed 10%. The turbulent kinetic energy field is also dramatically disturbed by the presence of the hedge. It is reduced by more than 50% in the lower downwind region of the shelter belt, and this reduction extends into the wake to about $x/W = 1.4$. One observes also a large increase of the TKE (by more than 50%) along the upwind face and the top face of the hedge, where the wind shear is strongest. This enhanced TKE region extends and spreads downwind; it curves down to ground shortly after passing the shelter belt.

Run label	Source height (normalized by the Hedge's height)	micro-meteorology			
		Mean wind direction θ_0 (°)	Standard deviation of wind direction σ_θ (°)	Friction velocity u_{*0} (m s^{-1})	Monin-Obukhov length L_{mo} (m)
R1	0.91	-33.5	9.6	0.27	-19.8
R2	0.91	-25.0	16.8	0.14	-1.8
R3	0.91	-49.5	16.0	0.29	-101.0
R4	0.91	22.2	25.6	0.34	-28.8
R5	1.06	-38.5	10.0	0.22	-74.2

Table 4.1: Conditions of the experimental runs.

Run label	Sonic anemometer		Mean temperature and horizontal velocity profile	
	u_{*0}	Q_{h0}	u_{*0}	Q_{h0}
R1	0.29	85.0	0.25	82.3
R2	0.12	123.2	0.16	139.7
R3	NA	NA	0.29	20.4
R4	0.35	132.3	0.34	97.5
R5	0.23	14.3	0.22	11.6

Table 4.2: Micrometeorological conditions computed from the sonic anemometer measurements and the temperature and wind velocity profiles

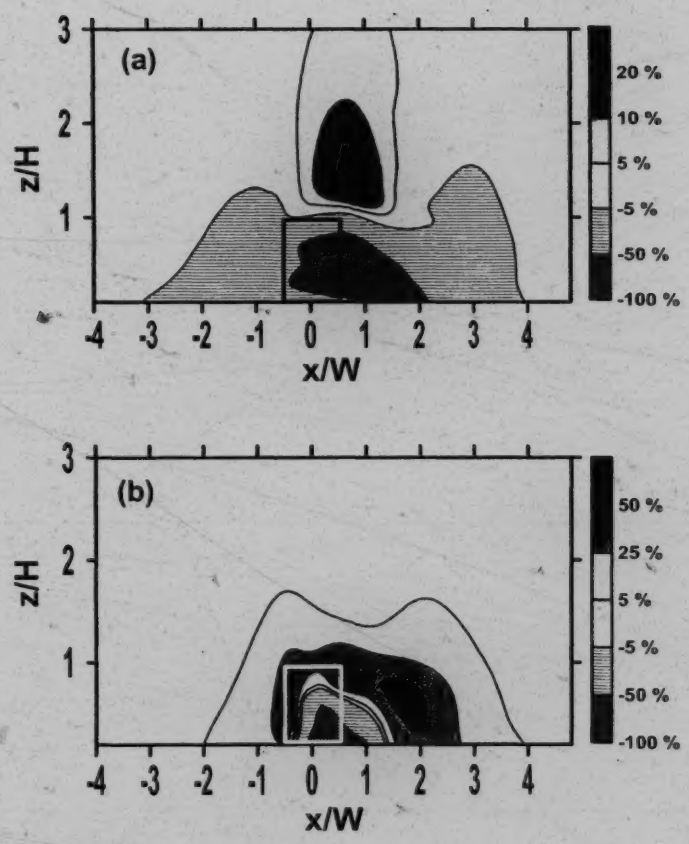

Figure 4.8: Disturbance in the mean horizontal velocity (Panel a) and in the turbulent kinetic energy (Panel b), in percent relative to the undisturbed value upwind. The rectangle shows the outline of the corn belt of height H and width W. The meteorological conditions are those of run R3.

Figure 4.9 shows the consistency between the modelled and the observed mean horizontal velocity perpendicular to the windbreak at heights z/H = (0.15, 0.35, 0.55, 0.75, 0.95) along the upwind profile (x/W=-0.60) and the downwind profile (x/W=0.60), for run R5. The close match, achieved by adjusting $C_d(z)$, suggests the mean wind speed is satisfactorily reproduced inside the hedge; unfortunately we have no measurements to check the model fields of the velocity variances, but these should have been qualitatively reasonable, since the inflow profiles $\overline{u'^2}(z)$ (etc.) of the RANS model are equilibrium (1d) solutions held to lower and upper boundary values from $\overline{u'^2}/u_{*0}^2 = \phi_{uu}(z/L_{mo})$, the Monin-Obukhov universal relationship.

4.4.3 Particle concentration and fluxes

The concentration vertical profiles at entry and exit of the corn belt are presented in Figure 4.10. The standard deviation of the observed concentration relates to the deviation in the particle count of the 20 areas sampled on the particle trapping instrument's strips. In all the runs presented, the numerically simulated concentration profile at entry of the hedge matches perfectly the measurements, as it was a constraint of the model - we remind the reader that we adjusted the source profile intensity so as to reproduce the measured concentration profile at entry of the corn belt.

The upwind experimental concentration profiles have rather different shapes from one run to the next, and this may be surprising since from a habitual context of *fluid element or tracer dispersion*, we may tend to be accustomed to expect 'form similarity' of concentration fields (for fixed source configuration). However it is to be recalled that in particle dispersion we have an expanded set of governing parameters, and so form similarity need not and

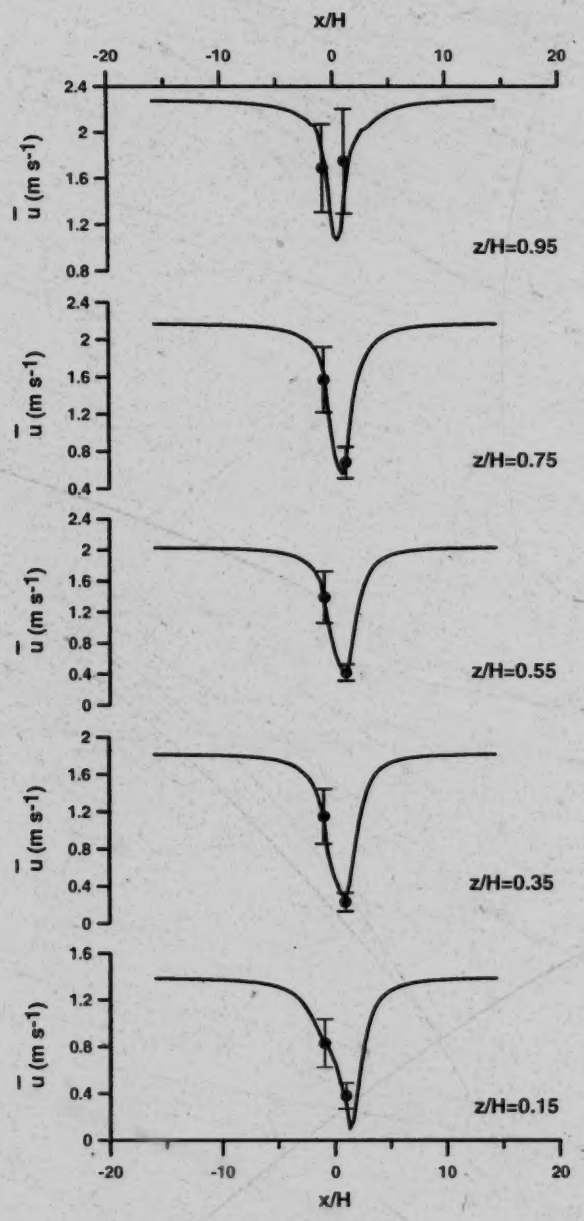

Figure 4.9: Mean horizontal velocity perpendicular to the hedge, computed by the RANS model (curves) or measured experimentally (dots) during run R5, at five vertical levels: z/H=0.15, 0.35, 0.55, 0.75, 0.95.

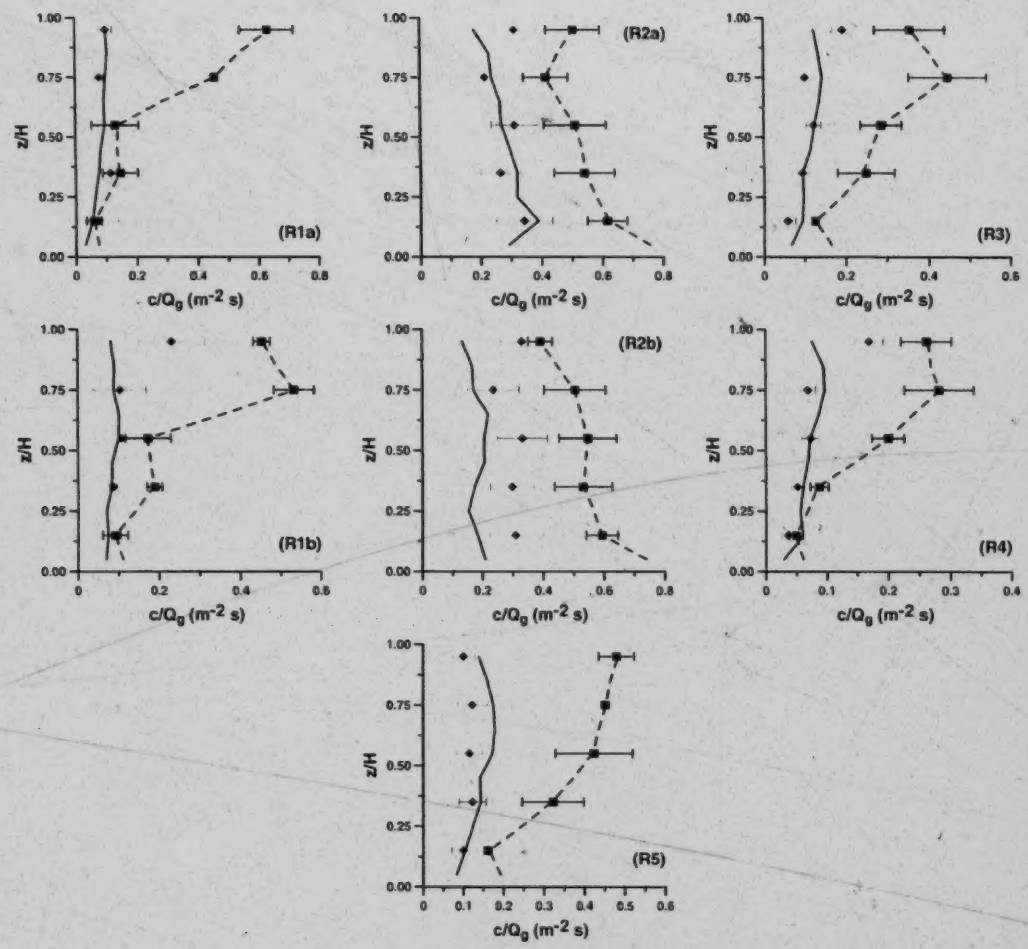

Figure 4.10: Vertical profiles of concentration (normalized by the source intensity Q_g) measured upwind at x/W =-0.6 (squares) and downwind at x/W=0.6 (diamonds). The corresponding numerical simulation results are shown with dashed (upwind) and solid (downwind) curves. Note that the virtual source, placed at x/W =-0.6, was adjusted to fit the upwind concentration profile.

indeed should not be expected. Examining this matter in more detail, we note Runs R1b, R3 and R4 display the same features, with upwind concentration peaking slightly below the source height ($H_S/H = 0.82$m), and falling sharply with decreasing height below the peak. In those three runs, the far upstream horizontal wind component perpendicular to the hedge was fairly strong ($\overline{u}_{0H} = 2.74,\ 2.73,\ 4.26$ m s^{-1} for runs R1b, R3 and R4 respectively). Therefore the particle plume had little time to settle under gravity and to spread in the vertical before encountering the face of the shelter belt. This explains why a concentration peak can be observed close to the level of the source. On the other hand in runs R1a and R5 one does not observe such a peak, although the wind conditions ($\overline{u}_{0H} = 2.74,\ 2.13$ m s^{-1} for runs R1a and R5 respectively) were similar to those of runs R1b, R3 and R4. How can this be explained?

The results of run R1a are to be interpreted by considering the smaller size of the particles ($10 \leq d_p \leq 25\mu$m) relative to those of runs R1b, R3 and R4 for which particles were up to 50 μm in diameter. In effect, the positive mean vertical velocity upwind of the hedge overcomes the gravitational settling velocity of small particles. Neglecting velocity fluctuations, the average vertical displacement of a particle traveling from the source (at $x = x_S$) to the vertical plane ($x = x_1$) just upwind from the windbreak where concentrations were measured is approximated by an integral

$$\Delta z = \int_{x_S}^{x_1} \frac{\overline{w}(x,z) + w_g}{\overline{u}(x,z)}\, dx \qquad (4.10)$$

along the particle path. Evaluating this expression from a computation of the RANS-LS model in the conditions of run R1a, we estimate that a 20 μm diameter particle would rise by 0.39 m above the source height $H_s/H = 0.82$

by the time it reaches the plane of the upwind measurement profile at $x = x_1$. In consequence the plume is lifted above the highest level of measurement ($z/H = 0.95$). This explains why one does not observe a concentration peak in the concentration upwind profile of run R1a. In R5 the source was placed higher than in the other runs ($H_s/H = 0.95$) and the plume mass centerline was too high for a concentration peak to be identified in the measurements. Finally, in R2a and R2b concentration was fairly homogeneous on the inflow profile, a peculiarity which should be associated to the significantly lighter winds than in the other runs ($\overline{u}_{0H} = 1.58$ m s^{-1}; $u_\star = 0.14$ m s^{-1}). Slower winds imply that particle have a longer time to disperse over a given distance. On the other hand, slow winds result in smaller particle diffusivity. In the far field limit, and assuming a homogeneous velocity field, the variance in particle location in the vertical is, after a traveling time t

$$\sigma_z^2(t) = 2\sigma_w^2 T_L t \tag{4.11}$$

where T_L is the Lagrangian integral time scale and σ_w^2 is the vertical velocity variance. $\sigma_w^2 \propto u_\star^2$ whereas $T_L \propto 1/u_\star$ and $t \propto 1/u_\star$. As a result, the variance σ_z^2 does not depend on $u_\star$ according to Eq. 4.11. If turbulence is left aside, a plume of particle of various sizes still spreads in the vertical. In effect gravitational settling is stronger for larger particles. Because of this differential gravitational settling, particles spread with increasing traveling time. With lighter wind conditions in experiment R2, particles travel longer before reaching the hedge, and therefore spread more than in the other runs. According to Eq. 4.10, in the conditions of R2 a 10 μm particle (subject to gravitational settling and the mean flow only, i.e. turbulent fluctuations are artificially discarded) ascends by 0.24 m by the time it reaches the windbreak, whereas a

50 μm particle drops by 0.84 m. This means that the differential gravitational settling accounts for 1.08 m of the vertical spread.

Comparing the numerically simulated downwind profiles of concentration with measurements allows to test the ability of the model to reproduce particle filtration by vegetation. The match between observations and numerical simulations is very satisfactory for run R1a. In runs R1b, R2a, R3 and R4, the overall magnitude of concentration across the downwind profile is well reproduced. However, concentration tends to be underestimated in the upper part by the hedge's top. This trend is particularly marked in run R1b and R4. Because the plants' heights were very heterogeneous, going from $z/H = 0.85$ to $z/H = 1.15$, we think that the values of leaf area density in the upper part of the hedge (calculated from a sample measurement of 15 plants) were not reliable, thus explaining the discrepancy.

In run R2b the numerical simulation significantly underestimates the bead concentration over the whole profile. The reader should be aware that the impaction efficiency is highly variable in the range of particle size, velocity and leaf dimension applicable to this experiment. Should the velocity of a 30 μm particle heading towards a 4 cm wide leaf be overestimated by 20% (for example, $u = 0.6$ m s^{-1} instead of 0.5 m s^{-1}, the approximate velocity at the center of the hedge in run R2), the impaction efficiency E_I of the particle would be overestimated by over 42%. The wind flow is a component of the modelling which is subject to inaccuracy. Even though we have evidence that the mean horizontal velocity was well reproduced by the RANS model, one should keep in mind that the observations displayed a large variability (See Figure 4.9). In addition, the RANS model is known to be poorly skilled at

computing the disturbance to velocity variances (Wilson, 2004); this certainly would affect the accuracy of the instantaneous particle velocities calculated by the LS model. There are also uncertainties pertaining to the size distribution of the particles released at the 'virtual sources' in the modelling, which is linearly interpolated (with distance) between the distribution measured at ground and at the top of the shelterbelt. Figure 4.11 compares the actual size distribution, at $x/W = -0.6$ (plane of the virtual source) and $z/H = 0.6$, with the distribution derived from the linear interpolation method. The results shown are obtained by numerical simulation in the meteorological conditions of run R2, with a line source placed at $x/W = -3.5$, $z/H = 0.82$, which releases particles of size uniformly distributed in the range $10 - 50$ μm. The graph shows that particles smaller than 33 μm are under-represented with the linear interpolation method (and correlatively particles larger than 33 μm are over-represented), with an error lying within 34%.. In conditions pertaining to R2 ($u \sim 0.5$ m s^{-1}, 4 cm wide leaves), overestimating the size of a 30 μm particle by 5 μm results in an error of 80% of the impaction efficiency on the leaves.

Given the sensitivity of impaction to the wind flow and particle diameter, discrepancies between the simulations and the observations are to be expected. It is encouraging that the magnitude of the 'jump' (across the hedge) in the concentration profile is well captured, with errors (relative to the concentration upwind from the windbreak) no larger than 24%, except in the upper region where the input values of the area-density $A(z)$ are dubious. No systematic bias of the computational description is observed throughout this comparison, and we conclude that the LS model reproduces the concentration profiles reasonably satisfactorily, bearing in mind the questionable level of accuracy of

the velocity statistics and of the particle size distribution provided to it.

The rate of deposition to ground under the 'hedge' was measured in runs R1b and R2b. We compare on Figure 4.12 the numerically simulated deposition flux integrated over the width of the corn belt against observations. The match is accurate within 14% and 35% respectively in runs R1b and R2b. In parallel is presented the observed and modelled horizontal particle flux carried by the mean wind flow across the vertical faces of the hedge (integrated over the height of the hedge), in order to show how they compare with ground deposition in term of magnitude. This horizontal flux is calculated as

$$F = \int_0^H \overline{u}(z)\,\overline{c}(z)dz \tag{4.12}$$

where $\overline{u}$ is the mean horizontal velocity perpendicular to the hedge, and $\overline{c}$ is the average concentration. The mismatch between numerical and experimental results of the horizontal flux upwind is fairly small (8% in run R1b and 15% in run R2b). Effectively, the discrepancy in the upwind flux stems from inaccuracies in the mean horizontal wind only, since concentration is forced to reproduce the observations along the upwind vertical profile. Errors of about 35% occur at the downwind profile; larger discrepancies (than upwind) are not surprising as they result from inaccuracies in both the input horizontal wind velocity and the modelling of particle dispersion. Yet again, those discrepancies seem tolerable in view of the suspect accuracy of the velocity statistics and particle size distribution provided to the LS model and the high sensitivity of the model's response to input errors. The deposition flux on ground turns out to represent only a small portion (5% and 12% in runs R1b and R2b respectively) of the horizontal particle flux (carried by the mean wind) entering the corn belt. This means that a large fraction of the incoming particles deposit

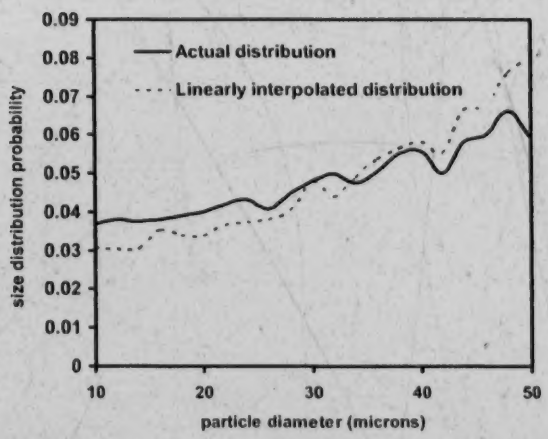

Figure 4.11: Actual particle size distribution at $z/H = 0.6$, $x/W = -0.6$ (virtual source plane) versus distribution derived from linear interpolation between the distribution at the top and the bottom of the shelterbelt. The results are numerically simulated, for the case that a line source at $z/H = 0.82$, $x/W = -3.5$ releases particles whose sizes are uniformly distributed in the range $10 - 50$ μm. The probability distributions shown are discretized in 21 diameter classes d_i of width 2 μm, in the range $10 - 50$ μm. The probability p_i that a particle belongs to the range $d_i \pm 1$ μm is calculated as $p_i = \int_{d_i-1}^{d_i+1} f_d(x)\,dx$, where f_d is the probability density function for diameter.

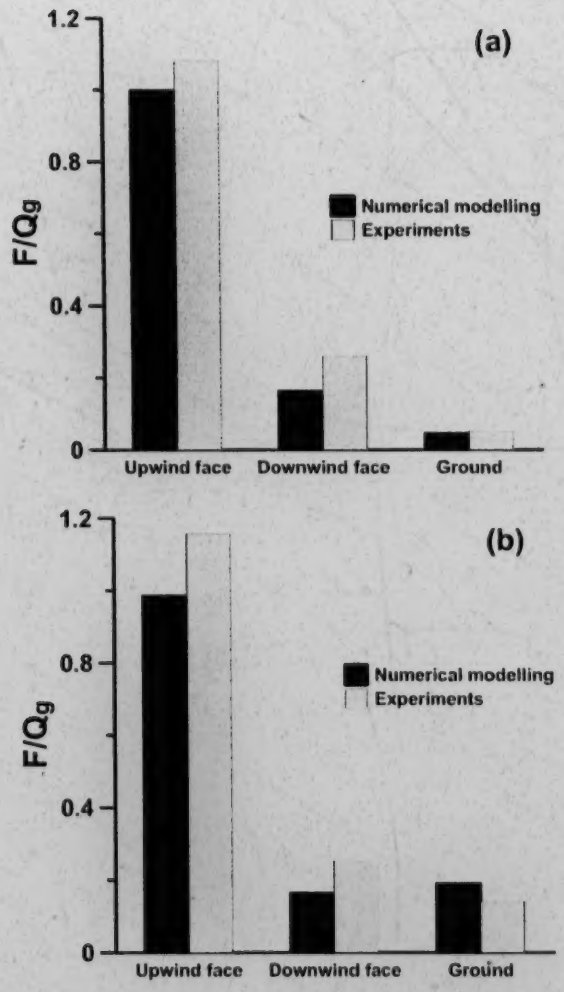

Figure 4.12: Normalized particle fluxes F/Q_g across the upwind face of the hedge, across the downwind face or onto ground for run R1b (panel a) and R2b (panel b). Comparison between experimental results and numerical simulations.

on the vegetation and/or exit the corn belt across the upper surface of the hedge.

4.4.4 Comparison with the treatment of entrapment by Raupach et al. (2001)

The theory developed by Raupach et al. (2001) is beautifully simple, fixing the transmittance of the windbreak κ in terms of an economical set of parameters, viz.

$$\kappa = \frac{\overline{c}_2}{\overline{c}_1} \approx \eta^{m E_1} \tag{4.13}$$

where (as earlier) $\overline{c}_1$ and $\overline{c}_2$ are respectively the mean particle concentrations immediately upwind and downwind from a windbreak and the optical porosity η is related to the projection of the area density A (m^{-1}) onto a vertical plane parallel to the shelterbelt,

$$\eta = e^{-AW} \tag{4.14}$$

As earlier E_1 is the efficiency of impaction on vegetation elements, while $m = L/W$, the 'meandering factor', is the ratio of the pathlength (L) of a particle's (meandering) trajectory across the shelterbelt, to the straightline width (W).

Because the Raupach et al. theory is enticing for its simplicity, it is worthwhile to investigate whether it yields acceptable results for the present experiments despite its (strong) assumptions, viz. neglect of deposition under gravitational settling to ground, neglect of particle flux across the upper boundary of the windbreak, and constant horizontal velocity '$V_b(z)$' across the width of the shelterbelt. Therefore, we computed the transmittance at $z/H = 0.6$ according to Raupach et al. for comparison with the corresponding numerical prediction of the far more intricate model described above. To this end we estimated E_1, m and η following Raupach et al. (their Section

2.1 for E_1, Section 2.2 for η and Appendix for m) from the canopy vegetation measurements and the velocity statistics computed by the wind flow model, for $z/H = 0.6$ at the center of the shelterbelt. Resulting values ($E_1 = 0.85$, $m = 1.12$) yielded $\kappa = 0.07$. The meteorological conditions of the numerical run where those of R3 (near-neutral stratification), and the natural shelter belt had the same characteristics as the one in the field experiments. The numerical simulation however was not intended to reproduce R3 or any of the other experimental runs: to clarify the fate of particles, in lieu of the physical (line-) source a vertically extended (plane-) source was positioned upwind of the shelter belt at $X_S/W = -1.5$, and spanned the region $0 \leq z \leq 2H$ in the vertical. It released particles of diameter 33 μm ($w_g = 8.2$ cm) at a uniform rate along its vertical span ($2H$), i.e. uniform source distribution. The transmittance predicted by the model, $\kappa = 0.36$, was about five times larger than with the analytical approach ($\kappa = 0.07$). Taken at face value, this result is very surprising. One might have expected that the neglect of deposition by gravitational settling and of particle escape across the upper boundary (shown later in section 4.4.5), which would logically cause a reduced toll of deposition onto vegetation, would lead to an *over*estimation of the transmittance by the analytical theory. However in reality the mean velocity within the belt of corn varies along the path downwind, implying the strong possibility that the effective values taken for E_1, m might be inaccurate. Using the RANS-LS model we computed (still in the conditions described above)

$$\langle E_{\rm dv} \rangle = \frac{1}{N_{\rm p}} \sum \left[\frac{1}{t_2 - t_1} \int_{t_1}^{t_2} E_{\rm dv}\, dt \right] \tag{4.15}$$

$$\langle m \rangle = \frac{1}{W\, N_{\rm p}} \sum \int_{t_1}^{t_2} \sqrt{u^2 + v^2 + w^2}\, dt \tag{4.16}$$

where the brackets $\langle\ \rangle$ denote an ensemble average over the number of particles (N_p) which enter the hedge across its upwind face; t_1 and t_2 are the times when a particle enters and exits the shelterbelt; E_{dv} is the efficiency of deposition on a vegetation element, which accounts for both the impaction efficiency E_I (Eq. 4.4) and rebound (determined according to section 4.3.3). Eqs. 4.15-4.16 gave

$$\langle E_{dv} \rangle = 0.22 \tag{4.17}$$

$$\langle m \rangle = 0.63 \tag{4.18}$$

These values are drastically different from those predicted by the formulae of Raupach et al., i.e. $E_{dv} = E_I = 0.85$ and $m = 1.12$. The large overestimation of the deposition efficiency stems from the neglect of particle rebound, and presumably the assumption of a uniform and constant velocity across the shelterbelt shares some responsibility for the error. A meandering factor $\langle m \rangle$ smaller than unity may be surprising at first sight, for particles subject to turbulent fluctuations travel a longer (cumulative) path than they would along a straight line. However, as will be shown in next section (4.4.5), a significant portion of the particles traveling inside the shelterbelt exit through the top boundary or deposit onto vegetation or onto ground. As a result, they travel on average a distance shorter than the thickness W of the hedge.

But when we inserted these corrected (ie. model computed) values for E_I and m into the 'thin windbreak' theory, the resulting transmittance was $\kappa = 0.69$, about twice as large as the value ($\kappa = 0.36$) predicted by the numerical model. This merely highlights the ambiguity inherent in applying the thin windbreak theory to the present trials, because it is simply wrong to neglect the particle fluxes to ground and across the upper boundary of the

hedge. We stress that Raupach et al. never intended their theory to be used in the manner we have here applied it, and in this section our aim has merely been to emphasize the need for a more complex treatment of particle filtering by thick shelterbelts.

4.4.5 Particle dispersion patterns.

To understand the influence of a thick natural shelterbelt on particle dispersion, we need to look not only at processes within the hedge, but also in its vicinity. To this end Figure 4.13a shows a synthetic particle concentration field, as modelled by the LS model coupled with the RANS wind flow model in the conditions described in section 4.4.4. The grey shaded contours represent the concentration normalized by the source intensity, and the vectors show the mean velocity field. When looking at the concentration profile immediately downwind of the uniform source, the reader will notice that the concentration increases closer to ground, where the wind velocity decreases. In other words, particles tend to accumulate in low wind velocity regions. Marching downwind across the shelter belt a clear decrease in particle concentration is identifiable, due to particle deposition onto vegetation. However, the decrease is more marked in the upper part of the hedge. Figure 4.13b shows the vertical flux of particles (superposed on the mean wind field vector map) for the same conditions as in Figure 4.13a. The reader will notice the strong outflow of particles across the upper (horizontal) boundary of the thick hedge, seen by the grey shades representing a positive flux. This outflow depletes particles in the upper region of the hedge, thus explaining why concentration decreases faster than in the bottom region. Interesting features are identifiable downwind of the hedge too. The grey patch (positive flux) seen immediately downwind

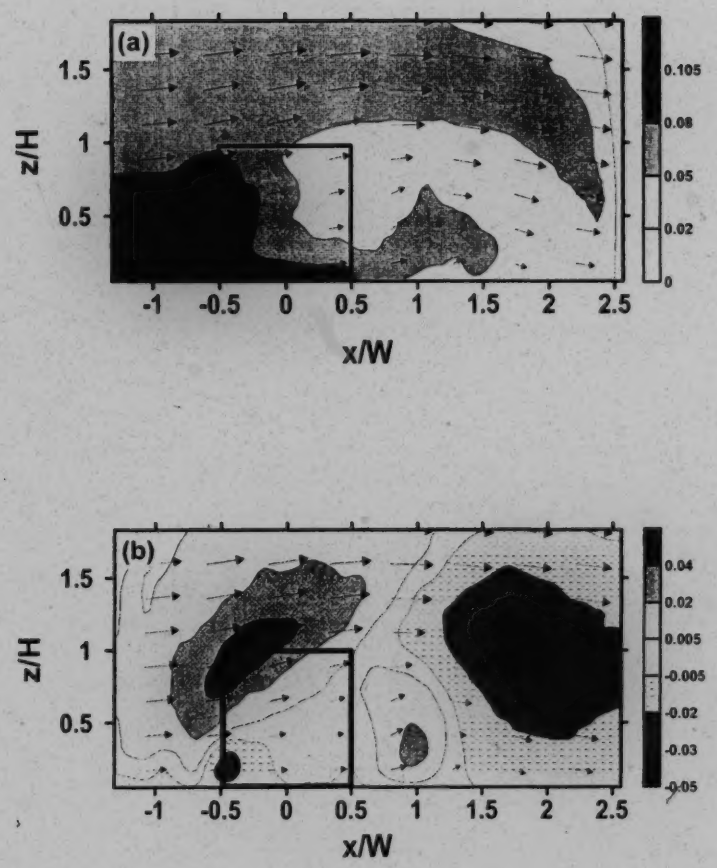

Figure 4.13: Fields of particle concentration (Panel a) and vertical fluxes (Panel b) about the corn belt (rectangle). Both concentration and fluxes are normalized by the source strength. The arrows show the mean wind vector field, computed for the conditions of run R3. The source is placed at $x/W = -1.5$ and releases 33 μm particles ($w_g = 8.2$ cm) uniformly along its vertical 2H span. Note that a positive flux points upwards.

of the shelter belt in Figure 4.13b shows an upwelling of particles, driven by a large positive vertical wind velocity. Further downwind, the mean vertical wind velocity becomes negative, causing particles to sink. The downwash flux is most pronounced at height $z/H \approx 1$, where concentration is highest (at this level downwind). Those characteristics of the particle vertical flux field translate into distortions of the particle plume downwind of the shelter belt as seen on the concentration map (Figure 4.13a).

The numerical simulations described above pertain to 33 μm particles, and it is worthwhile to investigate how particles of different sizes respond to the disturbance of a shelterbelt. Figure 4.14 shows the evolution of the proportion of particles of three different sizes (10 ± 1, 30 ± 1 and 50 ± 1 μm) along a horizontal transect crossing the shelterbelt. The results are obtained with numerical simulations identical to the ones described in the section 4.4.4, to the difference that the source released particles uniformly distributed in size in the range $9 - 51$ μm (as opposed to particles of diameter 33 μm).

The graph indicates that the size distribution drifts when marching downwind, with the 10 μm particles being increasingly represented to the detriment of the 50 μm particles. This trend starts immediately after particle release, and is due to faster gravitational settling of larger particles. The distribution drift accelerates sharply in the region of the shelterbelt ($-0.5 \leq x/W \leq 0.5$). As we mentioned in section 4.4.3, the efficiency of impaction of particles on vegetation is highly sensitive to particle size, with larger particles impacting more. As a consequence, smaller particles statistically deposit less onto vegetation. In other words, a shelterbelt filters preferentially large particles, which explains the drift of the size distribution towards small particles. This patterns is visible also on Figure 4.15. It shows the contour plot of the

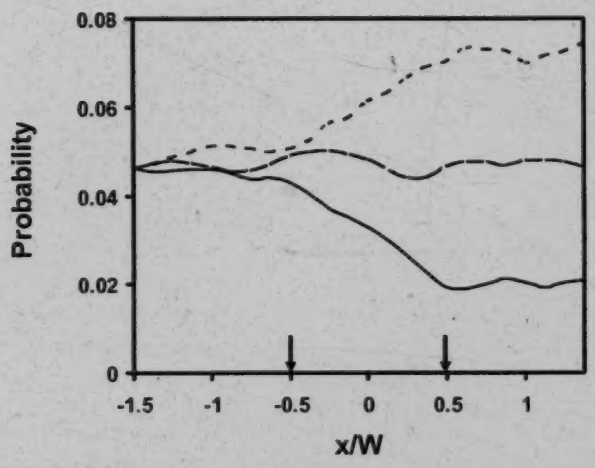

Figure 4.14: Probability of presence of particles with diameter 10 ± 1 μm (dotted curve), 30 ± 1 μm (dashed curve) and 50 ± 1 μm (solid curve) along a horizontal transect at $z/H = 0.6$ across the shelterbelt located at $-0.5 \leq x/W \leq 0.5$ (arrows indicate its limits). The source is placed at $x/W = -1.5$; it is spatially uniform in the vertical, and releases particles whose size distribution is uniform on the range $9 \leq d \leq 51$ μm. The meteorological conditions are those of run R3.

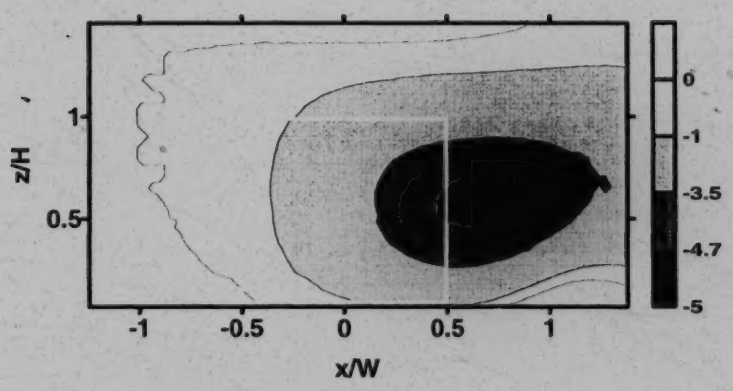

Figure 4.15: Deviation in the median particle size, in micrometers, calculated by numerical simulation. The source is spatially uniform along the vertical, and releases particles with diameters uniformly distributed in the range $9 - 51\mu$m, in a wind field consistent with meteorological conditions of run R3.

deviation of the median size of particles which have a uniform size distribution at source. The median size decreases as the plume crosses vegetation, due to preferential deposition of large particles. The deviation reaches a maximum (in absolute value) downwind from the windbreak around $x/W \sim 0.8$, where deposition onto vegetation does not occur anymore. The sharp depletion in large particles is due to the enhanced gravitational settling in this region where the wind reduction is strongest. Further downwind, the updraft partially annihilates this depletion.

The particle mass budget across the shelter belt becomes understandable in the light of the dispersion patterns described above. Figure 4.16 shows the 'fate' of 33 μm particles entering the shelter belt across its upwind (x_1) face[5]. More than a third of those particles deposit onto vegetation, and another third flow out across the top horizontal boundary ($z = H$). Only a small portion (less than 10%) deposit onto ground, and the remainder (about 25%) flow out across the downwind (x_2) face. With larger particles, the fraction depositing onto ground grows to the detriment of the outflux across the top boundary. However, the distribution of the particles remains overall qualitatively similar. As a consequence, the fluxes across the horizontal faces of the thick hedge (i.e. deposition flux on ground and vertical flux across the top boundary) cannot be neglected, as they amount to more than 40% of the particle flux entering the shelter belt. These findings confirm that the theory of Raupach et al. (2001), applicable in principle only to thin windbreaks, indeed (and unsurprisingly) does not provide a good approximation of the rate of particle entrapment by

[5]The terms of the mass budget do not add precisely to 100% (Figure 4.16) because particles may enter the shelterbelt volume across the top face, without traversing the upwind side, and thereby contribute to the mass budget; but the normalizing flux is that entering across the upwind face.

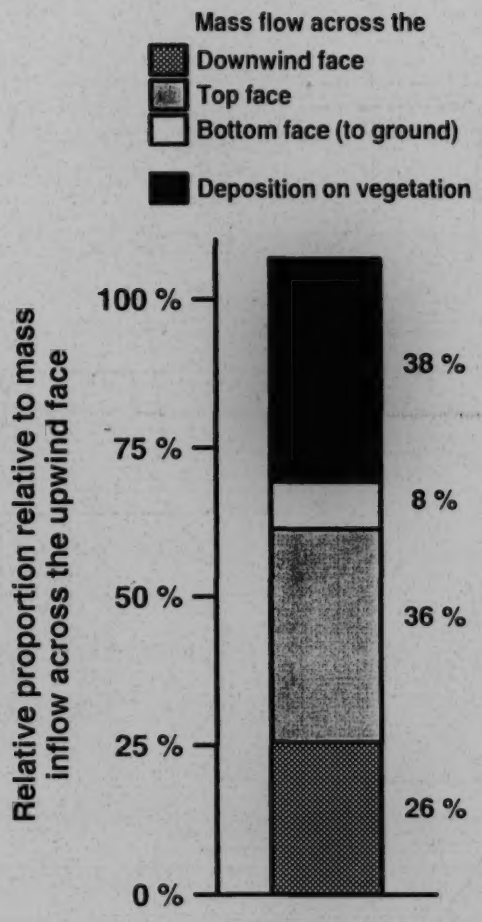

Figure 4.16: Particle mass budget in the shelterbelt (numerical simulation). The source is placed at $x/W = -1.5$ and releases 33 μm particles ($w_g = 8.2$ cm) uniformly along its vertical 2H span. The particles are carried in a wind flow computed for the conditions of run R3.

thick windbreaks.

We close this section by noting that the simulations indicate a rather minor role of velocity fluctuations in particle transport about the windbreak, a factor which, if generally valid, may permit helpful simplification in any future effort to construct a simpler entrapment theory than the type of detailed numerical simulation we have employed in this paper. Figure 4.17 indicates the horizontal fluxes of particles across the hedge's inflow (x_1, Panel a) and outflow (x_2, Panel b) faces are carried essentially by the mean (horizontal) wind: in the conditions run R3, at most about 15% of the particles are carried by the turbulent wind field. In other words the flux of particles transported by the mean wind, which can be easily measured experimentally (with wind cups and particle trapping instruments for example), approximates the total flux rather well.

It is interesting to notice that the turbulent flux across the downwind face remains essentially zero along the vertical. This is consistent with the concentration field (Figure 4.13a). Indeed, concentration increases both to windward and to leeward from the hedge's downwind side; in turn the horizontal gradient of concentration is likely to be close to zero across this downwind face, causing the turbulent flux to vanish (if one may hazard to invoke the gradient-diffusion paradigm). Only near ground does the turbulent flux become significant, where the concentration gradient and turbulent intensity are high. Figure 4.18 presents the vertical flux across the top (horizontal) face of the hedge. Clearly, both the turbulent flux and the flux driven by the gravitational settling velocity remain minor relative to the flux carried by the mean wind.

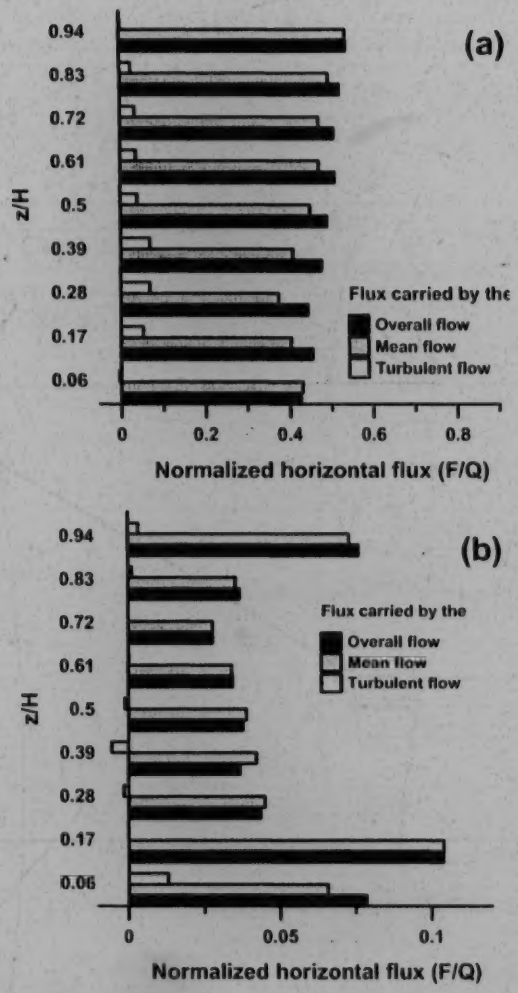

Figure 4.17: Computed horizontal fluxes of particles carried by the mean velocity field (in grey shade), the turbulent velocity field (in white) or by the overall wind field (in black), across the upwind face of the shelterbelt (Panel a) or the downwind face (Panel b). The source is placed at $x/W = -1.5$ and releases 33 μm particles ($w_g = 8.2$ cm) uniformly along its vertical 2H span. The particles are carried in a wind flow computed for the conditions of run R3.

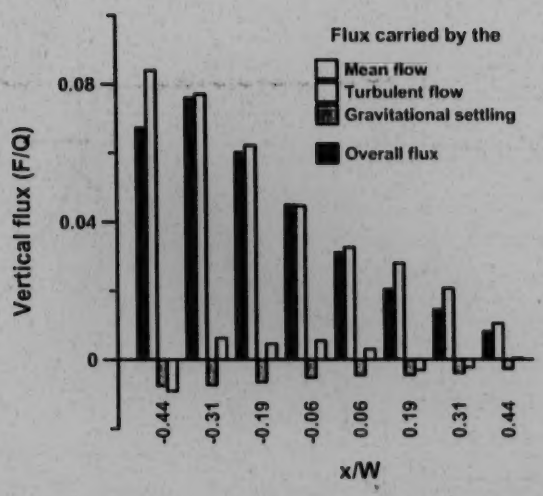

Figure 4.18: Computed vertical flux across the top boundary of the shelterbelt, carried by the mean flow (in light grey), the turbulent flow (in white) or the gravitational settling (in dark grey). The overall flux (in black) is the sum of all the others. Note that a positive flux points upwards.

4.5 Conclusions

This paper has focused on the role of a shelter belt as a particle filter, and therefore on trajectories *within* the vegetation, taking a few specific cases of the meteorological conditions and a single example of the windbreak dimension, vegetation density, leaf orientation and size. What has been proven is that entrapment may be described reasonably well by RANS-LS modelling, with errors in the concentration jump across the hedge no larger than 25%. However that computational approach is burdensome and inconvenient, accessible only to specialized individuals or teams. The simple analytical approach of Raupach et al. (2001) is not appropriate to capture particle filtering by a thick natural shelterbelt. For rapid practical calculations, a generalized analytical description is needed. Although we offer no progress in that regard, the present data highlight the want of (and hopefully will serve to test) a simplified theory.

As well as filtering the airstream through it, obviously a windbreak perturbs the paths of particles in its general vicinity. It would be interesting to investigate the overall impact of a shelter belt - acting as both a filter and as a windbreak - on the aerial transportation and deposition of particles, at a scale of tens to hundreds and even thousands of meters. Studying the sensitivity of the dispersion patterns to the meteorological conditions (friction velocity, thermal stability, wind obliquity) and to the specifics of the vegetation might allow us to determine in what conditions particles are most vulnerable to long distance drift, and to suggest an optimal design in terms of geometry, vegetation density and leaf size. Those issues will be addressed in future work.

4.6 References

Aylor, D. E., 1982: Modeling spore dispersal in a barley crop. *Agric. Meteorol.*, **26** (3), 215-219.

Aylor, D. E., 1990: The role of intermittent wind in the dispesal of fungal pathogens. *Annu. Rev. Phytopathol.*, **28**, 73-92.

Aylor, D. E. and T. K. Flesch, 2001: Estimating spore release rates using a lagrangian stochastic simulation model. *J. Appl. Meteorol.*, **40**, 1196-1208.

Bouvet, T., J. D. Wilson, A. Tuzet, 2006: Observation and modelling of heavy particle dispersion in a windbreak flow. *Journal of Applied Meteorol., in press.*

Csanady, G. T., 1963: Turbulent diffusion of heavy particles in the atmosphere. *J. Atmos. Sci.*, **20**, 201- 208.

Dahneke, B. J., 1971: Capture of aerosol particles by surfaces. *J. Colloid. Interface Sci.*, **37**, 342.

Dahneke, B. J., 1975: Kinetic-theory of escape of particles from surfaces. *J. Colloid. Interface Sci.*, **50**, 89-107.

Dong, Z., X. Wang and L. Liu, 2000: Wind erosion in arid and semi-arid China: an overview. *J. Soil and Water Conserv.*, **55.4**, 439-444.

Jarosz, N., B. Loubet, B. Durand, A. McCartney, X. Foueillassar, L. Huber, 2003: Field measurements of airborne concentration and deposition rate of maize pollen. *Agric. For. Meteorol.*, **119** (1-2), 37-51.

Maber, J., 1998: Spray drift and shelter. A brief summary of the effects of shelter on spray drift, Lincoln technology, Hamilton, New Zealand, 5 pp.

May, K. R., R. Clifford, 1967: The impaction of aerosol particles on cylinders, spheres, ribbons and discs. *Ann. Occup. Hyg.*, **10**, 83-95.

Oldeman L. R., R. T. A. Hakkeling, and W. G. Sombroek, 1991: World Map of the Status of Human-Induced Soil Degradation. An Explanatory Note, revised version. *United Nations Environment Program (UNEP) and International Soil Research Information Cente (ISRIC)*, Wageningen, Netherlands, 35 pp.

Paw U, K. T, 1983: The rebound of particles from natural surfaces. *J. Colloid. Interface Sci.*, **93**, 442-452

Rao, K.S., J. C. Wyngaard, O. R. Cote, 1974: Local Advection of Momentum, Heat, and Moisture in Micrometeorology. *Boundary-Layer Meteorology*, **7**,331-348.

Raupach, M. R., N. Woods, G. Dorr, J.F. Leys, H.A. Cleugh, 2001: The entrapment of particles by windbreaks. *Atmos. Environ.*, **35**, 3373-3383.

Shaw, D. L., 1988: The design and use of living snow fences in North America.

Agric. Ecosystems Environ., **22/23**, 351-362.

Shaw, D. T., 1978: Fundamentals of aerosol science. Wiley, New York, 372pp.

Thomson, D. J., 1987: Criteria for the selection of stochastic models of particle trajectories in turbulent flows. *J. Fluid Mech.*, **180** , 529-556.

Ucar, T., F. R. Hall, 2001: Windbreaks as a pesticide drift mitigation strategy: a review. *Pest Manag. Sci.*, **57**, 663-675.

Waggoner, P. E., G. S. Taylor, 1958: Dissemination by atmospheric turbulence: Spores of Peronospora tabacina. *Phytopathology*, **48**, 46-51

Wilson, J. D., 2000: Trajectory Models for Heavy Particles in Atmospheric Turbulence: Comparison with Observations. *J. Applied Meteorol.*, **39**, 1894-1912.

Wilson, J. D., 2004: Oblique, Stratified Winds about a Shelter Fence. Part II: Comparison of Measurements with Numerical Models. *J. Applied Meteorol.*, **43**, 1392-1409.

Wilson, J. D., T. K. Flesch, L. A. Harper, 2001: Micro-meteorological Methods for Estimating Surface Exchange with a Disturbed Windflow, *Agric. For. Meteorol.*, **107**, 207-225.

Woods, N., I. P. Craig, G. Dorr, B. Young, 2001: Spray drift of pesticides arising from aerial application in cotton. *J. environ. qual.*, **30**, 697 - 701.

Xu, M., K. Willeke, 1993: Impaction and rebound of particles at acute incident angles. *Aerosol sci. tech.*, **18**, 143-155.

Chapter 5

Conclusions

Contents

5.1 Summary of findings 180

5.1.1 Provision of an approximate solution for the deposition of heavy particles on uniform terrain 180

5.1.2 Provision of new experimental data. 181

5.1.3 Diagnosis of the capabilities of a coupled RANS-LS model. 181

5.1.4 Insight into the patterns of dispersion in a windbreak flow. 183

5.2 Recommendations for future research. 184

5.2.1 Provision of recommendations for windbreak design . 184

5.2.2 An analytical treatment of particle filtering. 185

5.3 Long distance particle transport and landscape structure: a broader perspective. 185

5.4 References 188

5.1 Summary of findings

This thesis revolves around providing tools to quantify and investigate the dispersion patterns of heavy particles, either over level terrain or in a windbreak-disturbed flow.

5.1.1 Provision of an approximate solution for the deposition of heavy particles on uniform terrain

The first of my main contributions gives a two-dimensional approximate analytical solution for the deposition of heavy particles released from an elevated source over uniform terrain. The solution is tested against both experimental and numerical results, and its domain of applicability is discussed. From the complete analytical solution are derived simple relationships between statistics characterizing the deposition swath and the variable $\overline{u}(H_s)/w_g$, valid in the domain $\overline{u}(H_s)/w_g < 7$ (where $\overline{u}(H_s$ is the mean horizontal velocity at source height, and w_g is the gravitational settling velocity of the dispersing particles). Because the variable $\overline{u}(H_s)/w_g$ is easily accessible, those relationships are readily exploitable. They are of practical interest for pollution risk management purposes. They allow for instance to estimate (i) the extent of the ground contamination downwind of a pollution source; (ii) the location on the ground where pollution reaches a peak; (iii) the intensity of this peak deposition, to be compared with acceptable levels of pollution. The analytical solution is also an ideal tool to test the sensitivity of the deposition patterns to the various parameters coming into play, thus gaining insight on the driving factors which control dispersion. In particular, it could be exploited to investigate the impact of the micro-meteorological conditions (i.e. wind intensity, thermal stratification, expressed in terms of friction velocity, roughness

length, and Monin-Obukhov length) on the deposition patterns, in relation to the source height and the particles' settling velocities.

5.1.2 Provision of new experimental data.

The second and third of my contributions address dispersion of a heavy particle plume passing by a windbreak. Whereas an analytical description is achievable in the relatively simple case of dispersion over uniform terrain, other tools become necessary to investigate dispersion in more complex flows, viz. field observations and numerical modelling. Because experiments are time consuming, and because their implementation demands extensive instrumentation facilities and technical support, observations pertaining to heavy particle dispersion are very scarce. Hage (1961) and Walker (1965) measured the deposition of heavy particles released from an elevated source, over level undisturbed terrain. Caput et al. (1973) measured deposition rate and aerial concentration of particles released into a windbreak flow; but the particles utilized were aerosols of a diameter smaller than a few micrometers, which behaved therefore virtually like passive tracers. In turn the available data are very limited, and in any case not relevant to the present study. In this context, the provision here of new experimental observations is very valuable and constitutes a major contribution of this work.

5.1.3 Diagnosis of the capabilities of a coupled RANS-LS model.

The new observations are used to test the capabilities of a coupled RANS-LS (wind/trajectory) model to capture the essentials of heavy particle dispersion in a windbreak flow. As is the norm in micrometeorology, discrepancies be-

tween the numerical results and experimental data exist, and these can be ascribed to some or all of the following factors: inaccuracy of the observations, inadequate skill of the RANS model to reproduce properly the statistics of the wind flow, and/or inadequacy of the LS simulations. Experimental errors are believed not to have contributed significantly to the mismatch with numerical results, for quality tests on the experimental procedures proved them to be satisfactory in most cases, and where otherwise measures were taken to minimize impact of errors on the results presented. The wind flow simulations on the other hand seem likely to have contributed significantly to the observed discrepancies. In effect, Wilson (2004) showed that velocity variances (in particular) are poorly reproduced by the RANS model, and that the sheltering effect in oblique flows is underestimated. Finally the LS model is bound to contribute a share of the error, for any model is in essence a simplified description of natural phenomena. In any case, the discrepancies reported remain relatively small, and all numerical results proved satisfactory in qualitative terms. Indeed the model reproduces fairly well the overall shape and extent of deposition swaths downwind of a fence, and their peaks are well located. Because the wind flow produced by the RANS model proved to be flawed in some respects, I believe that it is responsible for most of the error. In turn the performance of the LS model is quite satisfactory. A few years ago, Leuzzi and Monti (1998) showed that the dispersion patterns of tracer particles flowing around a building were adequately captured by Thompson's (1987) LS model. This present study provides additional evidence that the generalized Langevin equation (as formulated by Thompson), skillfully handles situations of strong inhomogeneity of the flow in all dimensions. Wilson (2000) showed that the adjustments to accommodate the dispersive peculiarities of heavy particles were

useful in a situation of aerial transport over level terrain. This work confirms Wilson's finding, and extends its relevance to highly heterogeneous wind flows.

To simulate particle dispersion inside a corn shelterbelt, a module for particle entrapment on vegetation impediments was added to the RANS-LS model. The rate of filtration across the thick hedge compared satisfactorily with observations, as the jump in magnitude of concentration across the width of the belt was well captured. Although relatively small, discrepancies however existed. The impaction efficiency on leaves being very variable in the range of values (for the velocity of the host flow, leaf dimension, and particle inertia) applicable to the experimental conditions, the model as a whole was very sensitive to errors in the input parameters. Considering together that (i) the module for particle entrapment is unforgiving of input errors; (ii) the wind flow provided by the RANS model is imprecise; (iii) the discrepancy with observation is relatively small, it is concluded that filtration is well captured in the modelling. Thus I suggest this work has presented and tested a numerical model capable of reproducing satisfactorily heavy particle dispersion in a windbreak flow, accounting for both the disturbance in the wind flow and the entrapment of particles on vegetation.

5.1.4 Insight into the patterns of dispersion in a windbreak flow.

Finally, this study discusses the impact of a windbreak on the dispersion patterns, both inside and about it. In particular it shows that whereas the intensity of the deposition peak is reduced in the presence of a barrier, the location

of the cone of the swath is only modestly altered. This latter trait results from the conflicting effects of the disturbances in the horizontal and the vertical mean flow fields. Overall the impact of a windbreak on the deposition peak seems therefore beneficial (at least when particles are regarded as pollutants). However, the presence of a fence causes a small fraction of the particles to drift further away then they otherwise would have. In other words, setting up a windbreak is a relevant strategy as far as it is desired to reduce the deposition rate (which could be regarded as pollution intensity) below a critical level. If on the other hand confinement of a polluting plume is desired, a windbreak is not an appropriate mitigator. The present work also provides insight regarding the patterns of dispersion *inside* a thick (3.2 m wide) corn shelterbelt (as opposed to '*about* a fence' as previously discussed). It is found that if a large portion of particles entering the hedge effectively remains entrapped on vegetation, a similar portion of them escapes through the top boundary, carried essentially by the mean flow.

5.2 Recommendations for future research.

5.2.1 Provision of recommendations for windbreak design

While the impact of a windbreak (whether it be thin and artificial or thick and natural) is broached in this study, the numerical tools presented could be further exploited to investigate in greater detail the dispersion patterns and their controlling factors. A natural follow-up on this work would be to investigate the combined effects of windflow disturbance and particle entrapment on particle dispersion for a variety of source spatial distributions commonly

encountered. Analyzing the sensitivity of the dispersive patterns to meteorological conditions (i.e. obliquity of incidence of the approaching flow, thermal stratification, roughness of the terrain, turbulence intensity) would allow to point up the critical features of the host flow. Subsequently the conditions in which a windbreak is most or least efficient could be identified. The numerical model would also be a useful tool to investigate the influence of the windbreak structure (density, heterogeneity, and shape of impactors) and geometry (height, width, shape). Such a study could lead to recommendations for windbreak design in relation to meteorological conditions, in particular in those where particle drift becomes an issue.

5.2.2 An analytical treatment of particle filtering.

Because numerical modelling is accessible to only a few privileged scholars or to organizations with sufficient resources (even though I acknowledge its tremendous usefulness), analytical descriptions remain incomparably more valuable for practical applications which require rapid calculations. For the specific issue of particle filtration by a natural shelterbelt I believe that, guided by the insight provided by the numerical model, the simple analytical approach of Raupach et al. (2001) can be refined and generalized to account for particle rebound and leakage through the horizontal boundaries of a barrier.

5.3 Long distance particle transport and landscape structure: a broader perspective.

The study of particle dispersion about windbreaks should be seen in the broader perspective of landscape fragmentation and long-distance transport. Although small scale (of the order of 100 m or less) topographical features of

the landscape, such as windbreaks, have only minor impact on the wind patterns in the convective boundary layer (Avissar and Schmidt, 1998; Gopalakrishnan et al., 2000), they may be responsible for the onset of long distance transport (over thousands of kilometers) of heavy particles such as spores, pollens or pathogens (Campbell et al., 1999; Brown and Hovmoller, 2002). In effect, because heavy particles settle to ground under gravity, they can only lift-off and catch strong wind flows higher up when launched by sufficiently strong updrafts (Burrows, 1986). Intuition suggests that while even on flat, undisturbed terrain strong updrafts can and do occur near ground (e.g. associated with dust devil), heterogeneities in the landscape such as barriers that distort the mean flow and create turbulence must trigger supplementary and (probably) more frequent and stronger events. Whereas large scale air circulation does not 'feel' small boundary structures, Roy and Avissar (2000) explain that land surface heterogeneities of larger scale (2-20 Km) significantly impact the flow patterns in the convective boundary layer (CBL), and in turn affect atmospheric transport processes. Whether those heterogeneities consist in changing topography or changing surface type, they result in differential heating of the air layer above ground. Horizontal pressure gradients are thus created; they drive air from cooler to warmer regions and as a result well organized and preferentially-located "roll" circulations form, with a characteristic size similar to the length scale of the heterogeneity which triggered them. When landscape heterogeneities are longer than 5-10 km, random turbulent eddies (resulting from thermals, with a horizontal extent of 2-3 km) appear and coexist with the rolls. Gopalakrishna and Avissar (2000), investigating the dispersion of tracer passive particles with a coupled LES-LS model, show that the flow patterns previously described deeply affect transport processes.

Indeed when particles are released over uniform terrain they tend to migrate to the middle of the CBL (carried by updrafts if released near ground, or by downdrafts when released high in the CBL). If the terrain is heterogeneous, the rolls reduce vertical mixing and in turn particles released at surface do not lift off, but rather they concentrate near ground. They note however that the effect is weaker when the heat flux is high, for the strong thermal updrafts break the horizontal rolls. Presumably, the effect weakens also when the length scale of the landscape heterogeneities increases, for the horizontal pressure gradients drop accordingly.

To sum up, if windbreaks markedly alter the transport of heavy particles at a local scale, they can also favour the onset of long distance transport. This illustrates how man can influence regional or even continental scale dispersion by local modification of the surface structure. Fragmentation of the land space at a larger scale, of the order of kilometers, also strongly affects transport processes. As a result land-use planning should be considered when addressing long distance aerial transportation and mitigation of pollution events.

5.4 References

Avissar, R., T. Schmidt, 1998: An evaluation of the scale at which ground-surface heat flux patchiness affects the convective boundary layer using large-eddy simulations. *J. Atmos. Sci.*, **55**, 2666-2689.

Brown, J. K. M. and M. S. Hovmoller, 2002: Aerial dispersal of pathogens on the global and continental scales and its impact on plant disease. *Science*, **297**, 537-541.

Burrows, F. M., 1986: The aerial motion of seeds, fruits, spores and pollen. *Seed dispersal* (ed. by D. R. Murray, Academic Press, Sydney), pp1-47.

Campbell, I. D., K. McDonald, M. D. Flanningan and J. Kringayark, 1999: Long-distance transport of pollen into the Arctic. *Nature*, **399**, 29-30.

Caput, C., Y. Belot, G. Guyot, C. Samie and B. Seguin, 1973: Transport of diffusing material over a thin wind-break. *Atmos. Environ.*, **7**, 75-86.

Gopalakrishnan, S. G. and R. Avissar, 2000: An LES study of the impacts of land surface heterogeneity on dispersion in the convective boundary layer. *J. Atmos. Sci.*, **57**, 352-371.

Gopalakrishnan, S. G., S. B. Roy and R. Avissar, 2000: An evaluation of the scale at which topographical features affect the convective boundary layer using large-eddy simulations. *J. Atmos. Sci.*, **57**, 334-351.

Hage, K. D.: 1961, On the dispersion of large particles from a 15-m source in the atmosphere, *J. Meteorol.* **18**, 534-539.

Leuzzi, G., P. Monti, 1998: Particle trajectory simulation of dispersion around a building. *Atmos. Environ.*, **32**, 203-214.

Roy, S. B. and R. Avissar, 2000: Scales of response of the convective boundary layer to land-surface heterogeneity. *Geophys. Res. Lett.* **27**, 533-536.

Walker, E. R.: 1965, A particulate diffusion experiment, *J. Appl. Meteorol.* **4**, 614-621.

Wilson, J. D., 2000: Trajectory models for heavy particles in atmospheric turbulence: comparison with observations, *J. Appl. Meteorol.* **39**, 1894-1912.

Wilson, J. D., 2004: Oblique, stratified winds about a shelter fence. Part II: Comparison of measurements with numerical models. *J. Appl. Meteorol.*, **43**, 1392-1409.

Appendices

Contents

A-1 Finite-difference solutions of the advection-diffusion equation. 192

A-2 The Lagrangian Stochastic (LS) model. 194

A-3 Steadiness of the passive point source in runs P . 195

A-4 Lateral homogeneity of the line source (runs L) . 197

A-5 Possible disturbance of deposition collector walls on particle deposition 199

A-6 Automated particle count 201

A-7 Code sources 203

A-1 Finite-difference solutions of the advection-diffusion equation.

To test the consequence of neglecting turbulent deposition, we solved the advection-diffusion equation numerically with the contribution of turbulent deposition retained, using a regular, high-resolution mesh ($\triangle x = \triangle z = 0.01\, H_s$) covering a computational domain sufficiently long ($100\, H_s$) to encompass most of the deposition swath and sufficiently high ($50\ H_s$) to ensure that the particle plume did not reach the top of the domain. An upwind difference was used for $\partial c/\partial x$, and a central difference was used for the vertical derivative (we followed the general approach of Patankar, 1980).

The source was placed at the entry boundary (index $i = 0$) of the computational domain, where we prescribed a condition consistent with a line source, viz:

$$\frac{c(0,j)}{Q} = \frac{1}{\triangle z\, \overline{u}(j)}\, \delta_{j,j_H} \qquad \text{(A-1)}$$

where j indexes gridpoint positions on the height axis and j_H identifies the index coinciding most closely with source height. At the top of the domain

$$\frac{c}{Q}(i, j_{max}) = 0 \qquad \text{(A-2)}$$

No boundary condition was needed at the downwind ($i = i_{max}$) boundary, for due to the absence of diffusion on the x-axis this is a 'one-way' coordinate (Patankar, 1980). Parameterizations for $\overline{u}(j)$ and $K(j)$ were identical to the ones used in the analytical treatment, i.e. Eqs. 2.5-2.6, with ξ as in Eq. 2.25. The numerical scheme was implicit on the z-axis, and the solution was obtained without iteration, simply by marching downwind on the x-axis away from the known inflow profile. When applied to the dispersion of passive tracer, this

scheme essentially reproduces the observations of Project Prairie Grass (Barad, 1958).

A-2 The Lagrangian Stochastic (LS) model.

To test the skills of the analytical solution, we performed simulations of particle dispersion using a 1^{st} order Lagrangian Stochastic (LS) model. Such a model computes an ensemble of independent particle trajectories emanating from the source, by generating for each particle a time series of velocity and integrating it with respect to time. A statistically meaningful, smooth deposition swath is then inferred from a large ensemble of particle paths.

We used the LS model described by Wilson (2000) under the label 'Inertial Particle (IP) Model' (section 2b of his paper). This model relies on two coupled equations: a Langevin equation gives the velocity of the 'driving fluid' that surrounds a heavy particle, and that velocity is imposed in the equation of motion for the particle's acceleration. The Langevin equation is adapted to surface-layer flow statistics and the Lagrangian time scale is corrected for the crossing trajectory effect following Sawford and Guest (1991); see appendices (A,B) of Wilson (2000) for details. In order to best correspond with the analytical treatment being tested, the LS model was 2-dimensional, and particles were always released at the same elevated location H_s. The boundary condition on ground was also consistent across the two treatments, the ground being supposed to be a perfectly absorptive surface. Thus in the LS model a particle trajectory was terminated as soon as it reached the roughness height z_0, which means that the phenomenon of re-suspension was excluded.

A-3 Steadiness of the passive point source in runs P

Whereas, upon testing, we found no noticeable correlation between the particle release rate and the wind speed, the vibration frequency (or equivalently the rotation speed of the motor) emerged as the factor controlling the release rate, and so we ensured that it be steady and equal over all runs. In humid conditions, particles agglomerated and blocked the source. All the experiments presented in this study were run in dry conditions, when the source did not clog. Figure A-1 presents the evolution of the source intensity with time over a run, showing a fairly steady rate of release. The smooth functioning of the source gives evidence that glass beads did not agglomerate and therefore did not disperse in clusters.

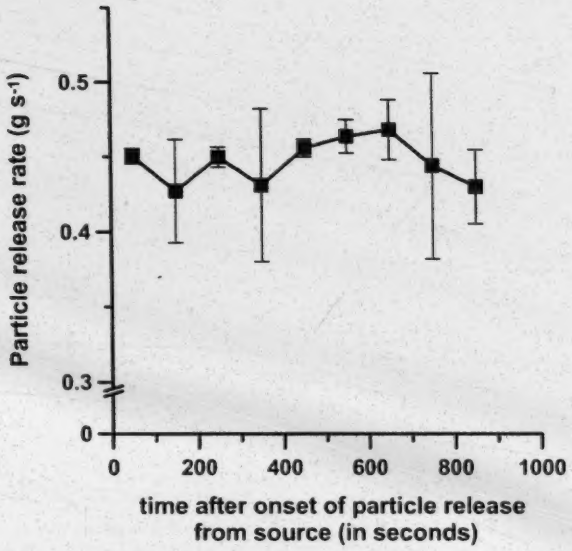

Figure A-1: Evolution of the particle source release rate over the duration of an experimental run. The error bars show the standard deviation of the release rate over five repetitions of the test.

A-4 Lateral homogeneity of the line source (runs L)

In order to test the lateral homogeneity of the plume, we sampled the deposition rate of particles onto the ground at intervals of one meter along a 20 m transect that ran parallel to the source, at a range of $x = 10H_s$ (a range that LS simulations -not shown- suggested to be sufficient for individual plumes to merge). This test was run over a 60 minute period, so as to smooth out the irregularity in the lateral distribution of the plume due to the fluctuating wind direction. Figure A-2 presents the results of this test and shows a significant (unwanted) heterogeneity in the deposition along this lateral transect. Measurements of the quantity of particles released revealed differences up to 30% from one individual point source to another. This probably explains the heterogeneity observed further downwind. Therefore, we measured in each run and for each point source the quantity of particles released so as to know the source intensity distribution $Q(y_i) = Q_0 f(y_i)$, where $Q(y_i)$ is the release rate at the (discrete) location of the source y_i, Q_0 is the overall magnitude of the release rate, and $f(y_i)$ is the profile factor. We reproduced this measured profile factor in the numerical simulations. Evolution of the particle source release rate over the duration of an experimental run. The error bars show the standard deviation of the release rate over five repetitions of the test.

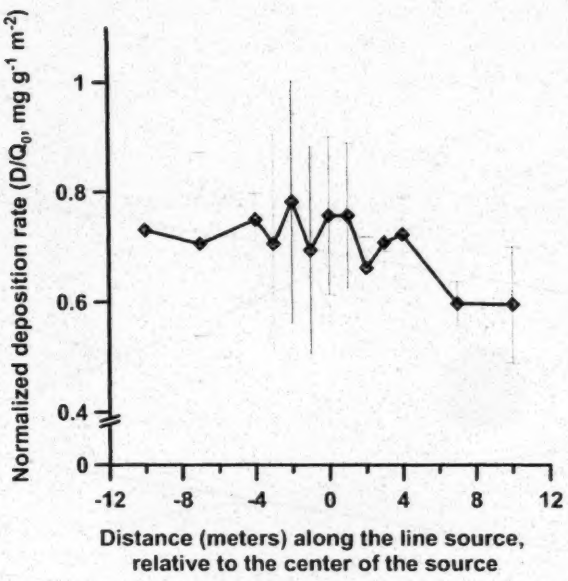

Figure A-2: Normalized deposition rate along the windbreak, at a distance x/H=10 from the source. The positions of the x-axis correspond to the distance form the source plume centerline. Those experimental data were retrieved from a single 60 min run. The error bars show the standard deviation derived from the three automated counts.

A-5 Possible disturbance of deposition collector walls on particle deposition

Ideally, the deposition collectors are flat surfaces lying on ground. In practice we used Petri dishes, the wall of which may have interfered with particle deposition in two ways. First, the walls locally disturbed the flow. Secondly, as the walls rise above the deposition surface, they blocked beads whose velocity had a non-zero horizontal component. In order to obtain further insight into the significance of the wall disturbance, we compared the deposition rate in two types of collectors differing only by the height of their walls: the Petri dishes (18 mm high walls) versus cylinders with higher walls (80 mm). These were placed side by side, 20 cm apart to avoid interference, along a deposition transect. Figure A-3 presents the ratio of deposition into high wall collectors to deposition into low wall collectors (Petri dishes), as a function of the bead diameter. The graph shows that for beads larger than 29 microns, the average ratio is 1 ± 0.04, therefore extremely close to unity. In this study, we have analyzed the dispersion specifically of 34 ± 2 μm particles, which are therefore not affected by the 'wall disturbance'.

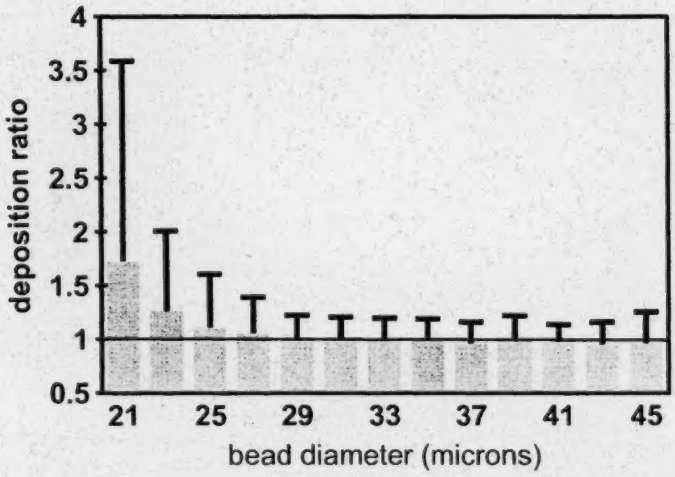

Figure A-3: Ratio of particle deposition into high wall collectors (80 mm high) to deposition into low wall collectors (18 mm high). For each diameter, the values for the mean and the standard deviation (shown in the error bars) are derived from 31 values.

A-6 Automated particle count

Deposition samples were counted in liquid phase by an automated counter (Beckman Coulter Multisizer®). In order to test the accuracy of the particle count by this automated procedure, we compared it to an optical count, which was taken as 'truth'. At various positions along the deposition transect seen on Figure 3.1, particles were trapped both in a Petri dish (for the automated count) and on a sticky glass strip that could be directly analyzed under a microscope, for optical count. The two collectors were again placed side by side again, 20 cm apart to prevent interference. Figure A-4 presents comparatively the results. The automated count systematically overestimated the optical count, by 34% on average. The sampling procedure of the automatic counter was probably responsible for the bias. In effect, particles had a density 2.5 higher than the solution they were imbedded in. In turn, as the solution was stirred vigorously, the centrifugal force pushing the particles outwards may well have lead to a preferential concentration in particle by the walls, where particles were sampled. The systematic bias observed affects the magnitude of the deposition rates measured experimentally. However, we present data of deposition normalized by the source strength Q_0, which is tuned for an optimal match with LS simulations. The magnitude of the deposition swath is therefore re-scaled, and the bias we observed in the counting has no impact on the experimental results presented.

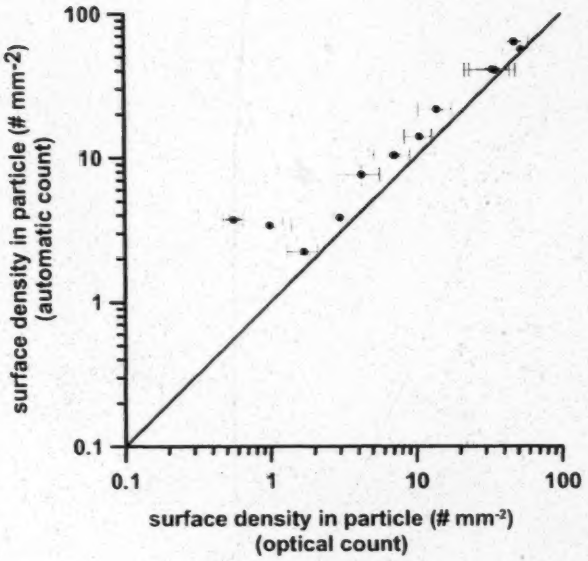

Figure A-4: Comparison of counting procedure, automated count versus optical count. The solid line represents the perfect match (i.e. y=x), and is displayed as a reference. The vertical error bars show the standard deviation in the automated count of three samplings for each measurement. The horizontal error bars show the standard deviation of five samplings for each measurement.

A-7 Code sources

The code sources are stored in the attached CD.